Southampton

University of Southampton Research Repository

Copyright © and Moral Rights for this thesis and, where applicable, any accompanying data are

retained by the author and/or other copyright owners. A copy can be downloaded for personal non-

commercial research or study, without prior permission or charge. This thesis and the accompanying

data cannot be reproduced or quoted extensively from without first obtaining permission in writing

from the copyright holder/s. The content of the thesis and accompanying research data (where appli-

cable) must not be changed in any way or sold commercially in any format or medium without the

formal permission of the copyright holder/s.

When referring to this thesis and any accompanying data, full bibliographic details must be given, e.g.

Thesis: Author (Year of Submission) "Full thesis title", University of Southampton, name of the

University Faculty or School or Department, PhD Thesis, pagination.

Data: Author (Year) Title. URI [dataset]

University of Southampton

Faculty of Social Sciences
School of Mathematics

Strangeness and anisotropic phases in dense nuclear matter in the chiral transition region

by

Savvas Pitsinigkos

MASt

ORCiD: 0000-0001-8674-4876

A thesis for the degree of Doctor of Philosophy

April 2025

University of Southampton

Abstract

Faculty of Social Sciences School of Mathematics

Doctor of Philosophy

Strangeness and anisotropic phases in dense nuclear matter in the chiral transition region

by Savvas Pitsinigkos

The theory of Quantum Chromodynamics presents a rich phase structure. However, while the low temperature and intermediate density region is a key piece in understanding the physics of neutron stars, it is also elusive from ab-initio methods and experiments. In this thesis we discuss two different models that explore the phase diagram of Quantum Chromodynamics.

In the first part we construct a model for dense matter based on low-density nuclear matter properties that exhibits a chiral phase transition and includes strangeness through hyperonic degrees of freedom. Along with empirical constraints from nuclear matter we require that at asymptotically large densities the chirally restored phase contains strangeness and the speed of sound approaches the conformal limit, resulting in a high-density phase that resembles deconfined quark matter. Additionally, the model is required to reproduce sufficiently massive compact stars. We also find that for the allowed parameter range strangeness does not appear in the chirally broken phase and that the chiral transition is of first order.

In the second part we employ a simpler version of this model to discuss the competition between isotropic and anisotropic phases. Assuming isotropy, the model exhibits a chiral phase transition which is a crossover. This observation crucially depends on the presence of the nucleonic vacuum contribution, an important addition to this model. Allowing for an anisotropic phase in the form of a chiral density wave can disrupt the smooth crossover. We identify the regions in the parameter space of the model where a chiral density wave is energetically preferred. A high-density re-appearance of the chiral density wave demonstrating unphysical behavior, is avoided by a suitable renormalization scheme. We find that, within our model, the chiral density wave is only realized for baryon densities of at least about 6 times nuclear saturation density.

As an introduction, the necessary tools and concepts are presented. In the end, possible extensions of this work are discussed.

Contents

D	eclara	tion of	Authorship	vii
A	cknov	vledger	nents	ix
1	Intr	oductio	n	1
	1.1	Quant	um Chromodynamics	2
		1.1.1	Symmetries of QCD	4
		1.1.2	Chiral effective field theory	9
		1.1.3	A phase diagram for Quantum Chromodynamics	11
	1.2	Pheno	menology	15
		1.2.1	The Walecka model	16
		1.2.2	Our approach	20
		1.2.3	The Nambu-Jona-Lasinio model	20
		1.2.4	Quark-meson model	22
	1.3	Inhom	logeneous phases	23
		1.3.1	Mixed phases	23
		1.3.2	Inhomogeneous condensates	24
	1.4	Neutro	on stars	26
		1.4.1	Composition	26
		1.4.2	Mass and radius	28
2	Stra	nge Ou	ark Matter from a baryonic approach	31
_	2.1	_	uction	31
	2.2			34
		2.2.1	Lagrangian	34
		2.2.2	Free energy and stationarity equations	37
		2.2.3	Speed of sound	39
	2.3		eter choices	42
		2.3.1	Saturation properties	42
		2.3.2	Couplings between hyperons and vector mesons	45
	2.4	Result	S	47
		2.4.1	Selected parameter sets	48
			2.4.1.1 Chiral transition and onset of strangeness	48
			2.4.1.2 Speed of sound and mass-radius curves	53
		2.4.2	Parameter-independent conclusions	58
	2.5		ary	62
2	Chi	ral arose	cover we chiral density wave in nuclear matter	65

vi CONTENTS

3.1	Introd	uction	65
	3.1.1	Background and motivation	65
	3.1.2	Model and main idea	67
	3.1.3	Main novelties	68
	3.1.4	Structure of the chapter	69
3.2	Mode	l and ansatz	69
	3.2.1	Lagrangian	69
	3.2.2	Ansatz and mean-field approximation	70
	3.2.3	Free energy	73
	3.2.4	Stationarity equations	78
	3.2.5	Fitting parameters	78
3.3	Result	S	81
	3.3.1	Isotropic matter: absence of first-order transition due to Dirac sea	81
	3.3.2	CDW solution	83
	3.3.3	Locating the CDW in the parameter space	86
	3.3.4	Comparison with different approaches to the Dirac sea	89
3.4	Summ	nary	92
4 Cor	nclusior	and Outlook	95
Appen	dix A	Chiral setup	99
Appen	dix B	Asymptotic flavor symmetry	105
Appen	dix C	Computing the Dirac sea contribution	109
Apı	oendix (C.1 Regularization	109
App	endix (C.2 Renormalization	111
		C.3 Matter contributions to densities and axial current	115
Appen	dix D	Model parameters	119
Refere	nces		121

Declaration of Authorship

I declare that this thesis and the work presented in it is my own and has been generated by me as the result of my own original research.

I confirm that:

- 1. This work was done wholly or mainly while in candidature for a research degree at this University;
- 2. Where any part of this thesis has previously been submitted for a degree or any other qualification at this University or any other institution, this has been clearly stated;
- 3. Where I have consulted the published work of others, this is always clearly attributed;
- 4. Where I have quoted from the work of others, the source is always given. With the exception of such quotations, this thesis is entirely my own work;
- 5. I have acknowledged all main sources of help;
- 6. Where the thesis is based on work done by myself jointly with others, I have made clear exactly what was done by others and what I have contributed myself;
- 7. Parts of this work have been published as: Eduardo S. Fraga, Rodrigo da Mata, Savvas Pitsinigkos, and Andreas Schmitt. Strange quark matter from a baryonic approach. *Phys. Rev. D*, 106(7):074018, Oct 2022.

 Savvas Pitsinigkos and Andreas Schmitt. Chiral crossover versus chiral density wave in dense nuclear matter. *Phys. Rev. D*, 109:014024, Jan 2024.

Signed:	Date:

Acknowledgements

The past years changed me as a person, and I want to thank the people who stood by my side and made sure that these changes were the best ones possible. Each of you played a vital role in my personal growth.

I want to first thank my supervisor, Andreas Schmitt. He provided guidance when I was lost, as well as motivation and encouragement when I didn't have any. He was patient through every late afternoon meeting and last-minute deadline rush, and accommodated us working in different time zones. Most importantly, his door was always open. I am grateful that I had the luck to be supervised by him.

I would also like to thank my family. My parents, Dimitris and Dora, have always supported me in their own unique way. They sparked and nurtured my interests, and I often find parts of them within me. My sister, Alkmene, has always challenged me – and continues to do so. She is the reason I developed the patience and persistence needed to tackle difficult problems.

I could not have completed this work without the unwavering support of my partner, Kyriaki, who not only carried the weight of her own Doctoral study, but also put a shoulder under my own weight at every chance she had. She always found a way to pull me towards the light and put a smile on my face.

Special thanks are due to the people with whom I first embarked on my journey in Physics. They inspired me and they still do, after countless hours of conversations on Physics and life. I would not be where I am today without having discovered this beauty alongside you. Thank you Christos, Marios, George and Chris – may we never stop having these conversations.

X CONTENTS

To the people that welcomed me in the office when I first came. They showed me how to survive the British weather and how to get to love Southampton. They are Alex (the Mathematica wizard), Enrico (the wise), Davide (the composed) and Daniel (the eloquent). Thank you for making me feel at home.

To those who joined the office later – Jack, David, Jon, Javi, and Alex – you kept me happily distracted and made me never want to leave. A special thanks to Orestis (the true Π), who became my home away from home and ensured I never felt homesick.

The people in the neutron stars group – especially Geraint, Shanshan, Marcus, and Thomas – were always there to chat about our common worries. You helped me realize that I wasn't the only one struggling, and that there is always hope. Thank you for listening to my troubles.

Finally, I want to thank some friends who offered me invaluable support, each in their own way, whether near or far, by patiently listening to my concerns. Thank you, Giannis and Panos, for gaming with me; thank you, Tommy, for your concern and for always reaching out; and thank you, Christina, for introducing me to bubble tea.

	,
V	٦
А	П

To those who helped me pursue my dreams...

Chapter 1

Introduction

How does matter behave when compressed to the extreme? What is the composition of a neutron star? Is there a way that we can find answers here on Earth? These are the questions that I will try to tackle in this thesis. We will mainly be concerned about the thermodynamics of Quantum Chromodynamics, which is the theory that holds a great portion of the answers to the questions we asked.

We shall begin with reviewing some basics of the theory. We will discuss the symmetries and symmetry breaking patterns. Then, a brief recap of the ideas of Chiral Effective field theory is presented. We then turn to the phase diagram of Quantum Chromodynamics and the open questions that still remain. We will continue by presenting our approach to answer these open questions and also similar approaches employing phenomenological models. At the end of the introduction we will discuss some special cases of inhomogeneous phases, and at last give some background in neutron star physics. In Chapter 2 we present a nucleon-meson model that includes strangeness via hyperons and attempts to paint a simplified picture of the phase structure of strong interactions. In Chapter 3 a simpler model is employed to shed new light over the possibility of a certain inhomogeneous phase is the ground state of the nuclear medium. Finally, we conclude the thesis by drawing some conclusions from our results, and also providing some outlook.

Note that, unless otherwise stated, we will be working in units where $c = \hbar = k_B = 1$. Also, the work presented in Chapters 2 and 3 has been taken from publications that were completed during my doctoral candidacy [1, 2].

1.1 Quantum Chromodynamics

Quantum Chromodynamics (QCD) is the theory that describes the strong interactions between quarks and gluons. These are the constituents of all hadrons, but quarks and gluons have very different properties from hadrons. Whatever these differences may be, QCD is the underlying theory describing the strong force, and so in principle the full hadron spectrum with its properties and interactions should be subject to the rules of that theory. Let us start by writing down the Lagrangian of the theory

$$\mathcal{L} = -\frac{1}{4} G_a^{\mu\nu} G_{\mu\nu}^a + \sum_{\alpha} \bar{\psi}_j^{\alpha} (i \not D_{jk} - m^{\alpha} \delta_{jk}) \psi_k^{\alpha}, \tag{1.1}$$

where the quark fields ψ_j^{α} have N_f flavors $\alpha = u, d, ...$ and 3 colors j = 1, 2, 3 and also the gluons A_u^a have a color index a = 1, ... 8. Moreover,

$$G_{\mu\nu}^a = \partial_\mu A_\nu^a - \partial_\nu A_\mu^a - g f^{abc} A_\mu^b A_\nu^c, \tag{1.2}$$

is the gluon field strength tensor, g is a coupling constant and f^{abc} are the structure constants of SU(3). The covariant derivative matrix with color indices j,k is

$$D_{\mu}^{jk} = \left(I_3^{jk} \partial_{\mu} + igA_{\mu}^a \frac{\lambda_a^{jk}}{2}\right),\tag{1.3}$$

with λ_a (a=1 to 8) being the SU(3) generators (Gell-Mann matrices). This is the simple theory that in principle describes the comparatively complex structure of QCD that we will discuss in the next chapters. However, calculating the said structure from first principles is not a small feat.

One of the main reasons for this difficulty is the strong coupling phenomenon of color confinement. To discuss it, think of QCD as an effective low-energy theory, only applicable up to some cutoff Λ , from where on another "full theory" extends it. Theories that are renormalizable (like QCD) have no regard about their ultraviolet completion (beyond the scale Λ). This means that they boil down to an effective description where all of their details are encoded to a finite set of free parameters that are measurable at some low energy scale E. The renormalization procedure describes how one can integrate the effects of the theory in the scales between (E,Λ) and encode them in the coupling "constants" of the effective theory, which now depend on E.

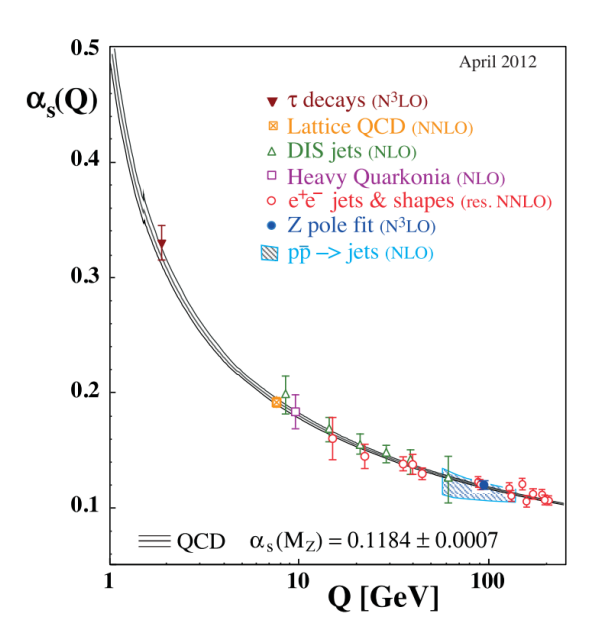


FIGURE 1.1: Energy dependence of the effective coupling ($\alpha_s \propto g$) in QCD. For every energy scale a suitable renormalization scale must be chosen for the theory (Q = E). Figure taken from [5]

Having in mind the coupling constant g from (1.3) in particular, say we want to calculate how it is affected by the change of the energy scale E. This is encoded in the beta-function, which for QCD to 1-loop accuracy is

$$\beta_{\text{QCD}} = E \frac{\partial g}{\partial E} = -\left(11 - \frac{2N_f}{3}\right) \frac{g^3}{16\pi^2} + \mathcal{O}(g^5). \tag{1.4}$$

The negative pre-factor (for the physical case of $N_f = 6$) hints that the coupling strength g becomes smaller as the energy at which we evaluate our effective theory increases. Following this trend, we expect that at very high E, the coupling constant reduces to very small values, resulting to a theory of approximately free quarks and gluons (asymptotic freedom [3, 4]). This is demonstrated in Fig. 1.1, In this regime the usual field theoretic perturbative methods can be applied.

On the contrary, moving to lower *E*, the coupling is expected to increase to the point that the theory becomes strongly coupled and non-perturbative effects dominate. One such effect is the confinement of quarks and gluons within color-less hadrons. Hadrons are the relevant degrees of freedom in the QCD vacuum.

1.1.1 Symmetries of QCD

We will now discuss some important symmetries of the theory. The first one is the invariance of the Lagrangian with respect to non-abelian gauge transformations, which is the color symmetry. A transformation of a quark spinor can be written as

$$\psi \to e^{i\lambda_a \theta^a(x)} \psi, \tag{1.5}$$

and the invariance is achieved by the corresponding transformation of the gluon field

$$A_u^a \to A_u^a + D_\mu \theta^a(x). \tag{1.6}$$

The conserved charge corresponding to this symmetry is the color charge.

There are also invariances of the Lagrangian with regard to global transformations. To discuss them consider the following. In QCD we observe 6 quark flavors, where their mass spectrum spans 5 orders of magnitude. We can differentiate 3 "heavy" (c, b, t) and 3 "light" (u, d, s) flavors, where former ones having masses in excess of 1 GeV and the latter ones have masses smaller than 100 MeV. We want to discuss the symmetries of the theory in the limit of vanishing light quark mass, the *chiral limit*. For this purpose let us introduce the projection operators

$$P_R = \frac{1+\gamma_5}{2}, \quad P_L = \frac{1-\gamma_5}{2},$$
 (1.7)

which can be used to split the spinors to their left-handed and right-handed components

$$\psi_{R/L} \equiv P_{R/L}\psi, \quad \psi = \psi_L + \psi_R. \tag{1.8}$$

We can now write the QCD Lagrangian in zero light quark mass limit

$$\mathcal{L} = -\frac{1}{4} G_a^{\mu\nu} G_{\mu\nu}^a + \sum_{\alpha = \text{heavy}} \bar{\psi}_j^{\alpha} (i \mathcal{D}_{jk} - m^{\alpha} \delta_{jk}) \psi_k^{\alpha} + \sum_{\alpha = \text{light}} \bar{\psi}_j^{\alpha} i \mathcal{D}_{jk} \psi_k^{\alpha}. \tag{1.9}$$

The latter term can be written as

$$\sum_{\alpha = \text{light}} \bar{\psi}_{j}^{\alpha} i \mathcal{D}_{jk} \psi_{k}^{\alpha} = \sum_{\alpha = \text{light}} \left(\bar{\psi}_{j,L}^{\alpha} i \mathcal{D}_{jk} \psi_{k,L}^{\alpha} + \bar{\psi}_{j,R}^{\alpha} i \mathcal{D}_{jk} \psi_{k,R}^{\alpha} \right). \tag{1.10}$$

In this form it is clear that the flavor symmetry group of the theory appears to be

$$U(3)_L \times U(3)_R, \tag{1.11}$$

that is symmetry with respect to rotations in the 3 dimensional "light" flavor space, independently for left and right handed spinors, i.e.

$$\psi_R \to e^{i\phi_R^a \lambda_a} \psi_R, \quad \psi_L \to e^{i\phi_L^a \lambda_a} \psi_L, \tag{1.12}$$

where now $\lambda_0 = I_3$. Since $U(N) \cong SU(N) \times U(1)$, this group can be decomposed to

$$SU(3)_L \times SU(3)_R \times U(1)_B \times U(1)_A. \tag{1.13}$$

The first two components, $SU(3)_L \times SU(3)_R$ form the *chiral symmetry* group. The remaining components are the vector $U(1)_B$ which contains transformations of the form

$$\psi \to e^{i\theta}\psi,\tag{1.14}$$

and axial-vector $^{1}U(1)_{A}$ containing transformations

$$\psi \to e^{i\theta\gamma^5}\psi. \tag{1.15}$$

The conserved charge for $U(1)_B$ is the baryon number.

Regarding $U(1)_A$, the story is more subtle. While such a transformation appears to be an invariance of the lagrangian, the symmetry is broken on a quantum level. That is, if one tries to calculate loop corrections² to the axial current, they find that is is actually not conserved. The calculation (to 1-loop) yields

$$\partial_{\mu} J_{0,A}^{\mu} = -\frac{g^2 N_f}{16\pi^2} G_{\mu\nu}^a \tilde{G}_a^{\mu\nu}.$$
 (1.16)

As a result, the symmetry group of QCD in the chiral limit is

$$SU(3)_L \times SU(3)_R \times U(1)_B \times U(1)_A.$$
 (1.17)

¹The names come from the parity transformations of the corresponding conserved charges.

²Specifically the so-called triangle diagrams.

Another noteworthy approximate symmetry arises when one considers QCD with only two quarks, (say u and d), where they have the same mass. In this case we discover an extra SU(2) symmetry, the *isospin symmetry*. An isospin transformation can be written as

$$\begin{pmatrix} u \\ d \end{pmatrix} \to e^{i\theta^a \tau_a} \begin{pmatrix} u \\ d \end{pmatrix}, \tag{1.18}$$

where τ_a are the Pauli matrices.

Finally, let us discuss about a theory related to QCD, pure Yang-Mills. Pure Yang-Mills theory is also constructed upon an $SU(N_c)$ symmetry, and for $N_c=3$ it is the free gluon sector of QCD

$$\mathcal{L}_{YM} = -\frac{1}{4} G_a^{\mu\nu} G_{\mu\nu}^a. \tag{1.19}$$

However, QCD theory is not the same theory as pure Yang-Mills. In the infinite quark mass limit, where quark states are never populated and all quark propagators in diagrams are infinitely suppressed, QCD calculations should converge to those in Yang-Mills.

We are specifically interested on the center symmetry of Yang-Mills. That is symmetry with respect to transformations generated by the center of SU(3), the subgroup of elements that commute with all elements of the group. This manifests in an Euclidean space where the "time" dimension τ is periodic, which is the finite temperature framework that thermal field theory employs. There is a quantity that spontaneously breaks center symmetry when it dynamically acquires a non-zero value. That is the Polyakov loop.

Let's first define a Wilson line as the path ordered exponential³

$$w_{if} = \hat{P} \exp\left(i \int_{\vec{x}_i, \tau_i}^{\vec{x}_f, \tau_f} A_{\mu} dx^{\mu}\right), \tag{1.20}$$

for some path $(\Delta \vec{x}, \Delta \tau)$. Then, the Polyakov loop is defined as the trace of a Wilson line along a straight path in the imaginary τ direction

$$\Phi(\vec{x}) = \frac{1}{3} \text{Tr} \left[\hat{T} \exp \left(i \int_0^\beta d\tau \, A_0(\vec{x}, \tau) \right) \right], \tag{1.21}$$

³Path ordering \hat{P} is a generalization of time ordering \hat{T} where operators are ordered with respect to the parameter that parametrizes the path.

where $\beta=1/T$ is the length of the compact "time" dimension. The usefulness of the Polyakov loop is that it quantifies the free energy cost ΔF to add a static color source (an infinitely heavy quark) in the system (subtracting the mass contribution itself)

$$|\Phi(\vec{x})| = e^{-\Delta F \beta}. \tag{1.22}$$

From the above relation it is evident that the when the energy cost is 0 then the Polyakov loop is 1, but as $\Delta F \to \infty$ the value of the loop vanishes. The Polyakov loop is an order parameter for color confinement in Yang-Mills theory. When it vanishes, the ground state of the system is "center symmetric" and it is infinitely expensive to add color charge to the system (color confinement). Conversely, when $|\Phi(\vec{x})| = 1$ then the center symmetry is spontaneously broken, and there is no free energy cost associated with the addition of color charges.

The benefit of examining pure Yang-Mills theory is that it provides a well-defined order parameter for confinement. Whether this is transferable to real QCD is not an easy question to answer.

After this discussion where we considered close relatives of QCD, we must not forget where we started from. Quarks are neither infinitely massive nor massless. The physical reality we observe lies somewhere in the middle. Quarks have finite, distinct masses. This has the following implications for QCD:

- Isospin symmetry is explicitly broken due to the *u* and *d* mass splitting.
 However, the mass splitting is in the order of MeV so the symmetry breaking implications should be small.
- Center symmetry is explicitly broken, this time by the non infinite value of the
 quark masses, and it is unclear whether it is a good order parameter for the color
 confinement observed in QCD.
- Chiral symmetry is explicitly broken by the non-zero u, d and s quark masses.
 Again, the symmetry breaking is small so we expect the symmetry to be a reasonable approximation.

Finally, the chiral symmetry is also spontaneously broken in the QCD vacuum. This is a physical observation that cannot be seen directly in the lagrangian. The QCD

vacuum assumes a non zero chiral condensate value $\langle \bar{\psi}\psi \rangle$, which is a condensate of quark-antiquark pairs. The non-zero chiral condensate is responsible for the relatively large mass of the confined states like the nucleon $m_N \approx 1$ GeV. Moving away from the QCD vacuum, the chiral condensate (approximately) vanishes as we move towards the (approximate chirally symmetric) quark phase of QCD. This establishes an apparent connection between chiral symmetry and center symmetry. Center symmetry breaking separates colored from uncolored phases and chiral symmetry breaking separates heavy baryons from light quarks. Either may be used to signify the quark-hadron transition, but we have to remember that the Polyakov loop and the chiral condensate are a "strict" order parameter at different limit scenarios of QCD.

We also know from the Goldstone Theorem [6–10] that when a global continuous symmetry is spontaneously broken we get a number of massless Goldstone bosons that is equal to the amount of generators of the broken symmetry. In this case, if we treat the quarks as having non-zero but equal masses $m_u = m_d = m_s$, we find that the symmetry breaking pattern is

$$SU(3)_L \times SU(3)_R \rightarrow SU(3)_{L+R}.$$
 (1.23)

That means that the theory is still invariant under simultaneous rotations of the left and right handed components. Since SU(3) has 8 generators, the spontaneous symmetry breaking gives rise to 8 Goldstone modes. These Goldstone modes are the pseudoscalar octet, written in Eq. (A.2a). They are not massless due to the finite quark mass and thus the small explicit chiral symmetry breaking.

In the above we have used the word "small" and "large" somewhat loosely when referring to masses and deviations from symmetry. We need an energy scale Λ_{χ} to compare it with, and this will be provided section 1.1.2.

In other cases condensates that manifest in the ground state of the system may spontaneously break additional symmetries of the theory. These can be a condensate of fermion pairs in fermionic superfluids that breaks $U(1)_B$ (baryon number conservation), or even an inhomogeneous condensate that spontaneously breaks Poincaré symmetry.

1.1.2 Chiral effective field theory

Chiral effective field theory (ChEFT) is an effective description of QCD. It is a framework that approximates low energy QCD in a controlled manner, i.e. calculations can (in principle) be made up to the required precision. The description is built around the lowest mass hadrons, which are the pions. Their mass set the "soft" scale of the theory $Q=m_\pi\approx 140\,\mathrm{MeV}$. The "hard" scale Λ_χ of the theory, where extra degrees of freedom appear, is set by the lightest vector mesons ρ and ω with $m_{\rho,\omega}\approx 775\,\mathrm{MeV}$. The scale is chosen to be $\Lambda_\chi\approx 1\,\mathrm{GeV}$ and it is called the chiral symmetry breaking scale.

To construct the effective theory we want to write the most general Lagrangian that is consistent with the symmetries and symmetry breaking patterns of low energy QCD. The relevant degrees of freedom are pions and nucleons. It is convenient to decompose the lagrangian as

$$\mathcal{L}_{\text{ChEFT}} = \mathcal{L}_{\pi\pi} + \mathcal{L}_{\pi N} + \mathcal{L}_{NN} + \dots, \tag{1.24}$$

where $\mathcal{L}_{\pi\pi}$ contains only pion terms, $\mathcal{L}_{\pi N}$ pion-nucleon interactions and \mathcal{L}_{NN} two nucleon interactions. The ellipsis stands for extra terms that include higher number of nucleons and pions, encoding many-body interactions. The idea is that, given a small parameter λ , we can write an expansion for these terms that makes sense to be truncated at some order of the small parameter. The scale separation gives us natural choice of

$$\lambda = \frac{Q}{\Lambda_{\chi}}.\tag{1.25}$$

Now, it is also convenient to introduce the pions via the SU(2) flavor matrix

$$U = \exp\left(\frac{i\tau \cdot \pi}{f_{\pi}}\right). \tag{1.26}$$

We can now work out and write the leading order contribution. We have

$$\mathcal{L}_{\pi\pi}^{\text{LO}} = \frac{f_{\pi}^2}{4} \text{Tr} \left[\partial_{\mu} U \partial^{\mu} U^{\dagger} + m_{\pi}^2 (U + U^{\dagger}) \right]. \tag{1.27}$$

The first term is chirally invariant, but the second explicitly breaks chiral symmetry. The magnitude of the explicit breaking is chosen such that it reproduces the correct

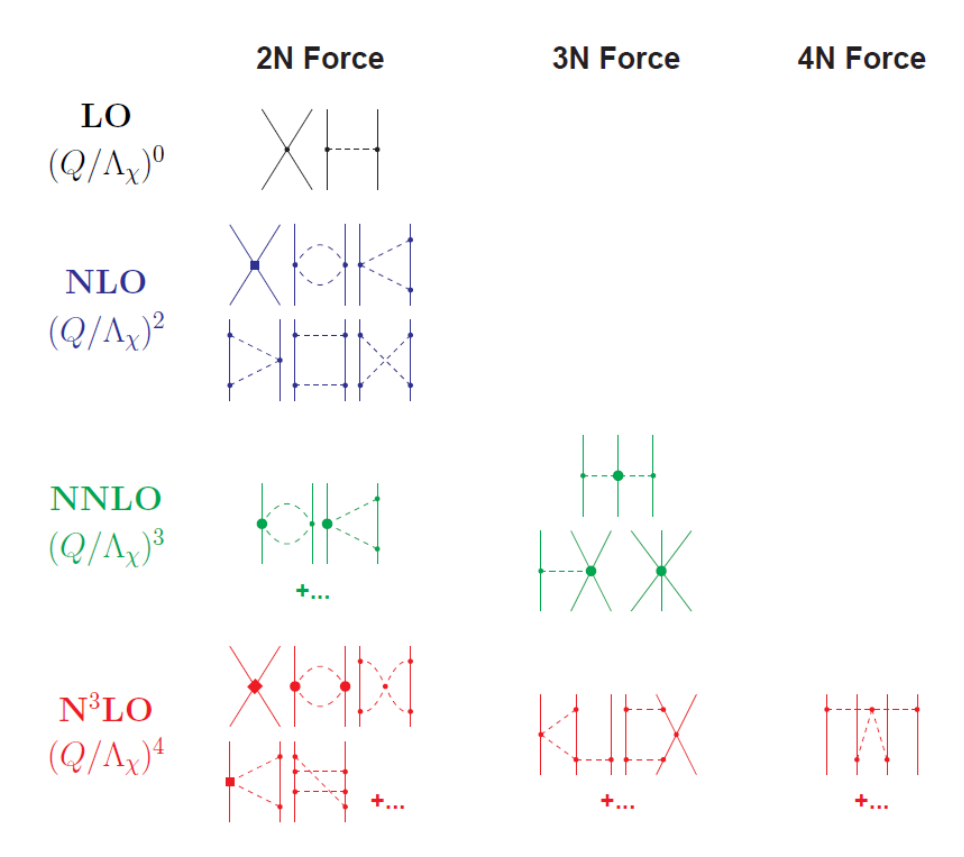


FIGURE 1.2: Diagrams contributing to the 2,3 and 4 nucleon interaction at different orders. At higher orders in the chiral expansion, many body interactions emerge naturally. Image taken from [11].

pion mass. We have thus ensured that we have broken chiral symmetry only "as much as" it is broken in QCD.

We will not write the leading order terms in $\mathcal{L}_{\pi N}$ and \mathcal{L}_{NN} here, but a more detailed description is provided in [11]. The takeaway is that the theory is able to provide a systematic way to approximate the QCD interaction between the relevant degrees of freedom in the low energy regime, given that the external momenta Q are small with regard to the chiral symmetry breaking scale Λ_{χ} . A pictorial representation of how the expansion parameter is enforcing a hierarchy on the Feynman diagrams describing the nuclear interaction can be seen in Fig. 1.2. A finite number of diagrams contribute to a given order in Q/Λ_{χ} .

While very useful, the applicability of ChEFT is limited to densities close to nuclear saturation density. Trying to go beyond quickly breaks the assumption about the smallness of λ and introduces great uncertainty to the predictions. However, we will later use ChEFT as "inspiration" to set up phenomenological models.

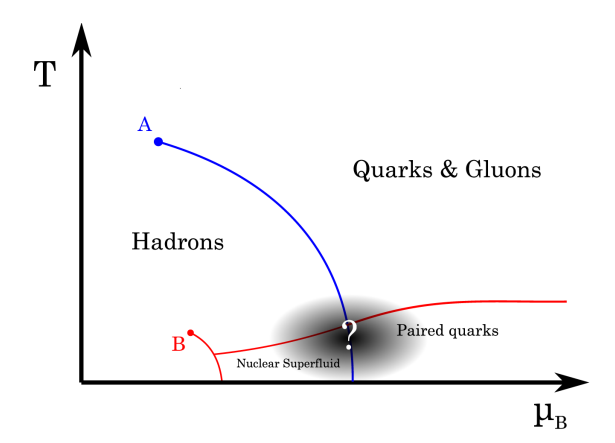


FIGURE 1.3: A plausible assumption for the form of the QCD phase diagram. The blue line is a first order chiral phase transition boundary, while red lines separate distinct phases within the quark and hadronic phases. Critical points are labeled *A* and *B*. The shaded region is there to remind us that the exact structure is unclear.

1.1.3 A phase diagram for Quantum Chromodynamics

A phase diagram for QCD can be seen in Fig. 1.3. It broadly sketches the proposed phase structure of the ground state of QCD, at different baryon chemical potentials μ_B and temperatures T. This is not "The" phase diagram for QCD as several questions remain unanswered. The marked phases and phase transitions are just a reasonable proposition of how the true phase diagram could be. Let us now review the features of this phase diagram.

A natural place to start is our everyday experience. But where is that exactly in the phase diagram? What is the scale on each axis? To answer that, we will look at the lightest particle in the QCD vacuum. That is the neutral pion, with a mass of about 135 MeV. Postulating that this is a relevant mass scale for QCD, we can translate it to temperature units dividing with Boltzmann's constant $k_B \approx 8.617 \cdot 10^{-5} \,\text{MeV/K}$, which gives us $\approx 1.57 \cdot 10^{12} \,\text{K}$. This is a strong hint that our everyday experience and most phenomena on Earth are at effectively 0 temperature, compared to the QCD scale.

What about the baryon chemical potential scale? The energy (per baryon) to create a nucleon pair in an empty system is the rest mass of the neutron itself $m_n \approx 940 \text{MeV}$, plus the interaction energy per baryon $E_B \approx -16 \text{ MeV}$. That means that only for values larger than $m_n + E_B$ we have baryons spontaneously populating the medium. The mass of the nucleon sets a rough scale for the creation of baryonic

matter around 1 GeV, and since we do not observe spontaneous creation of nucleons, it is safe to assume that the baryon chemical potential we experience is nowhere near that value. The only baryons that we observe in the vacuum are bound in the nuclei of atoms, forming a dilute atomic gas. Let's accept that our experience is consistent with a μ_B value of 0.

The main theoretical question that we are trying to answer is about the nature of the quark-hadron transition. We see that QCD in the vacuum is strongly coupled and confined in hadrons, and we know that asymptotically it is a theory of free quarks and gluons. What we want to understand is what happens in between, i.e. how to find the ground state of QCD in the middle of the phase diagram. Where do we need to draw lines between different phases, and what phases are these?

How do we probe different regions of the phase diagram then? Let's say we only want to explore the T direction for now, staying at $\mu_B = 0$. It is possible to numerically calculate QCD observables on the computer by discretizing the theory on an Euclidean lattice. Lattice QCD is non-perturbative and hence applicable even at strong coupling. Using lattice QCD it has been demonstrated that the deconfinement transition is an analytic crossover [12, 13], accompanied by a chiral phase transition at the same critical temperature $T_C \approx 156$ MeV [14].

However, it is not currently possible to use lattice QCD to extend the calculations on the μ_B direction. That is because of the notorious sign problem [15, 16] that prohibits the use of lattice methods for systems with a finite fermion density. This is the time to turn to experiments. While heavy-ion collision programs have been successful in probing the small μ_B , high T region of the phase diagram [17–20], there has been also an effort to extend their reach to larger μ_B as well. In these experiments two nuclei collide and can temporarily create a hot quark-gluon plasma. The experiments in CERN and RHIC have only found a crossover transition so far, but only probe very low μ_B . Currently, the BES experiment [21, 22] by the STAR collaboration in RHIC is attempting to extend the search to even higher μ_B . One hopes to find evidence of a first order phase transition boundary, or the terminating critical point associated with a second order transition (point A in Fig. 1.3) [23].

Nevertheless, the existence of such a critical point, along with a first order phase transition boundary is hypothesized [24, 25]. This is reflected by the blue line on

Fig. 1.3. It marks the chiral phase transition separating the hadronic and quark phases. It is drawn to extend all the way to zero T. But this may not be the case. There is the proposition of quark-hadron continuity [26] suggesting that there is only a crossover transition between nuclear and quark phases. This idea is backed by the fact that there is no strict symmetry breaking for the chiral symmetry since it is explicitly broken by the non-zero quark masses. So it is plausible that the line stops at an extra critical point (not shown), or that it is never there altogether.

The issue is that this region of intermediate μ_B and low T is computationally difficult to tackle. The sign problem is severe for high μ_B , and the temperature is too low to be probed by heavy-ions. But there is a physical system that contains matter in a state corresponding to this region of the phase diagram. That is Neutron stars, and their micro-physics are governed by dense, low temperature QCD. We will discuss how they provide insight to this diagram in 1.4.2.

What we can try to do is approach this regime from different directions. Starting at low μ_B and zero T, we find ourselves in the QCD vacuum. Increasing μ_B we reach the point of the liquid-gas transition [27, 28]. At this point the ground state shifts from a hadron gas with approximately zero density to a uniform nuclear medium of density $n_0 \approx 0.15 \,\text{MeV/fm}^3$ [29]. This is nuclear matter at its saturation density, which is the density of the nuclear medium within nuclei. This density region is accessible to Earth experiments which enable us to measure properties of QCD matter. These are quantities like the binding energy E_B [30], incompressibility K [31], symmetry energy S [32] and slope parameter of the symmetry energy L [33]. By increasing T while following the liquid-gas transition line, we find ourselves in another critical endpoint. For higher T the transition becomes a crossover.

Extending our predictions to significantly higher densities is very difficult. We are facing a strongly coupled system of nucleons that needs to be described in a dedicated framework. We will show how we attack this problem by employing phenomenological models in 1.2.

Despite the strong coupling, non perturbative calculations of the neutron pairing gap have shown that nucleons are paired in the ground state of the system for low temperatures[34–36]. At higher *T* the pairing gap closes and superfluidity is lost.

Different forms of superfluidity are also possible [37]. This is an indication that the ground state of the system might be significantly more complicated.

Skipping the troubling region altogether, we turn to very large μ_B . We know that QCD is asymptotically free, and thus when $\mu_B \gg \Lambda_\chi$ we will get to that limit. Asymptotic freedom enables us to employ perturbative methods around the free quark-gluon system. In this setting, the one gluon exchange interaction provides the attractive interaction component necessary to form quark Cooper pairs. The quark-quark condensate cannot be color-less and hence spontaneously breaks the $SU(3)_c$ symmetry. Due to the perturbative nature of this limit, it can be shown that the ground state of the theory is the Color-Flavor locked (CFL) phase [38]. In this phase all 3 light quarks of all 3 colors pair with one another. The "locked" part of the name comes from the fact that the CFL phase is symmetric only under simultaneous transformations of flavor and color

$$SU(3)_L \times SU(3)_R \times SU(3)_c \times U(1)_B \rightarrow SU(3)_{L+R+c}.$$
 (1.28)

As we move towards lower μ_B , the mass difference between the s and u, d quarks becomes more important. This imposes a stress on the pairing pattern and tends to disrupt it. Other candidate superconducting quark phases might become preferred. One example is the 2SC phase where the u and d quarks of only 2 colors pair [39]. Another one is the Fulde–Ferrell–Larkin–Ovchinnikov phase [40, 41] (FFLO) where the diquark condensate is inhomogeneous. There are many possibilities to be explored ([42] and references therein) and us entering in the strong coupling regime of QCD means that we can only be sure about the asymptotic result of the stability of CFL. Again, for sufficiently high temperatures, the quark pairing gap closes and superconductivity is lost.

Finally, it is necessary to stress that this phase diagram is not "all there is". We could escape the 2D plane (μ_B , T) and ask how does the phase structure of QCD change when we move in a new direction. One important such direction is that of the isospin chemical potential μ_I which introduces an isospin charge in the system. This is a crucial direction for neutron star physics, where matter is highly isospin asymmetric (many more neutrons than protons). Nuclei on the contrary, even heavy ones, have a very comparable number of protons and neutrons, and so the isospin charge of the

system is small. One may also argue that neutron stars spin and have large magnetic fields. While in the context of heavy ion collisions it may be an interesting question to ask "what is the ground state of the QCD medium under extreme rotation Ω or magnetic field B?", it turns out that neutron stars are not as "extreme". Their typical Ω and B values are typically very small in the QCD scale. However, there are scenarios where this claim possibly needs to be reevaluated, namely magnetars [43] and heavily turbulent regions in neutron star mergers [44].

The importance of the nature of the chiral phase transition is beyond the academic interest of the completeness of the phase diagram. If the quark-hadron transition is of first order, this has implications not only for the thermodynamics of the system, but for the dynamical evolution of it as well. Imagine that a supernova explosion gives birth to a neutron star that has a large enough central density to surpass the critical density of a first order quark-hadron transition. That does not mean that the core will immediately contain quark matter. The hadronic system will exist in a false vacuum for a while, trapped by the potential barrier set by the first order phase structure. This meta-stable state will eventually decay to the true vacuum via bubble nucleation. Bubbles of the true vacuum appear and grow in the meta-stable phase, until the full volume of the system is in the true vacuum. In order to phenomenologically describe this procedure we need to determine an important parameter: the *surface tension* associated with an interface between the two phases. In order to calculate it we need a model that contains the chiral phase transition itself, like the ones used in Chapters 2 and 3.

1.2 Phenomenology

We have already hinted that the low temperature and intermediate density region is one of the most elusive ones as there are no first principle approaches that can be applied. This is why we employ some phenomenological model to try and tackle this problem. To put together an appropriate model we need to consider the relevant degrees of freedom, the symmetries of the theory and well established experimental results. However, we will not be as rigorous as ChEFT is, since we are aiming for a wider range of applicability. What we are sacrificing in the process though is the well defined "error bars" that ChEFT provides. As a result our analysis has the purpose to

explore the qualitative possibilities that might be realizable in QCD, rather than to make a strict quantitative prediction.

1.2.1 The Walecka model

The Walecka model [45] is a simple microscopic model that attempts to describe nuclear matter at high densities. It is in principle a very simplistic way to model nuclear matter, but is a nice paradigm that demonstrates the basic ingredients of phenomenological models. The lagrangian of the model is written as

$$\mathcal{L} = \sum_{j=n,p} \bar{\psi}_{j} (i\gamma^{\mu}\partial_{\mu} - m_{N} + \mu_{j}\gamma^{0})\psi_{j} + \frac{1}{2}(\partial_{\mu}\sigma\partial^{\mu}\sigma - m_{\sigma}^{2}\sigma^{2}) - \frac{1}{4}\omega_{\mu\nu}\omega^{\mu\nu} + \frac{1}{2}m_{\omega}^{2}\omega_{\mu}\omega^{\mu} + \sum_{j=n,p} \bar{\psi}_{j} (g_{\sigma}\sigma + g_{\omega}\gamma^{\mu}\omega_{\mu})\psi_{j}, \tag{1.29}$$

where $\omega_{\mu\nu}=\partial_{\mu}\omega_{\nu}-\partial_{\nu}\omega_{\mu}$ and m_N , μ_j are the nucleon mass and chemical potential. This model describes protons and neutrons interacting via meson exchange, particularly the scalar σ and the vector ω mesons. They are coupled to the baryons through Yukawa-type terms. The meson masses are $m_{\omega}\approx 782$ MeV and $m_{\sigma}\approx 500$ MeV.

Since we will explore the system at different densities, we will use the grand-canonical ensemble where the chemical potential is part of the description of the thermodynamic system. The Grand Potential (or free energy) Ω is given by

$$\Omega = E - \sum_{j} \mu_{j} N_{j} - TS, \tag{1.30}$$

where E is the energy of the system, N_j is the particle number, S is the entropy and T is the temperature. This expression can be written in terms of intensive quantities if we divide by the system volume V

$$\frac{\Omega}{V} = -P = \epsilon - \sum \mu_j n_j - Ts, \qquad (1.31)$$

where $\epsilon = E/V$ is the energy density, $n_j = N_j/V$ is the number density and s = S/V is the entropy density.

The partition function Z and the free energy Ω of the system are related through

$$\Omega = -T \ln Z. \tag{1.32}$$

To compute the partition function one needs to calculate the functional integral

$$Z = \int \sum_{j} \mathcal{D}\bar{\psi}_{j} \mathcal{D}\psi_{j} \mathcal{D}\sigma \mathcal{D}\omega \exp \int_{X} \mathcal{L}, \qquad (1.33)$$

where we have denoted (in the imaginary time formalism $t \to i \tau$, $\beta = \frac{1}{T}$)

$$\int_{X} \equiv \int_{0}^{\beta} d\tau \int d^{3}x. \tag{1.34}$$

In principle one calculates the functional integral and finds the free energy. However, when the Lagrangian contains interactions it is very hard to solve the integral. This is where the first approximation is employed. That is the mean field approximation, in which the meson fields are written as the sum of some space independent condensate plus fluctuations

$$\sigma \to \bar{\sigma} + \sigma,$$
 (1.35)

$$\omega_{\mu} \to \bar{\omega}_0 \delta_{0\mu} + \omega_{\mu}, \tag{1.36}$$

and then the fluctuations are neglected. Note that for the case of the vector meson we assumed that only the zero component ω_0 condenses. In doing so, the meson field condensates act as medium contributions to the nucleon chemical potential and mass.

The mean field Lagrangian is written as

$$\mathcal{L} = \sum_{j=n,p} \bar{\psi}_j (i\gamma^{\mu}\partial_{\mu} - m_N^* + \mu_j^* \gamma^0) \psi_j + \frac{1}{2} \partial_{\mu} \bar{\sigma} \partial^{\mu} \bar{\sigma} - \frac{1}{2} m_{\sigma}^2 \bar{\sigma}^2 - \frac{1}{4} \bar{\omega}_{\mu\nu} \bar{\omega}^{\mu\nu} + \frac{1}{2} m_{\omega}^2 \bar{\omega}_0^2,$$
 (1.37)

where

$$m_N^* \equiv m_N - g_\sigma \bar{\sigma}, \quad \mu_j^* \equiv \mu_j - g_\omega \bar{\omega}_0.$$
 (1.38)

The mean field approach is simplifying our task when considering the bosonic integration, but there are cases where this is not enough. In order to integrate the fermionic part and due to the coupling with the meson condensates, it is assumed that there is no spatial dependence of the latter. However, after the fermionic integration,

we re-introduce the space dependence in the resulting free energy by hand. This is the Thomas-Fermi approximation, and is valid when the condensates vary slowly in space.

Now we are ready to perform the functional integration of the free fermionic part (since we neglected fluctuations, the mesonic part decouples from the fermions, modulo the modified parameters m_N^* and μ^*)

$$Z = \exp\left[\frac{V}{T}\left(-\frac{1}{2}m_{\sigma}^{2}\bar{\sigma}^{2} + \frac{1}{2}m_{\omega}^{2}\bar{\omega}_{0}^{2}\right)\right] \times$$

$$\times \int \mathcal{D}\bar{\psi}\mathcal{D}\psi \exp\left[\int_{X}\sum_{j=n,p}\bar{\psi}_{j}(i\gamma^{\mu}\partial_{\mu} - m_{N}^{*} + \mu_{j}^{*}\gamma^{0})\psi_{j}\right]. \tag{1.39}$$

The functional integration returns

$$Z = \exp\left[\frac{V}{T}\left(-\frac{1}{2}m_{\sigma}^2\bar{\sigma}^2 + \frac{1}{2}m_{\omega}^2\bar{\omega}_0^2\right)\right] \cdot \operatorname{Det}\left[\frac{G_n^{-1}(k)G_p^{-1}(k)}{T^2}\right],\tag{1.40}$$

where the determinant is taken over the Dirac space and over all of the momenta, and G^{-1} is the inverse nucleon propagator:

$$G_i^{-1}(k) = -\gamma^{\mu} k_{\mu} - \gamma_0 \mu_i^* + m_N^*. \tag{1.41}$$

The system pressure is proportional to the logarithm of the partition function as seen in Eq. 1.32. Then by using that for a diagonalizable matrix A

$$\log \operatorname{Det}(A) = \operatorname{Tr}(\log A), \tag{1.42}$$

we can calculate the logarithm of the determinant as a sum over Matsubara frequencies.

Performing the Matsubara sum and taking the thermodynamic limit we get the system pressure

$$P = -\frac{\Omega}{V} = \frac{T}{V} \ln Z = \left(-\frac{1}{2} m_{\sigma}^2 \bar{\sigma}^2 + \frac{1}{2} m_{\omega}^2 \bar{\omega}_0^2 \right) + P_N, \tag{1.43}$$

where P_N is the pressure of the nucleons

$$P_N \equiv 2\sum_{j} \int \frac{d^3 \mathbf{k}}{(2\pi)^3} \left[E_k + T \ln \left(1 + e^{-(E_k - \mu_j^*)/T} \right) + T \ln \left(1 + e^{-(E_k + \mu_j^*)/T} \right) \right], \quad (1.44)$$

with

$$E_k = \sqrt{k^2 + m_N^{*2}}. (1.45)$$

The factor of 2 in (1.44) accounts for the 2 spins, and the two logarithm terms account for particles and anti-particles. It is often the case that the vacuum contribution E_k is omitted, being considered a small contribution with no qualitative significance. However, as we will later see in Chapter 3 this is not always true, and in some cases this sea contribution is important. For now, we will drop it (no-sea approximation), but we will come back to it later.

We will now take the limit $T \to 0$. The antiparticle contribution to the pressure will vanish, and the particle pressure will pick up Θ -functions ensuring that there is a finite baryon pressure only if the chemical potential exceeds the Fermi energy. The nucleon pressure

$$P_N \xrightarrow{T \to 0} p_n(\mu_n^*, m_N^*) + p_p(\mu_p^*, m_N^*),$$
 (1.46)

where $p(\mu, m)$ is the individual fermion species pressure,

$$p(\mu, m) \equiv \frac{\Theta(\mu - m)}{8\pi^2} \left[\left(\frac{2}{3} k_F^3 - m^2 k_F \right) \mu + m^4 \ln \frac{k_F + \mu}{m} \right]$$
 (1.47)

with

$$E_F = \mu^* = \sqrt{k_F^2 + m_N^{*2}}. (1.48)$$

We have now worked out how the zero temperature pressure of a system is given as a function of the meson condensates and fermion chemical potentials. This system includes fermions (n, p) interacting with scalar and vector mesons (σ, ω) . In our works we include more fermion or meson species, but the procedure is essentially the same.

1.2.2 Our approach

We will dedicate a little time to point out some differences of our approach presented in Chapters 2 and 3 compared to the Walecka model.

The most crucial one is the fact that in the Walecka model there is an explicit constant mass term in the Lagrangian. The effective nucleon mass receives a contribution from the σ meson condensate, but chiral symmetry is explicitly broken by the constant term. On the contrary, in our approach we will not write a lagrangian mass term. The condensate of the σ field is playing the role of the chiral condensate, which dynamically generates the full nucleon mass. At the same time this means that when the σ condensate vanishes, the nucleons in our model become effectively massless, spontaneously "restoring chiral symmetry". The quotation marks are used because in our model as well chiral symmetry is explicitly broken, but with a small magnitude, consistent with that of QCD. Hence, the restoration of chiral symmetry is only approximate.

Another important difference is that in Chapter 2 we will require that the system is beta equilibrated and charge neutral, with the scope of applying our results to neutron stars. This means that our system will no longer have equal numbers of protons and neutrons, and it will acquire a net isospin charge n_I . It is then important to add ρ to the model, the iso-triplet vector meson that mediates isospin interactions.

Other choices that are different in our models include the addition of self interactions for the scalar and vector mesons, extra degrees of freedom containing strangeness and allowing for an anisotropic chiral condensate.

1.2.3 The Nambu-Jona-Lasinio model.

While we only considered nucleons and mesons in the phenomenological description, this is not the only possibility. We have, so far, used degrees of freedom that are relevant on the low density side of the chiral transition. What if we now try to obtain a complementary phenomenological description using quarks?

The Nambu-Jona-Lasinio (NJL) model has not been historically a quark model. It was a model for interacting nucleons as well [7, 8]. However, it has been later

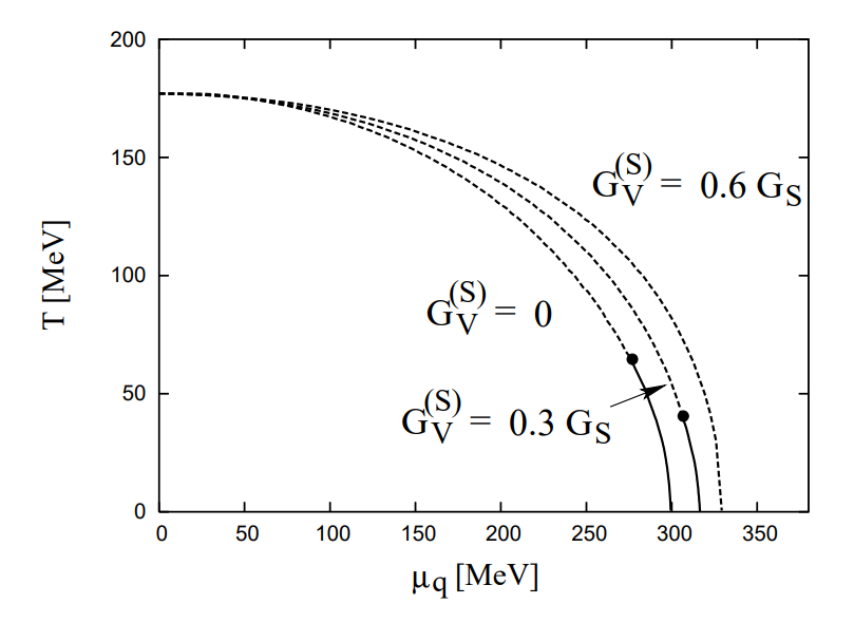


FIGURE 1.4: The phase diagram for the two flavor NJL model in the chiral limit with 0 net isospin. The line for $G_V^{(S)}$ applies to the model written in (1.49). The solid line marks a phase transition from a chirally broken (small T, μ_q) to a chirally restored phase (at large T, μ_q). The phase transition line has a critical endpoint at a finite temperature. Plot taken from [46]

re-interpreted as a model for quark interactions. The term "NJL model" actually describes a family of models that feature a four fermion contact interaction term. Such an example would be

$$\mathcal{L}_{\text{NJL}} = \bar{\psi}(i\partial \!\!\!/ - m + \mu_q \gamma^0)\psi + G_S\left[(\bar{\psi}\psi)^2 + (\bar{\psi}i\vec{\tau}\gamma_5\psi)^2\right],\tag{1.49}$$

where ψ is a two flavor, three color quark spinor, G_S is the coupling strength and μ_q is the quark chemical potential (equal for the two flavors, assuming isospin symmetric matter). In this model the quarks ψ acquire a dynamical mass

$$M = m - 2G_S \langle \bar{\psi}\psi \rangle, \tag{1.50}$$

which receives a contribution from a quark-antiquark condensate, i.e. the chiral condensate. This is what enables the model to exhibit spontaneous chiral symmetry breaking as well. A vanishing chiral condensate at large quark chemical potential μ_q corresponds to small effective masses for the quarks and (approximately) restored chiral symmetry, while a non-zero value (which occurs at small μ_q) corresponds to heavy quarks and spontaneous breaking of chiral symmetry. The chiral phase transition line is shown in Fig. 1.4 as an example.

This approach is complementary to the one we are going to observe in our model. In NJL we have quarks undergoing a chiral phase transition, while in our model it is nucleons that do so. The two models paint a picture on the opposite sides of the canvas that is the chiral phase transition.

1.2.4 Quark-meson model

A much more similar construction to the Walecka model would be a quark-meson model. We keep the idea of using mesons to mediate the nuclear interaction, but now the degrees of freedom are quarks. We can write down a lagrangian for such a model as

$$\mathcal{L}_{QM} = \bar{\psi} \left[i \partial \!\!\!/ + g(\sigma + i \vec{\tau} \cdot \vec{\pi} \gamma_5 + \mu_q \gamma^0) \right] \psi + \frac{1}{2} (\partial_\mu \sigma)^2 + \frac{1}{2} (\partial_\mu \vec{\pi})^2 + U(\sigma^2 + \vec{\pi}^2), \quad (1.51)$$

where the three pion fields are included in $\vec{\pi}$, ψ is again a two flavor, three color quark spinor, and μ_q is again the quark chemical potential. There is also some meson self-interaction potential that, in the simplest form, can be something like

$$U(\phi) = \frac{m^2}{2}\phi + \frac{\lambda}{4}\phi^2, \quad \phi = (\sigma^2 + \vec{\pi}^2).$$
 (1.52)

The condensate of the σ field here is also interpreted as the chiral condensate, and it will provide a dynamical mass to the quarks that spontaneously breaks chiral symmetry. The similarities with the models that we use is evident if we compare \mathcal{L}_{QM} with, let's say Eq.(3.2), (3.3) and (3.5).

Finally, it is also possible that one stitches together two phenomenological models into one, specifically a quark model and a nucleon model. The attempt here is to use in each phase a model with the correct degrees of freedom. This fused model might achieve that, but it loses all the information around the chiral phase transition. In such a model it is impossible to calculate the location of the chiral phase transition or the surface tension. They need to be an extra input to the model a free parameter. Another attempt would be to use a single model that contains explicitly both nucleon and quark degrees of freedom, and switches dynamically between one another [47, 48]. The caveat is that one has to be careful when counting the baryons in the system, as nucleons or as quarks.

1.3 Inhomogeneous phases

The consideration of an inhomogeneous phase in dense matter is an effort to make any discussion about the ground state of nuclear matter more realistic. Restricting ourselves to homogeneous phases only, we significantly simplify calculations, but at the same time we strip ourselves from an enormous breadth of alternative plausible scenarios. The purpose of this section is to discuss such scenarios.

1.3.1 Mixed phases

Consider an infinite nucleonic system of constant temperature and uniform baryon density, which is also *locally* charge neutral due to the presence of electrons. Moreover, let the system sit at a critical chemical potential μ_B^* where a first order phase transition takes place. Now, flip half of the system to the phase beyond the phase transition. Since the system is sitting at the critical chemical potential, one may naively expect that there would be a sharp interface separating the two phases. However, such a discontinuity will come at a great energy cost and it would probably be smoothed out, creating an extended domain wall where thermodynamic quantities would smoothly change. The energy surplus from such a configuration, compared to the energy of the whole system containing only 1 phase, is the surface tension Σ between the two phases. But there might be even more complexity in the real case.

By relaxing the local charge neutrality condition to a *global* one, we allow for locally electrically charged phases to exist, while the total charge of the system remains zero. Under this new condition, we may be able to construct a new, preferred phase which combines both phases on the two sides of the phase transition. This *mixed* phase is made up from oppositely charged phases with phase A occupying a volume fraction χ and phase B the remaining $1-\chi$. Such a situation is depicted at Fig. 1.5

The existence of a first order phase transition is crucial, since on that critical chemical potential $\mu_B^{\rm crit}$ both phases are equally preferred (energetically) and have equal pressures. That means they can co-exist. However, it is not given that this co-existence can be extended over a finite range in μ_B . It is necessary that the free energy of each phase at $\mu_B^{\rm crit}$ is lowered by introducing net opposite charges, while the

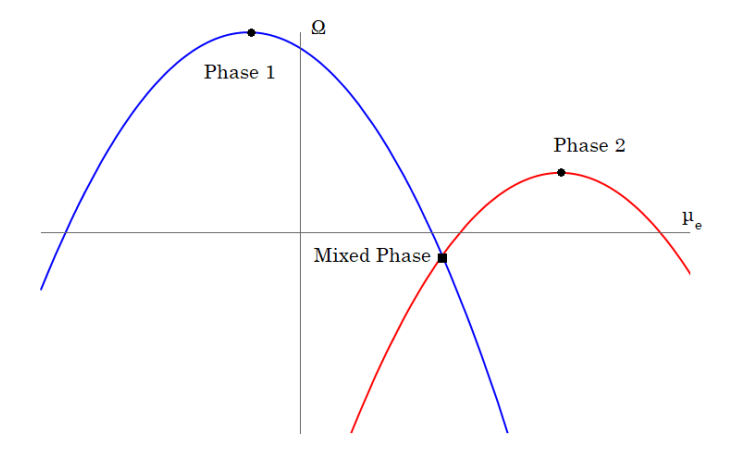


FIGURE 1.5: Schematic representation of a situation where the mixed phase has a lower free energy than the constituent pure phases. It is crucial that at the intersection the slope of the two curves is of opposite sign, signifying the oppositely charged phases. The electron chemical potential μ_e provides a new "dimension" along which the free energy is reduced.

pressure remains equal

$$\Omega_A = \Omega_B. \tag{1.53}$$

Then, we can adjust χ from 0 to 1, keeping the condition (1.53), and smoothly interpolate between the 2 pure phases A and B with out mixed phase.

In order to decipher whether such a construction is preferred, the free energy of the mixed phase needs to be compared with that of the competing pure phase, for each μ_B . However, there are two extra energy contributions that we need to take into account when calculating the free energy of the mixed phase. First, there is the Coulomb interaction between the two oppositely charged phases, that depends on their spatial configuration [49]. Second, whatever that configuration might be, the sharp interfaces are again smoothed out by domain walls, introducing an associated surface tension energy cost. The ground state configuration of the two phases comprising the mixed phase is the shape that minimizes these additional energy contributions. It may resemble different "pasta phases" like gnocchi, spaghetti or lasagna [50].

1.3.2 Inhomogeneous condensates

A different kind of inhomogeneity is possible. Unlike the mixed phases, where an inhomogeneous configuration arises from a construction involving only homogeneous

phases, there is the possibility that the ground state of the system displays some inherent inhomogeneity. We already mentioned a superfluid phase that contains an inhomogeneous diquark condensate. In the context of the chiral phase transition, we would like to know whether the associated order parameter, the chiral condensate, additionally breaks symmetries of the Poincaré group in the ground state.

Such configurations have been extensively studied in quark models [51–63] and less so in nucleon models [64–67], and are expected to appear in the region of the chiral phase transition smoothing a first order discontinuity. However, we show in Chapter 2 that the first order jump is not necessary, and that such a phase can arise and disrupt a smooth crossover.

The phase that we later explore is the Chiral Density Wave (CDW), which is a sinusoidal modulation with wavenumber $|\vec{q}|$ for the scalar $\sigma \propto \langle \bar{\psi}\psi \rangle$ and pseudoscalar $\pi_3 \propto \langle \bar{\psi}\gamma^5\psi \rangle$ components of the chiral condensate

$$\sigma(\vec{x}) = \phi \cos(2\vec{q} \cdot \vec{x}), \quad \pi_3(\vec{x}) = \phi \sin(2\vec{q} \cdot \vec{x}). \tag{1.54}$$

Even though this configuration seems inhomogeneous, all observables of the system turn out to be homogeneous. Hence, such a phase is just anisotropic, by the spontaneous breaking of rotational symmetry that manifests when the system picks some arbitrary direction for the wave-vector \vec{q} .

There are also some truly inhomogeneous candidate phases. Some examples are a simple 1D modulation only in the σ direction [52], the solitonic solution for the mass function M(x) [68]

$$M(x) = \Delta \nu \frac{\operatorname{sn}(\Delta x | \nu) \operatorname{cn}(\Delta x | \nu)}{\operatorname{dn}(\Delta x | \nu)},$$
(1.55)

with sn, cn and dn being the Jacobi elliptic functions, or higher dimensional modulations of the form

$$\sigma(x,y) = \phi \cos(q_x x) \cos(q_y y). \tag{1.56}$$

In any case, for a given system one in principle has to calculate and compare the free energy of every possible configuration to find the true ground state, or result to some sort of stability analysis to prove that they have indeed found the state of least energy. This is not what we will do, as our goal will be different.

1.4 Neutron stars

Neutron stars are born in supernova explosions when the remnant's mass is approximately between $1.4~M_{\odot}$ and $3~M_{\odot}$ [69]. The iron core of the dying star collapses and reaches densities above the nuclear saturation density, where the notion of individual nuclei is lost. After the violent explosion the remnant is very hot, with a temperature significant even for the QCD scale, reaching tens of MeV. However, the neutron star cools very fast via neutrino emission due to the direct URCA process. We can write the direct (modified) URCA process as

$$B(+N) \to B'(+N) + \ell + \bar{\nu}_{\ell}, \quad B(+N) + \ell \to B'(+N) + \nu_{\ell},$$
 (1.57)

where baryon B decays to baryon B' via the absorption (emission) of a lepton ℓ and its (anti-)neutrino. The modified URCA also needs a spectator nucleon N for kinetic reasons. The direct URCA process dominates the neutron star cooling but it is only possible at high densities i.e. in the core of the star, where the proton fraction is large enough. At low densities only the modified URCA contributes, which is slower in comparison. As a result of neutrino emission, the star becomes cold on the QCD scale in a few years [70], reaching a temperature of hundreds of eV. The emission of X-rays from the neutron star surface is another mechanism that contributes to neutron star cooling, but is only dominating at later times.

1.4.1 Composition

The details of the inner structure of a neutron star are unclear. The outer crust is still made from atomic nuclei, mainly iron ions [71], arranged on a lattice, surrounded by an electron gas that ensures the system remains charge neutral. This structure has a density that is much smaller than nuclear saturation density, and in our language can be described by a vacuum-nuclear matter mixed phase. Diving deeper in the crust the lattice spacing decreases, and nuclei start getting richer in neutrons. At some point,

1.4. Neutron stars 27

the excess neutrons start dripping from the nuclei, forming a neutron gas around the neutron rich ion lattice. This is the boundary between the inner and outer crust. Moreover, neutrons start to pair and the neutron gas develops a superfluid component.

In the inner crust the superfluid component is still existent, and is responsible for the observed *pulsar glitches* [72] i.e. the sudden spin-up of the neutron star during its spinning down lifetime. Superfluid vortices form and pin on lattice sites, storing angular momentum. While they form and equilibrate, the spin-down of the whole system breaks this equilibrium which ultimately un-pins a number of vortices and moves them outwards, abruptly transferring their momentum to the crust [73].

Going deeper into the inner crust, the separation between the individual nuclei becomes so small that they start fusing into different pasta phases. This is due to the comparable contribution of the nuclear force and the Coulomb interaction at the small length scales of the system. Again, in our language, this is a "nuclear matter - neutron gas with a superfluid component" mixed phase. At even larger densities the pasta phases "melt" into a uniform medium of neutrons, protons and electrons, which marks the transition to the core.

In the work that I will present we are not including a crust description. The stars that we will construct do not contain a "nuclear matter-vacuum" mixed phase or a superfluid component.

The composition of the core is already taking us to uncharted territory. First principle methods still apply below about 2 n_0 [74] so we expect that the outer core is mostly comprised of neutrons with a small fraction of protons and electrons. At even larger densities muons appear, and even more exotic degrees of freedom are expected to be energetically preferred. The "opening" of a new Fermi sphere (let's say of some hyperon) comes with a smaller energy cost that adding another neutron with a very high Fermi energy. But such an onset is expected to come with a softening of the equation of state, which leads to a prediction of a maximum neutron star mass that is inconsistent with observations. This is the well known "hyperon puzzle". [75]

Finally, there is a possibility that the neutron star core probes densities that are beyond the chiral phase transition, and that quark matter appears. Unfortunately, the

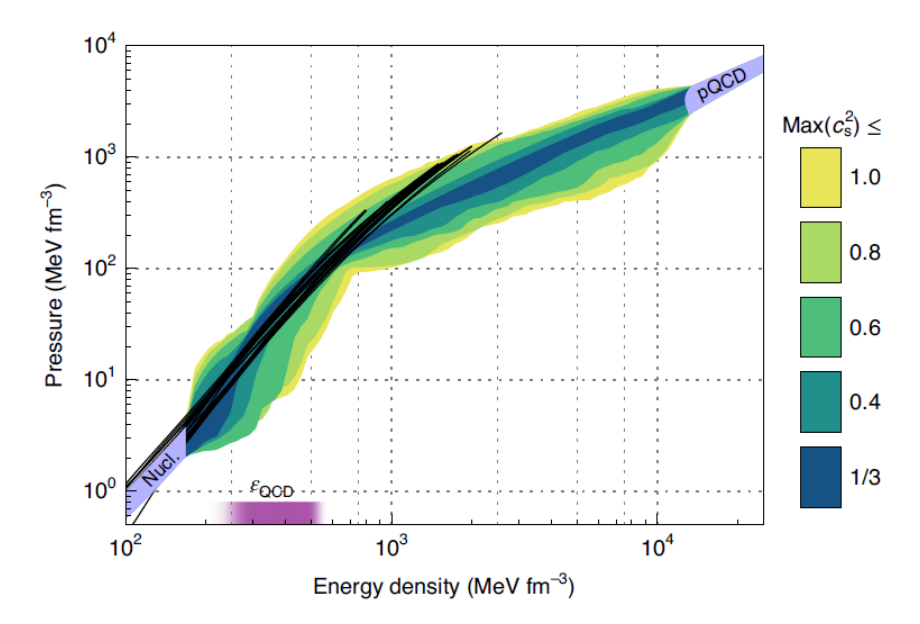


FIGURE 1.6: Possible equations of state consistent with ChEFT and perturbative expansions of QCD (light blue bands at both ends). Different colors correspond to different maximal values of the speed of sound squared. Equations of state are selected by interpolating between the two light blue regions and classified based on their maximal sound speed. Image taken from [77].

density is only expected to be about $8n_0$ [76], which is still in the strong coupling regime of QCD. Even if there is quark matter in the center of the neutron star core, it is strongly coupled and accessible only to phenomenological models. The composition of the core is something we explore with our model in Chapter 2.

1.4.2 Mass and radius

Since neutron stars are the only physical laboratories probing cold and dense matter, we want to know what kinds of information we can extract from them and what to require that our models reproduce. In our work we focus on the equation of state and the resulting mass-radius curve.

We model the neutron star as a zero temperature fluid governed by an equation of state, i.e. a relation between the pressure P and the energy density ϵ of the fluid $P(\epsilon)$. The derivation of this equation depends on the microscopic properties of the system and the model that is used to perform them. There are model agnostic approaches as well [77] that may be quantitatively more precise, but lack the microscopic description of matter. Such an example is given in Fig. 1.6

1.4. Neutron stars 29

In order to build a star out of a given equation of state we need to employ General Relativity. Specifically we want to know what is the spherically symmetric solution of the Einstein equations

$$R_{\mu\nu} - \frac{1}{2} R \, g_{\mu\nu} = T_{\mu\nu},\tag{1.58}$$

where

$$T^{\mu\nu} = (P + \epsilon)u^{\mu}u^{\nu} + Pg^{\mu\nu}, \tag{1.59}$$

is the stress energy tensor of an ideal fluid. In our approach we ignore rotation and only consider static compact stars. The equations boil down to

$$\frac{\partial M(r)}{\partial r} = 4\pi r^2 \epsilon,\tag{1.60}$$

$$\frac{\partial P(r)}{\partial r} = -G \frac{\left[\epsilon(r) + P(r)\right] \left[M(r) + 4\pi P(r)r^3\right]}{r \left[r - 2GM(r)\right]},\tag{1.61}$$

where M(r) is the mass profile of the star and G is the gravitational constant. These are the Tolman-Oppenheimer-Volkoff (TOV) equations. These are 2 equations that contain 3 unknown functions, ϵ , P and M. The equation of state closes the system and makes it possible to determine the mass profile of a star. The equations are solved by picking a central pressure value as boundary condition $P(0) = P_0$ and then integrating until the "surface" of the star at r = R (or more precisely the end of the outer core) where P(R) = 0. This procedure yields the pressure and mass profiles of the star from which we can calculate the total star mass M_{tot} . If we also used some microscopic model to calculate the equation of state, we also derive the profile of all quantities in our model. Finally, by picking different P_0 as initial conditions we are able to draw a curve in the $R-M_{\text{tot}}$ plane, the Mass-Radius curve. Such plots can be seen in Fig. 2.6.

Each mass-radius curve predicts a maximum mass star that has to be consistent with current experimental constraints. The stricter ones today come from the pulsar PSR J0952–0607 with a mass of about $2.35M_{\odot}$ [78, 79]. Any model that fails to produce maximum mass stars of at least as much is incompatible with observations. Moreover, each model in turn predicts that any object with a mass larger than the maximum mass is bound to collapse to a black hole.

There are more observables than the mass and radius that have been discussed here. Recently, due to the development of gravitational wave astronomy, it has been possible to infer the tidal deformability of a neutron star from the gravitational signal emitted during the inspiral phase of a binary compact star system. This measurement has a sensitive dependence on the radius of the star and the elastic properties of the crust. Since in our description we will not include a crust, we do not expect that our model reproduces such predictions accurately. Nevertheless, the goal of the project was not to create a detailed model of the neutron star, but to use the maximum star mass as an extra constraint for the equation of state. Since the contribution of the crust to the total mass would not be significant, including it is not crucial for our purpose.

Chapter 2

Strange Quark Matter from a baryonic approach

2.1 Introduction

The work presented in this chapter has already been published in [1].

In this chapter, we are interested in the chiral phase transition at zero temperature and large, but not asymptotically large, baryon chemical potentials. We shall employ a relatively simple phenomenological model to explore this region of the phase diagram. Even giving up the rigor of the underlying fundamental theory, it is a challenge to account for both quark matter and hadronic matter within a single approach. Using a single model is beneficial if one wants to have a prediction about the critical chemical potential at which the chiral phase transition occurs. While this transition point is a prediction of a unified approach, it is essentially a model parameter if two separate descriptions of hadronic and quark matter are glued together. Another advantage is that the single model enables the calculation of the surface tension (if the transition is of first order), for which the full potential, connecting both local minima, needs to be known.¹. In particular, one needs information on the barrier, which is directly related to the surface tension. The reason for that lies in the fact that, given the effective potential, one can resort to the full

¹Even though there is a well-known systematic procedure to build an effective potential from the matching of pressures obtained from different models, it requires extra information that is usually not available, which results in more free parameters and uncertainties [80–82].

power of semiclassical methods, perturbing the system around classical solutions instead of trivial vacua (see e.g. Refs. [83, 84]). Such classical solutions probe the entire structure of the potential, including the different phases it allows.

The majority of studies of hybrid stars – compact stars with a quark matter core and a nuclear mantle – employ two separate descriptions for the two phases, see for instance Refs. [85–93]. A few unified approaches do exist in the literature. One example is to start from a Lagrangian that contains both baryonic and quark degrees of freedom [47, 48], another is a holographic approach where baryonic and quark phases are realized in a consistent way [94–96]. Here we pursue a very simple idea, already put forward in Refs. [49, 97]: we start from a Lagrangian with only baryonic degrees of freedom, where the masses are entirely generated through the chiral condensate, similar to the extended linear sigma model employed in Refs. [67, 98]. This allows us to observe a chiral phase transition and a (approximately) chirally symmetric phase at high densities with very small baryonic masses. This is in contrast to similar models of the Walecka type [45, 99–102], which can only be used to describe chirally broken matter. Our study extends the model of Refs. [49, 97, 103, 104] to include strangeness via hyperonic degrees of freedom, which gives rise to a more realistic picture of the chirally restored phase, resembling "strange quark matter" in various aspects that will be discussed in detail. In particular for neutron star conditions this is an essential improvement since without strangeness the model does not have any degrees of freedom that carry both baryon number and negative electric charge. This is relevant due to the neutrality constraint and can also be expected to alter the screening effects at the interfaces of mixed phases, and thus our study provides a framework to improve the study of "chiral pasta" [49].

By including hyperons we do not necessarily change the baryonic phase of the model. Whether actual hyperons appear is decided dynamically. They may be disfavored before the chiral phase transition, and we shall see that they indeed only appear for values of the model parameters that are in conflict with astrophysical data of compact stars. However, the hyperonic degrees of freedom do play a role in the chirally restored phase and we shall see that parameter regions allowed by empirical constraints do also allow for strangeness in the chirally restored phase for all chemical potentials above the chiral phase transition. It is in this sense that we speak of strange quark matter from a baryonic approach, having in mind that there are no quark

2.1. Introduction 33

degrees of freedom in our model and that we should not expect to reproduce all known properties of weakly interacting, three-flavor quark matter at asymptotically large densities. Instead, our model provides a prediction for chirally restored matter close to the chiral phase transition, relevant for compact stars, with properties very different from simple extrapolations of weakly-coupled quark matter.

We shall keep most of the approximations used in the non-strange version of the model [49, 97], i.e. our evaluation will be in the mean-field and no-sea approximations at zero temperature, and we shall neglect Cooper pairing that is expected to occur in nuclear matter [105] and quark matter [42]. As in Refs. [49, 97], we should keep in mind that our description of dense matter is based on extrapolating a model constructed mainly to reproduce low-density properties of nuclear matter. We shall restrict ourselves to thermodynamic properties and homogeneous phases, within the constraints of equilibrium with respect to the weak interactions and local electric charge neutrality. The main idea of this work is to set up the model and explore its parameter space in order to identify regions in which it reproduces basic properties of symmetric nuclear matter at saturation, basic properties of strange quark matter at asymptotically large densities and is able to reproduce compact stars with a mass of at least about 2.1 solar masses, meeting the constraint set by the heaviest known compact star [106, 107]. In doing so, we can e.g. constrain to a very narrow range the poorly known slope parameter of the symmetry energy, $L \simeq (88 - 92)$ MeV. Our study thus lays the ground for future studies for instance of the quark-hadron mixed phase or the chiral density wave [61, 67, 108] in the vicinity of the chiral phase transition.

The chapter is organized as follows. We set up the model in Sec. 2.2, including the underlying Lagrangian and the resulting Euler-Lagrange equations. Some guidance and insight for the setup is gained from an SU(3) symmetric approach, which we review in Appendix A. In Sec. 2.3 we discuss carefully the matching procedure of our parameters and identify the freedom in the parameter choices left by experimental uncertainties, mainly in the strangeness sector. Our main results are presented and discussed in Sec. 2.4, which we have divided into a subsection on a few selected parameters sets, Sec. 2.4.1, and a more general survey of the parameter space, Sec. 2.4.2, where we draw some parameter-independent conclusions. We give a summary and an outlook in Sec. 2.5.

2.2 Setup

2.2.1 Lagrangian

The hadronic part of our Lagrangian is composed of baryonic and mesonic contributions and baryon-meson interactions,

$$\mathcal{L} = \mathcal{L}_B + \mathcal{L}_M + \mathcal{L}_I. \tag{2.1}$$

The baryonic part is

$$\mathcal{L}_B = \sum_i \bar{\psi}_i (i\gamma^\mu \partial_\mu + \gamma^0 \mu_i) \psi_i \,, \tag{2.2}$$

where $\bar{\psi}_i = \psi_i^\dagger \gamma^0$ and the sum is over the baryon octet, $i=n,p,\Sigma^0,\Sigma^-,\Sigma^+,\Lambda,\Xi^0,\Xi^-$. We have not included any explicit mass terms, all baryon masses will be generated dynamically by the chiral condensate. Since in QCD chiral symmetry is only approximate, adding small explicit masses does not violate general principles, and this was indeed done in comparable approaches [109]. For simplicity, and to avoid additional parameters, we shall account for explicit chiral symmetry breaking only in the meson potential and the choice of the baryon-meson coupling constants. The Lagrangian formally contains a chemical potential for each of the 8 baryon species, but in (three-flavor) QCD there are only three independent chemical potentials, associated with baryon number, isospin, and strangeness. In terms of these chemical potentials,

$$\mu_i = \mu_B + I_i \mu_I + S_i \mu_S \,, \tag{2.3}$$

where I_i is the third component of the isospin and S_i is the strangeness of the baryons, such that explicitly

$$\mu_{n/p} = \mu_B \pm \mu_I, \qquad (2.4a)$$

$$\mu_{\Sigma^{\pm}} = \mu_B \mp 2\mu_I - \mu_S , \qquad (2.4b)$$

$$\mu_{\Lambda} = \mu_{\Sigma^0} = \mu_B - \mu_S \,, \tag{2.4c}$$

$$\mu_{\Xi^{-}/\Xi^{0}} = \mu_{B} \pm \mu_{I} - 2\mu_{S}$$
 (2.4d)

2.2. Setup 35

The number of independent chemical potentials is further reduced by the conditions of equilibrium with respect to the weak interactions and electric charge neutrality. We require the leptonic process $p+e\to n+\nu_e$ to be in equilibrium with the inverse reaction $n\to p+e+\bar\nu_e$, and the same for the non-leptonic processes $n+n\leftrightarrow p+\Sigma^-$. Other weak reactions involving hyperons exist but their equilibration does not yield independent conditions for our chemical potentials. We shall assume that neutrinos have mean free paths larger than the size of the system, such that we may set the neutrino chemical potential to zero. This is a good assumption for neutron stars unless the temperature is larger than about a few MeV, which is only the case in the very early stages of their evolution and in merger processes. At zero temperature, weak equilibrium directly translates into simple conditions for the chemical potentials, $\mu_p + \mu_e = \mu_n$, and $2\mu_n = \mu_p + \mu_{\Sigma^-}$. As a result, we can express μ_B , μ_I , μ_S in terms of neutron and electron chemical potentials,

$$\mu_B = \mu_n - \frac{\mu_e}{2}, \qquad \mu_I = \frac{\mu_e}{2}, \qquad \mu_S = -\frac{\mu_e}{2}.$$
(2.5)

The mesonic part of the Lagrangian contains the scalar meson σ and the vector mesons ω^{μ} , ρ_0^{μ} , ϕ^{μ} ,

$$\mathcal{L}_{M} = \frac{1}{2} \partial_{\mu} \sigma \partial^{\mu} \sigma - U(\sigma) - \frac{1}{4} \omega_{\mu\nu} \omega^{\mu\nu} - \frac{1}{4} \phi_{\mu\nu} \phi^{\mu\nu} - \frac{1}{4} \rho_{\mu\nu}^{0} \rho_{0}^{\mu\nu} + \frac{m_{\omega}^{2}}{2} \omega_{\mu} \omega^{\mu} + \frac{m_{\phi}^{2}}{2} \phi_{\mu} \phi^{\mu} + \frac{m_{\rho}^{2}}{2} \rho_{\mu}^{0} \rho_{0}^{\mu} + \frac{d}{4} (\omega_{\mu} \omega^{\mu} + \rho_{\mu}^{0} \rho_{0}^{\mu} + \phi_{\mu} \phi^{\mu})^{2}, \qquad (2.6)$$

where $\omega_{\mu\nu}=\partial_{\mu}\omega_{\nu}-\partial_{\nu}\omega_{\mu}$ and analogously for $\phi_{\mu\nu}$ and $\rho_{\mu\nu}^0$. This Lagrangian can be viewed as a subset of the Lagrangian containing the full scalar, pseudoscalar, and vector meson nonets [110], only keeping the fields that we assume to condense in the medium given by the baryons. This is justified by the mean-field approximation, where the fluctuations of the meson fields are neglected. For instance, the pseudoscalar nonet is completely omitted here because we assume none of these fields to condense. It is only indirectly used by fitting one of the parameters of the potential U to the pion mass. Moreover, in the scalar sector, the fields corresponding to the 0 and 8 direction with regard to the commonly used generators of U(3) are usually rotated to give a non-strange scalar field σ and a strange field ζ . This is explained more explicitly in Appendix A, where we briefly review the more systematic approach

using the full mesonic and baryonic multiplets. Here, in the main part, we omit the ζ field (and condensate) for simplicity. This is comparable to the approximation used in Walecka-like models, where the excitations of the scalar fields (not their condensates) are fundamental degrees of freedom of the Lagrangian. In this case, the strangeness sector, i.e., the excitation of the ζ , is sometimes omitted as well for phenomenological reasons [93, 111]. The potential for the remaining scalar meson is chosen to be the same as in the two-flavor version of this model [49, 97, 103, 104],

$$U(\sigma) = \sum_{n=1}^{4} \frac{a_n}{n!} \frac{(\sigma^2 - f_{\pi}^2)^n}{2^n} - \epsilon(\sigma - f_{\pi}), \qquad (2.7)$$

with parameters a_1 , a_2 , a_3 , a_4 , ϵ and the pion decay constant $f_\pi \simeq 92.4\,\mathrm{MeV}$. Temporarily including pion fluctuations, we fit $a_1 = m_\pi^2$ to reproduce the vacuum mass of the pion $m_\pi = 139\,\mathrm{MeV}$, and requiring the vacuum value of the chiral condensate to be $\langle \sigma \rangle = f_\pi$, we obtain $\epsilon = m_\pi^2 f_\pi$. For the vector meson masses in Eq. (2.6) we will use $m_\omega = 782\,\mathrm{MeV}$, $m_\phi = 1020\,\mathrm{MeV}$, $m_\rho = 775\,\mathrm{MeV}$. We have included a quartic meson coupling term [48, 112–114] with coupling constant $d \ge 0$, which will play an important role for our results. The structure of this term is a particular choice within the more general quartic term based on a chiral approach, see appendix A and in particular Eq. (A.7).

The baryon-meson interactions are given by

$$\mathcal{L}_{I} = -\sum_{i} \bar{\psi}_{i} (g_{i\sigma}\sigma + g_{i\omega}\gamma^{\mu}\omega_{\mu} + g_{i\rho}\gamma^{\mu}\rho_{\mu}^{0} + g_{i\phi}\gamma^{\mu}\phi_{\mu})\psi_{i}. \qquad (2.8)$$

As dictated by the chiral SU(3) approach, the coupling constants within each isospin multiplet are related, see appendix A, and will be denoted by

$$g_{Nx} \equiv g_{nx} = g_{px}$$
, $g_{\Sigma x} \equiv g_{\Sigma^0 x} = g_{\Sigma^{\pm} x}$, $g_{\Xi x} \equiv g_{\Xi^0 x} = g_{\Xi^{-} x}$, (2.9)

for $x = \sigma, \omega, \phi$, and

$$g_{N\rho} \equiv g_{n\rho} = -g_{p\rho}$$
, $g_{\Sigma\rho} \equiv g_{\Sigma^+\rho} = -g_{\Sigma^-\rho}$, $g_{\Xi\rho} \equiv g_{\Xi^0\rho} = -g_{\Xi^-\rho}$, (2.10)

while $g_{\Sigma^0\rho}=g_{\Lambda\rho}=0$. The coupling constants $g_{i\sigma}$ between the baryons and the scalar field are fixed by their vacuum masses. At mean-field level, and using that in the

2.2. Setup 37

vacuum $\langle \sigma \rangle = f_{\pi}$, the baryonic vacuum masses are $m_i = g_{i\sigma}f_{\pi}$. Using $m_N \equiv m_{n/p} \simeq 939\,\mathrm{MeV}$, $m_{\Delta} \simeq 1115\,\mathrm{MeV}$, $m_{\Sigma^{\pm}/\Sigma^0} \simeq 1190\,\mathrm{MeV}$, $m_{\Xi^{-}/\Xi^0} \simeq 1315\,\mathrm{MeV}$, this fixes the coupling constants $g_{i\sigma}$. Fixing the couplings between the baryons and the vector mesons is more complicated. It is possible to derive the coupling terms from a SU(3) invariant approach, see appendix A. We shall use the resulting constraints for some of the hyperonic couplings, combined with a phenomenological approach for the nucleonic couplings, as we shall explain in Sec. 2.3.

2.2.2 Free energy and stationarity equations

We allow the scalar meson field and the temporal components of the vector meson fields to condense and denote the corresponding condensates by

$$\sigma \equiv \langle \sigma \rangle, \quad \omega \equiv \langle \omega_0 \rangle, \quad \rho \equiv \langle \rho_0^0 \rangle, \quad \phi \equiv \langle \phi_0 \rangle.$$
 (2.11)

They are assumed to be homogeneous in space, and we neglect all mesonic fluctuations. This allows us to write down an effective "mean-field Lagrangian",

$$\mathcal{L} = \sum_{i} \bar{\psi}_{i} (i\gamma^{\mu} \partial_{\mu} + \gamma^{0} \mu_{i}^{*} - M_{i}) \psi_{i} - U(\sigma) - V(\omega, \rho, \phi), \qquad (2.12)$$

with the vector meson potential

$$V(\omega,\rho,\phi) = -\frac{1}{2}(m_{\omega}^2\omega^2 + m_{\rho}^2\rho^2 + m_{\phi}^2\phi^2) - \frac{d}{4}(\omega^2 + \rho^2 + \phi^2)^2, \qquad (2.13)$$

the effective chemical potentials

$$\mu_{n/p}^* = \mu_{n/p} - g_{N\omega}\omega - g_{N\phi}\phi \mp g_{N\rho}\rho, \qquad (2.14a)$$

$$\mu_{\Sigma^0}^* = \mu_{\Sigma^0} - g_{\Sigma\omega}\omega - g_{\Sigma\phi}\phi, \qquad (2.14b)$$

$$\mu_{\Sigma^{\pm}}^{*} = \mu_{\Sigma^{\pm}} - g_{\Sigma\omega}\omega - g_{\Sigma\phi}\phi \mp g_{\Sigma\rho}\rho, \qquad (2.14c)$$

$$\mu_{\Lambda}^{*} = \mu_{\Lambda} - g_{\Lambda\omega}\omega - g_{\Lambda\phi}\phi$$
, (2.14d)

$$\mu_{\Xi^{0}/\Xi^{-}}^{*} = \mu_{\Xi^{0}/\Xi^{-}} - g_{\Xi\omega}\omega - g_{\Xi\phi}\phi \mp g_{\Xi\rho}\rho,$$
 (2.14e)

and the effective, medium-dependent masses

$$M_{n/p} = g_{N\sigma}\sigma$$
, $M_{\Sigma^0/\Sigma^{\pm}} = g_{\Sigma\sigma}\sigma$, $M_{\Lambda} = g_{\Lambda\sigma}\sigma$, $M_{\Xi^0/\Xi^{-}} = g_{\Xi\sigma}\sigma$. (2.15)

As often done in comparable phenomenological models, we shall omit the (renormalized) vacuum contribution ("no-sea approximation"). The idea is that this contribution would only yield a quantitative change and since the entire approach is of phenomenological nature there is not much to be gained from the inclusion of this contribution, given that the parameters of the model will be fitted within this approximation to low-energy nuclear matter properties. (There are cases, however, where the vacuum part makes a *qualitative* difference, for instance in the case of a background magnetic field [98, 115–117].) We shall also restrict ourselves to zero temperature. Then, the free energy density becomes

$$\Omega = -\sum_{i} p(\mu_{i}^{*}, M_{i}) + U(\sigma) + V(\omega, \rho, \phi) - p(\mu_{e}, m_{e}) - p(\mu_{\mu}, m_{\mu}), \qquad (2.16)$$

where the pressure of each fermion species is given by the function

$$p(\mu, M) = \frac{\Theta(\mu - m)}{8\pi^2} \left[\left(\frac{2}{3} k_F^3 - m^2 k_F \right) \mu + m^4 \ln \frac{k_F + \mu}{m} \right], \qquad (2.17)$$

with the Fermi momentum

$$k_F = \sqrt{\mu^2 - m^2} \,. \tag{2.18}$$

In Eq. (2.16) we have added the leptonic contribution, with electron and muon chemical potentials μ_e , μ_μ , and their masses $m_e=0.511\,\mathrm{MeV}$ and $m_\mu=106\,\mathrm{MeV}$. Weak equilibrium requires $\mu_e=\mu_\mu$, for instance through the processes $e\to\mu+\bar\nu_\mu+\nu_e$ and $\mu\to e+\bar\nu_e+\nu_\mu$. We define the following general expressions for the scalar density and the fermionic number density,

$$n_{\rm sc}(\mu,m) \equiv -\frac{\partial p}{\partial m} = \Theta(\mu - m) \frac{m}{2\pi^2} \left(k_F \mu - m^2 \ln \frac{k_F + \mu}{m} \right),$$
 (2.19a)

$$n(\mu, m) \equiv \frac{\partial p}{\partial u} = \Theta(\mu - m) \frac{k_F^3}{3\pi^2}.$$
 (2.19b)

2.2. Setup 39

Then, the Euler-Lagrange equations can be written as

$$0 = \frac{\partial \Omega}{\partial \sigma} = \frac{\partial U}{\partial \sigma} + \sum_{i} g_{i\sigma} n_{\text{sc},i}, \qquad (2.20a)$$

$$0 = \frac{\partial \Omega}{\partial \omega} = \frac{\partial V}{\partial \omega} + \sum_{i} g_{i\omega} n_{i}, \qquad (2.20b)$$

$$0 = \frac{\partial \Omega}{\partial \rho} = \frac{\partial V}{\partial \rho} + \sum_{i} g_{i\rho} n_{i}, \qquad (2.20c)$$

$$0 = \frac{\partial \Omega}{\partial \phi} = \frac{\partial V}{\partial \phi} + \sum_{i} g_{i\phi} n_{i}, \qquad (2.20d)$$

where $n_{sc,i} \equiv n_{sc}(\mu_i^*, M_i)$ and $n_i \equiv n(\mu_i^*, M_i)$. Additionally, we need the constraint from local electric charge neutrality, which reads

$$0 = \frac{\partial \Omega}{\partial \mu_e} = -n_p - n_{\Sigma^+} + n_{\Sigma^-} + n_{\Xi^-} + n_e + n_{\mu}. \tag{2.21}$$

For the equation of state we shall need the energy density

$$\epsilon = -P + \mu_e n_e + \mu_u n_u + \mu_B n_B + \mu_S n_S + \mu_I n_I = -P + \mu_n n_B,$$
 (2.22)

where $P = -\Omega$ is the pressure, where, in the second step, we have used the chemical potentials (2.5) and the charge neutrality condition (2.21), and where baryon, strangeness, and isospin number densities are

$$n_B = \sum_i n_i, \qquad n_S = \sum_i S_i n_i, \qquad n_I = \sum_i I_i n_i.$$
 (2.23)

2.2.3 Speed of sound

We require that our model reproduces the speed of sound of asymptotically dense cold QCD, such that our chirally restored phase shares this property with realistic quark matter. At asymptotically large densities the speed of sound squared c_s^2 of QCD goes to the conformal limit 1/3, since in this limit μ_B is much larger than the QCD scale and, due to asymptotic freedom, also much larger than the constituent quark masses. Therefore, the baryon density is that of a free gas of fermions, $n_B \propto \mu_B^3$, which yields $c_s^2 = 1/3$, independent of the proportionality constant, as can be easily checked

from the definition

$$c_s^2 = \frac{\partial P}{\partial \epsilon} = \frac{n_B}{\mu_B} \left(\frac{dn_B}{d\mu_B} \right)^{-1} . \tag{2.24}$$

Here, the first expression is valid in general, i.e., also for nonzero temperatures, in which case the derivative with respect to ϵ is taken at fixed entropy per particle. The second expression is valid at zero temperature; see for instance appendix E of Ref. [94] for a derivation of the general expression in terms of derivatives with respect to the chemical potential and temperature.

To discuss the speed of sound in our model, let us for illustrative purposes in this section only consider isospin-symmetric nuclear matter without strangeness, i.e. we ignore hyperons for now and the only nonzero meson condensates are σ and ω . Also ignoring neutrality and a possible lepton contribution, the only relevant equations are Eqs. (2.20a) and (2.20b), which have to be solved for σ and ω and which we write as

$$0 = f_1(\sigma, \omega, \mu_B) \equiv \frac{\partial U}{\partial \sigma} + 2g_{N\sigma} n_{\rm sc}(\mu_B^*, M), \qquad (2.25a)$$

$$0 = f_2(\sigma, \omega, \mu_B) \equiv \omega(m_\omega^2 + d\omega^2) - g_{N\omega}n_B, \qquad (2.25b)$$

with $M = g_{N\sigma}\sigma$, $\mu_B^* = \mu_B - g_{N\omega}\omega$. For the speed of sound we need the derivative

$$\frac{dn_B}{du_B} = \frac{\partial n_B}{\partial u_B} + \frac{\partial n_B}{\partial \sigma} \frac{\partial \sigma}{\partial u_B} + \frac{\partial n_B}{\partial \omega} \frac{\partial \omega}{\partial u_B}.$$
 (2.26)

The explicit derivatives of n_B are easily obtained, but σ and ω are only given implicitly by Eqs. (2.25) (there is no analytical solution even in this simplified scenario). We can, however, compute the relevant derivatives in terms of σ and ω via

$$\left(\frac{\partial \sigma}{\partial \mu_{B}}, \frac{\partial \omega}{\partial \mu_{B}}\right) = -\left(\frac{\partial f_{1}}{\partial \mu_{B}}, \frac{\partial f_{2}}{\partial \mu_{B}}\right) \left(\begin{array}{cc} \frac{\partial f_{1}}{\partial \sigma} & \frac{\partial f_{2}}{\partial \sigma} \\ \frac{\partial f_{1}}{\partial \omega} & \frac{\partial f_{2}}{\partial \omega} \end{array}\right)^{-1}.$$
(2.27)

Inserting all this into the definition of the speed of sound yields after some algebra

$$c_{s}^{2} = \frac{1}{3} \frac{k_{F}^{2}}{\mu_{B} \mu_{B}^{*}} \left[\frac{\frac{2k_{F} \mu_{B}^{*}}{\pi^{2}} + \frac{3}{M} \frac{\partial U}{\partial M} - \frac{\partial^{2} U}{\partial M^{2}}}{\frac{2k_{F}^{2}}{\pi^{2} \mu_{B}^{*}} + \frac{3}{M} \frac{\partial U}{\partial M} - \frac{\partial^{2} U}{\partial M^{2}} + \frac{2g_{N\omega}^{2} k_{F} \mu_{B}^{*}}{\pi^{2} (m_{\omega}^{2} + 3d\omega^{2})} \right],$$
 (2.28)

2.2. Setup 41

where $k_F^2 = (\mu_B^*)^2 - M^2$. This relatively compact expression is valid for all densities, but still requires solving equations (2.25) numerically for an explicit evaluation. In this section we are only interested in the asymptotic limit, which can be evaluated analytically. One observes that taking the limit $\mu_B \to \infty$ does not commute with the limit $d \to 0$. If we first send $d \to 0$, the solutions of Eq. (2.25) become for large μ_B

$$d = 0: \qquad \sigma \simeq \left(\frac{2g_{N\omega}^2 \pi}{3m_{\omega}^2}\right)^{2/3} \frac{f_{\pi} m_{\pi}^2}{g_{N\sigma}^2 \mu_B^{2/3}}, \qquad \omega \simeq \frac{\mu_B}{g_{N\omega}} - \left(\frac{3\pi^2 m_{\omega}^2 \mu_B}{2g_{N\omega}^5}\right)^{1/3}. \quad (2.29)$$

The subleading term in ω is needed to obtain the leading behavior for μ_B^* . Since for $\mu_B \to \infty$ we have $k_F \simeq \mu_B^*$, the first term in the square brackets in Eq. (2.28) approaches 1. It is therefore subleading and the asymptotic speed of sound is given by the second term in the square brackets. With the relations (2.29) we find $c_s^2 = 1$. Therefore, if the quartic self-interactions are switched off in the Lagrangian, d = 0, the speed of sound approaches the speed of light at asymptotically large μ_B .

On the other hand, if we first take the limit $\mu_B \to \infty$ at nonzero d we find for the leading terms of the solution of Eqs. (2.25)

$$\sigma \simeq \left[1 + \left(\frac{2g_{N\omega}^4}{3\pi^2 d} \right)^{1/3} \right]^2 \frac{f_{\pi} m_{\pi}^2 \pi^2}{g_{N\sigma} \mu_B^2}, \qquad \omega \simeq \left[1 + \left(\frac{3\pi^2 d}{2g_{N\omega}^4} \right)^{1/3} \right]^{-1} \frac{\mu_B}{g_{N\omega}}. \tag{2.30}$$

Again, the first term in the square brackets in Eq. (2.28) becomes 1, but this time it is of the same order as the second term, and both terms together give the asymptotic result $c_s^2 = 1/3$ for all d > 0, a conclusion also reached for a similar model in Ref. [118]. This shows that only in the presence of a quartic vector meson self-coupling our model reproduces the asymptotic speed of sound of QCD.

These observations also suggest that by choosing a sufficiently small but nonzero d, the speed of sound becomes arbitrarily close to 1 at intermediate densities. The reason is that the behavior of the condensates (2.29) also holds in a regime where μ_B is large compared to all other energy scales while the dimensionless parameter $d\mu_B^2/m_\omega^2$ is small, see Eqs. (2.25b) and (2.28). For any nonzero d, of course, the behavior (2.30) eventually takes over as μ_B is increased and the speed of sound approaches 1/3 asymptotically. This can be confirmed numerically, as well as the fact that these asymptotic limits derived here remain valid in the more complicated scenario including strangeness and the neutrality constraint.

2.3 Parameter choices

Our strategy for fixing the parameters of the Lagrangian is to fit as many as possible to empirical vacuum and low-density quantities, and explore the parameter space of the remaining ones to understand the qualitative behavior of the model, in particular with respect to the chiral phase transition and the onset of strangeness. We have already used vacuum properties to fix ϵ , a_1 , m_{ω} , m_{ϕ} , m_{ρ} , $g_{N\sigma}$, $g_{\Lambda\sigma}$, $g_{\Sigma\sigma}$, $g_{\Xi\sigma}$. We assume that the nucleons do not couple to the hidden strangeness meson, $g_{N\phi}=0$ [109, 119, 120]. It remains to choose values for, first, a_2 , a_3 , a_4 , d, $g_{N\omega}$, $g_{N\rho}$, and, second, the couplings of the hyperons to the vector mesons $g_{\Lambda\omega}$, $g_{\Sigma\omega}$, $g_{\Xi\omega}$, $g_{\Lambda\phi}$, $g_{\Sigma\phi}$, $g_{\Xi\phi}$, $g_{\Sigma\rho}$, $g_{\Xi\rho}$. Let us discuss these two groups of parameters separately.

2.3.1 Saturation properties

We relate the 6 parameters a_2 , a_3 , a_4 , d, $g_{N\omega}$, $g_{N\rho}$ to 6 properties of isospin-symmetric nuclear matter at saturation: we use the well-known binding energy $E_B = -16.3 \,\mathrm{MeV}$ and saturation density $n_0 = 0.153 \, \text{fm}^{-3}$, and also work with a definite symmetry energy $S = 32 \,\text{MeV}$, following the empirical estimates $S \simeq (30.2 - 33.7) \,\text{MeV}$ [121, 122] (see, however, Ref. [33], which predicts a somewhat larger value based on measurements of the neutron skin thickness by the PREX collaboration [123]). The incompressibility at saturation is less well known, $K \simeq (200 - 300)$ MeV. In our main results we shall employ the value $K = 250 \,\mathrm{MeV}$. We have checked that our results do not change much under variations of *K* in the empirically allowed range. There is much more sensitivity to the effective nucleon mass at saturation, M_0 , and the slope Lof the symmetry energy with respect to density changes away from saturation. For later, we shall keep in mind an empirical range of $M_0 \simeq (0.7 - 0.8) m_N$ [124–129]. Estimates for the slope of the symmetry energy range from $L \simeq (40-60) \,\mathrm{MeV}$ [130–132] to more recent values using the result of the PREX experiment [123], indicating that larger values might be favored, $L \simeq (70-140)$ MeV [33]; for a recent overview of the various estimates for *L* see Ref. [133].

To set up the relation between the model parameters and the saturation properties, we denote the chemical potential at the onset of isospin-symmetric (non-strange) baryonic matter by $\mu_0 = 922.7 \,\text{MeV}$, and the effective baryon chemical

potential by $\mu_0^* = \mu_n^* = \mu_p^* = \sqrt{k_F^2 + M_0^2}$, where the Fermi momentum can be expressed in terms of the saturation density via $n_0 = 2k_F^3/(3\pi^2)$, which yields $k_F \simeq 260$ MeV. In the absence of hyperons, baryon and isospin densities are $n_B = n_n + n_p$ and $n_I = n_n - n_p$, respectively. In symmetric nuclear matter, where $n_I = 0$, the stationarity equations (2.20) give $\rho = \phi = 0$, while ω obeys the cubic equation

$$g_{N\omega}n_0 = m_\omega^2 \omega + d\omega^3, \qquad (2.31)$$

whose relevant solution we write as

$$\omega_0 = \frac{g_{N\omega} n_0}{m_\omega^2} f(x_0) , \qquad (2.32)$$

with

$$f(x) \equiv \frac{3}{2x} \frac{1 - (\sqrt{1 + x^2} - x)^{2/3}}{(\sqrt{1 + x^2} - x)^{1/3}}, \qquad x_0 \equiv \frac{3\sqrt{3d} g_{N\omega} n_0}{2m_{\omega}^3}.$$
 (2.33)

With $\lim_{x\to 0} f(x) = 1$ we recover the case without quartic vector meson interactions, d = 0. We also need the definitions of incompressibility, symmetry energy, and slope of the symmetry energy,

$$K = 9n_B \frac{\partial \mu_B}{\partial n_B}, \qquad S = \frac{n_B}{2} \frac{\partial \mu_I}{\partial n_I}, \qquad L = 3n_B \frac{\partial S}{\partial n_B},$$
 (2.34)

where K is evaluated for symmetric nuclear matter, the derivative in S is taken at fixed n_B and evaluated at $n_I = 0$, and the derivative in L is taken at fixed $n_I = 0$.

Putting all of this together, we obtain the following six conditions for the model parameters:

$$g_{N\omega}^2 = \frac{m_{\omega}^2}{2n_0} (\mu_0 - \mu_0^*) \left[1 + \sqrt{1 + \frac{4dn_0(\mu_0 - \mu_0^*)}{m_{\omega}^4}} \right] , \qquad (2.35a)$$

$$g_{N\rho}^2 = \frac{3\pi^2 m_{\rho}^2}{k_F^3} \left(S - \frac{k_F^2}{6\mu_0^*} \right) \left(1 + \frac{d\omega_0^2}{m_{\rho}^2} \right) , \qquad (2.35b)$$

$$L = \frac{3g_{N\rho}^{2}n_{0}}{2(m_{\rho}^{2} + d\omega_{0}^{2})} \left[1 - \frac{2d n_{0}g_{N\omega}\omega_{0}}{(m_{\rho}^{2} + d\omega_{0}^{2})(m_{\omega}^{2} + 3d\omega_{0}^{2})} \right] + \frac{k_{F}^{2}}{3\mu_{0}^{*}} \left(1 - \frac{K}{6\mu_{0}^{*}} \right) + \frac{g_{N\omega}^{2}n_{0}k_{F}^{2}}{2m_{\omega}^{2}\mu_{0}^{*2}} [f(x_{0}) + x_{0}f'(x_{0})],$$

$$(2.35c)$$

$$K = \frac{3k_F^2}{\mu_0^*} - \frac{6k_F^3}{\pi^2} \left(\frac{M_0}{\mu_0^*}\right)^2 \left[\frac{1}{g_{N\sigma}^2} \frac{\partial^2 U}{\partial \sigma^2} + \frac{2}{\pi^2} \int_0^{k_F} \frac{dk \, k^4}{(k^2 + M_0^2)^{3/2}}\right]^{-1} + \frac{6k_F^3}{\pi^2} \frac{g_{N\omega}^2}{m_{\sigma}^2} [f(x_0) + x_0 f'(x_0)], \qquad (2.35d)$$

$$0 = \frac{m_{\omega}^2}{2}\omega_0^2 + \frac{d}{4}\omega_0^4 - U(\sigma) + \frac{1}{4\pi^2} \left[\left(\frac{2}{3}k_F^3 - M_0^2 k_F \right) \mu_0^* + M_0^4 \ln \frac{k_F + \mu_0^*}{M_0} \right], \quad (2.35e)$$

$$0 = \frac{\partial U}{\partial \sigma} + \frac{g_{N\sigma} M_0}{\pi^2} \left(k_F \mu_0^* - M_0^2 \ln \frac{k_F + \mu_0^*}{M_0} \right). \tag{2.35f}$$

Here, the first relation is obtained from inserting the relation $\mu_0^* = \mu_0 - g_{N\omega}\omega_0$, which follows from Eq. (2.14a), into Eq. (2.31); the next relations are obtained by computing S, L, and K from their definitions (2.34); finally, we have the condition that the pressure at saturation be identical to the pressure of the vacuum, which in our convention is zero, and the stationarity equation (2.20a) for σ , whose value is $\sigma = M_0/g_{N\sigma}$ at saturation.

For given L, S, K, M_0 , μ_0 , n_0 , Eqs. (2.35) can now be solved to obtain the model parameters a_2 , a_3 , a_4 , $g_{N\omega}$, $g_{N\rho}$, d. For the practical calculation it is useful to note that (2.35a), (2.35b), (2.35c) do not depend on a_2 , a_3 , a_4 (which only enter through the meson potential U), such that they can be solved separately for $g_{N\omega}$, $g_{N\rho}$, d. The results are then used to solve Eqs. (2.35d), (2.35e), (2.35f) for a_2 , a_3 , a_4 . If the quartic coupling is set to zero, d=0, Eqs. (2.35a) and (2.35b) can be used to obtain $g_{N\omega}$ and $g_{N\rho}$, and the coupled equations (2.35d), (2.35e), (2.35f), are used to fix a_2 , a_3 , a_4 , while L can only be computed afterwards, i.e., in this case there is no freedom in the parameter set to reproduce a given value for L.

Interestingly, Eqs. (2.35) can be used to compute a window in the M_0 -L plane for a given value for K. From Eqs. (2.35a) and (2.35b) we see that in order for $g_{N\omega}^2$ and $g_{N\rho}^2$ to be positive we need

$$k_F \sqrt{\left(\frac{k_F}{6S}\right)^2 - 1} < M_0 < \sqrt{\mu_0^2 - k_F^2}.$$
 (2.36)

We can also compute the limits of *L* for d = 0 and $d \to \infty$, which gives the range

$$S + \frac{k_F^2(3\mu_0 - K)}{18\mu_0^{*2}} < L < \frac{3g_{N\rho}^2 n_0}{2m_\rho^2} + \frac{k_F^2}{3\mu_0^*} \left(1 - \frac{K}{6\mu_0^*}\right) + \frac{g_{N\omega}^2 n_0 k_F^2}{2m_\omega^2 \mu_0^{*2}}, \tag{2.37}$$

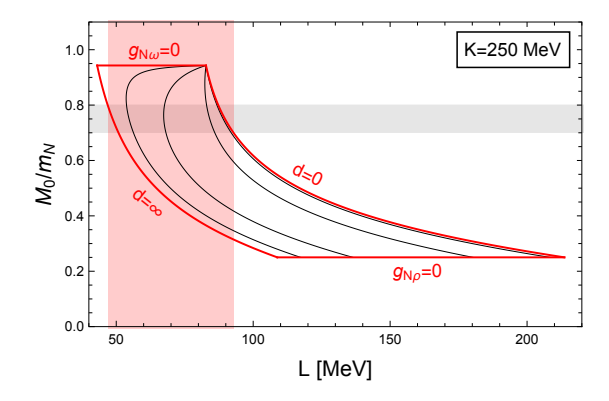


FIGURE 2.1: Allowed window (red curves) of the model in the M_0 -L plane bounded by the limits (2.36) and (2.37), solely derived from known saturation properties of symmetric nuclear matter. Here we have set K = 250 MeV, which we will use throughout this chapter. The thin black curves are lines of constant d, d = 10, 10^2 , 10^3 , 10^4 from right to left. The grey horizontal band indicates the empirically favored range for M_0 , which results in a predicted range $L \simeq (47-93)$ MeV, shown by the red vertical band.

where the lower (upper) limit comes from $d \to \infty$ (d=0). We have considered the possibility of negative d, but have not found any physically sensible solutions, in most cases indicated by a superluminal speed of sound combined with the solutions of the stationarity equations turning complex at large densities, see also Refs. [118, 134]. The resulting window in the M_0 -L plane is shown in Fig. 2.1 for $K=250\,\mathrm{MeV}$ (with all other saturation properties as given above). If we apply the realistic window $M_0\simeq (0.7-0.8)m_N$ we see that this already constrains the range for the slope of the symmetry energy to $L\simeq (47-93)\,\mathrm{MeV}$, as indicated by the shaded bands in the figure.

2.3.2 Couplings between hyperons and vector mesons

The choice for the hyperon couplings $g_{\Lambda\omega}$, $g_{\Sigma\omega}$, $g_{\Xi\omega}$, $g_{\Delta\phi}$, $g_{\Sigma\phi}$, $g_{\Xi\phi}$, $g_{\Sigma\rho}$, $g_{\Xi\rho}$ is much less constrained by experimental data. Here our strategy is to combine phenomenological constraints with the relations given by the chiral approach of appendix A, while leaving one degree of freedom to be varied to probe the dependence of our results on different choices of the hyperon couplings. The connection between the coupling constants and (potential) experimental data is made by the hyperon potential depths. The potential depth $U_i^{(j)}$ of a single hyperon i in a medium of baryon species j at arbitrary baryon density n_B is computed as follows. We assume isospin-symmetric media, such that $n_p = n_n$ for j = N, $n_{\Sigma^+} = n_{\Sigma^0} = n_{\Sigma^-}$ for $j = \Sigma$, and $n_{\Xi^0} = n_{\Xi^-}$ for

 $j = \Xi$. As a consequence, $\rho = 0$ in each case, and the Fermi momentum k_F is related to the baryon density by

 $n_B = \frac{sk_F^3}{3\pi^2},$ (2.38)

where s is a degeneracy factor, s=2,1,3,2 for baryonic media N,Λ,Σ,Ξ , respectively. The single-baryon energy $E_{k,i}^{(j)}$ of baryon i in a medium of baryon j obeys the relation

$$E_{k,i}^{(j)} - \mu_i = \sqrt{k^2 + (M_i^{(j)})^2} - \mu_i^{*(j)},$$
 (2.39)

where $M_i^{(j)}$ is the medium-dependent mass of baryon i and $\mu_i^{*(j)}$ is its effective chemical potential, containing the actual chemical potential μ_i and the medium-dependent condensates, see Eq. (2.14). The potential is given by the minimum of the single-baryon energy $E_{k=0,i}^{(j)}$ minus the vacuum mass m_i ,

$$U_i^{(j)} = M_i^{(j)} - \mu_i^{*(j)} + \mu_i - m_i = g_{i\sigma}(\sigma^{(j)} - f_{\pi}) + g_{i\omega}\omega^{(j)} + g_{i\phi}\phi^{(j)}, \qquad (2.40)$$

where, in the second step, we have expressed the vacuum mass in terms of the vacuum value of the chiral condensate, $m_i = g_{i\sigma}f_{\pi}$. The medium-dependent mass and effective chemical potential have been written in terms of the meson condensates in the medium of baryon j, which have to be computed numerically with the help of the stationarity equations at the given baryon density n_B (2.38). For our purposes, Eq. (2.40) is only needed for the hyperon potentials in a medium of nucleons at saturation density. In this case $\phi = 0$, and using $g_{N\sigma}\sigma^{(N)} = M_0$, $g_{N\sigma}f_{\pi} = m_N$ we can write

$$U_i^{(N)} = \frac{g_{i\sigma}}{g_{N\sigma}}(M_0 - m_N) + g_{i\omega}\omega_0, \qquad (2.41)$$

where $\omega^{(N)} = \omega_0$ is the value of the condensate at saturation (2.32). We thus have three relations, $i = \Sigma, \Lambda, \Xi$, to relate three hyperon potentials to the hyperon-omega coupling constants.

In all our results we shall use the value

$$U_{\Lambda}^{(N)} = -30 \,\text{MeV}\,,$$
 (2.42)

as suggested by experimental data [135, 136] and adopted in comparable models [111, 137, 138]. The potentials for Σ and Ξ are less well known experimentally, with

2.4. Results 47

chiral effective theory suggesting $U_{\Xi}^{(N)}$ to have a relatively small absolute value with either sign possible and $U_{\Sigma}^{(N)}$ more likely to be positive [139, 140]. For simplicity, we shall assume the values of both potentials to be identical,

$$\mathcal{U} \equiv U_{\Sigma}^{(N)} = U_{\Xi}^{(N)}, \qquad (2.43)$$

and vary $\mathcal U$ within a reasonable range. We shall see that within this simplistic approach we will have to choose in particular $U^{(N)}_\Sigma$ to be different from what is usually adopted. Due to the large uncertainties in our knowledge of these potentials this may not seem too unreasonable. Moreover, empirical constraints drive our choice to more attractive potentials compared to the most common values in the literature, such that one might expect hyperons to be unusually favored in our results. However, we shall see that for the parameter sets that meet astrophysical constraints strangeness does not occur in the chirally broken phase. Therefore, even if the hyperon potentials we choose are different from their value in nature, we do not have hyperons with unphysical properties in our system. The hyperon coupling constants then rather characterize the interactions in the chirally restored phase (i.e., of "strange quark matter"), for which no direct experimental information is available and where astrophysical data are our best source for constraints, forcing us to somewhat stretch the usual regime for the hyperon potentials.

After choosing a value of \mathcal{U} , Eqs. (2.41), (2.42), (2.43) fix the ω coupling constants $g_{\Sigma\omega}$, $g_{\Lambda\omega}$, $g_{\Xi\omega}$. This leaves the coupling constants $g_{\Lambda\phi}$, $g_{\Sigma\phi}$, $g_{\Xi\phi}$, $g_{\Sigma\rho}$, $g_{\Xi\rho}$, which we compute from the chiral relations (A.12) (ignoring the relations in that equation for $g_{\Sigma\omega}$, $g_{\Lambda\omega}$, $g_{\Xi\omega}$).

2.4 Results

We present and discuss our results as follows. First, in Sec. 2.4.1 we choose four parameter sets in order to demonstrate qualitatively different scenarios with respect to the chiral phase transition and the onset of strangeness that our model can produce. At this point, we do not yet discard parameter regions disfavored by astrophysical data. The reason is that it is instructive to see that different scenarios can be realized in principle, keeping in mind that our model is of phenomenological nature. Therefore, a

8Νω	gNρ	8Λω	$g_{\Sigma\omega}$	$g_{\Xi\omega}$	a_2	$a_3[\mathrm{MeV}^{-2}]$	$a_4 [\mathrm{MeV}^{-4}]$	M_0/m_N	L[MeV]	Figs. 2.2 – 2.6
10.23	4.138	14.53	14.59	16.39	44.69	$2.917 \cdot 10^{-4}$	$5.071 \cdot 10^{-5}$	0.72	89.91	black
8.196	4.297	12.35	12.03	13.63	55.15	$-7.465 \cdot 10^{-3}$	$9.553 \cdot 10^{-5}$	0.8	86.24	red
6.610	4.379	10.86	10.17	11.65	73.15	$3.120 \cdot 10^{-2}$	$2.865 \cdot 10^{-4}$	0.85	84.66	blue
3.291	4.477	9.371	7.155	8.738	465.5	3.643	$1.305 \cdot 10^{-2}$	0.92	83.14	green

TABLE 2.1: Parameter sets used in Sec. 2.4.1, Figs. 2.2 – 2.6. We have included the resulting values for the Dirac mass at saturation M_0 and the slope parameter L, while $K=250\,\mathrm{MeV}$ in all four cases. The parameters ϵ , a_1 , m_ω , m_ϕ , m_ρ , $g_{N\sigma}$, $g_{\Lambda\sigma}$, $g_{\Sigma\sigma}$, $g_{\Xi\sigma}$ are the same in all cases and fixed by vacuum properties as explained in Sec. 2.2. Moreover, in all four cases d=21, and the hyperon couplings listed here are chosen to give $\mathcal{U}=-50\,\mathrm{MeV}$. The remaining hyperon-meson couplings $g_{\Lambda\phi}$, $g_{\Sigma\phi}$, $g_{\Xi\phi}$, $g_{\Sigma\rho}$, $g_{\Xi\rho}$ are determined by the chiral relations (A.12) in each case separately.

scenario realized in the present version of the model that appears to be excluded by data may be allowed in an improved version of the model, or in a different phenomenological model – or in QCD. Then, second, in Sec. 2.4.2, we *do* discuss the empirical and astrophysical constraints systematically, which will lead to conclusions independent of the particular parameter choices.

2.4.1 Selected parameter sets

We start with the four parameter sets specified in Table 2.1. They all give a potential $\mathcal{U}=-50\,\mathrm{MeV}$ for the Σ and Ξ , and the quartic meson self-coupling constant is fixed to d=21. As mentioned above, we also keep the incompressibility at saturation fixed to $K=250\,\mathrm{MeV}$. The parameter sets are then obtained by varying the Dirac mass at saturation from low (approximately the lower end of the empirically allowed range) to high (somewhat larger than the empirically allowed maximum). The slope parameter L then adjusts accordingly (varying, however, only by a few percent for the given choices). Note that a_4 turns out to be positive in all four cases as it should be since this ensures a bounded vacuum potential for σ .

2.4.1.1 Chiral transition and onset of strangeness

In Fig. 2.2 we show the effective nucleon mass $M_N \equiv M_{n/p}$ as a function of the neutron chemical potential, obtained by solving the stationarity equations (2.20) together with the neutrality constraint (2.21) numerically for σ , ω , ϕ , ρ , μ_e at given μ_n (and T=0). Since all baryon masses are proportional to the chiral condensate σ (multiplied by a coupling constant to reproduce the vacuum masses), the effective hyperon masses

2.4. Results 49

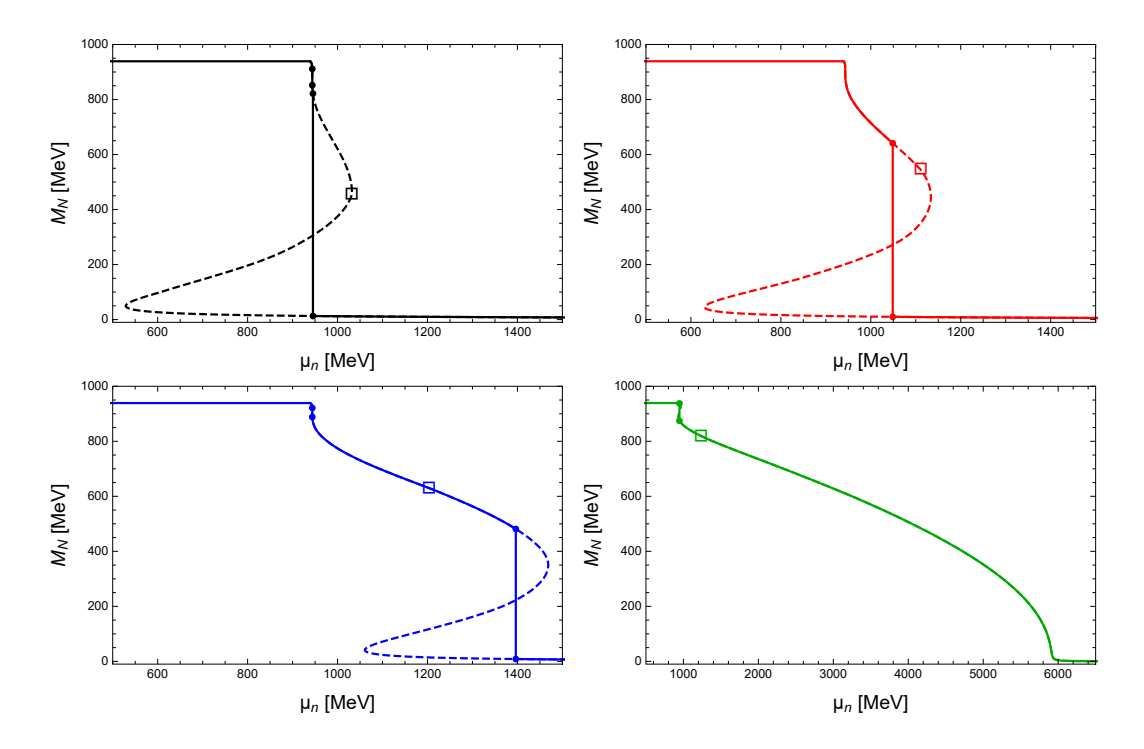


FIGURE 2.2: Effective nucleon mass as a function of the neutron chemical potential for the four parameter sets given in Table 2.1. Solid lines correspond to stable phases, while the dashed segments are metastable (M_N decreasing with μ_n) or unstable (M_N increasing with μ_n). The open squares mark the onset of strangeness, and the dots mark the phase transition within the baryonic phase (upper left and both lower panels) and the chiral phase transition (both upper panels and lower left). In the bottom right panel the chiral transition has become a (steep) crossover.

follow the same behavior. The figure shows all branches of the solution, including the unstable and metastable ones. In all cases, there is an approximately chirally symmetric phase at large chemical potentials, where the baryon masses are very small. In three of the four cases shown here, the chirally restored phase is reached via a first-order phase transition. The location of the phase transition has to be determined from the free energy, i.e., by inserting the solutions of the stationarity equations back into the free energy density (2.16). An example is shown in Fig. 2.3, corresponding to the lower left panel in Fig. 2.2. Determining the state with the lowest free energy at each μ_n allows us to identify the stable branches, shown as solid curves in Fig. 2.2.

Besides the very prominent chiral phase transition, Fig. 2.3 also shows a much weaker first-order phase transition at relatively low densities within the chirally broken phase. This phase transition can be understood as a "remnant" of the first-order onset of isospin-symmetric nuclear matter. In that case, the free energy is multi-valued at the onset, and moving towards more neutron-rich matter tends to

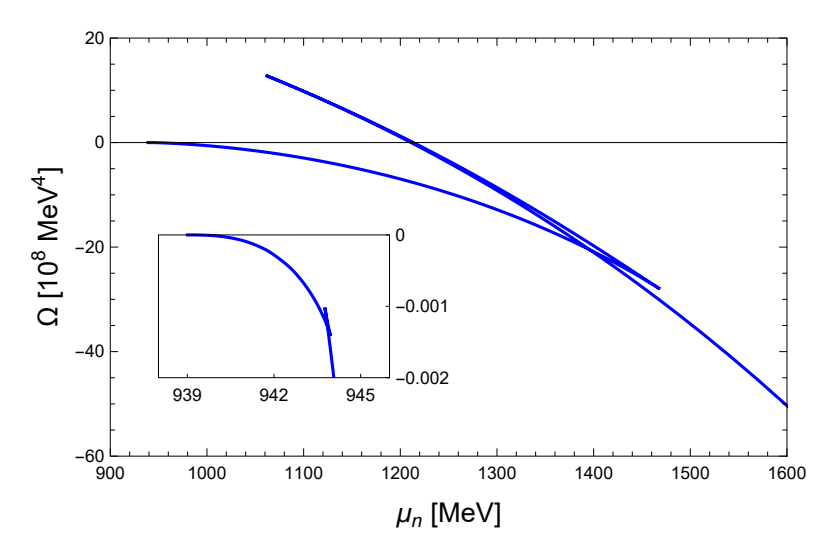


FIGURE 2.3: Free energy density as a function of the neutron chemical potential for the third case (blue) of Fig. 2.2. The large three-valued region is the spinodal region of the first-order chiral phase transition, while the zoom-in shows a (weak) first-order transition within the chirally broken phase.

diminish this multivaluedness, i.e., decrease the spinodal region. This happens gradually, and thus, even in the neutron-rich environment obtained here by the conditions of weak equilibrium and charge neutrality, it is possible that the spinodal region survives. This is the case in three of the four cases in Fig. 2.2, as indicated by the dots that mark the effective nucleon mass on either side of the transition. In contrast to the chiral transition, the curves of stable and unstable phases in the vicinity of this transition are not distinguishable by naked eye on the given scale.

Fig. 2.2 also indicates the onset of strangeness (open squares). We see that there are qualitatively different cases with respect to that onset (and demonstrating these differences is one main motivation for our choice of parameter sets): in the two upper panels, the onset of strangeness occurs in the metastable or unstable regime. This implies that the baryonic phase does not contain any hyperons, while strangeness appears immediately after the chiral transition, i.e. the transition is from nuclear matter to "strange quark matter". Showing the possibility of this scenario within a model based on baryonic degrees of freedom has been one of the main goals of this work (and we shall see below that astrophysical constraints favor this case). The precise location of the strangeness onset within the metastable/unstable regime is irrelevant for the stable, homogeneous phases discussed here. However, it would be interesting for future studies to see how this location affects the properties of

2.4. Results 51

inhomogeneous phases, such as a mixed phase, which does know about the behavior of the model away from the stable branches. In the lower left panel of Fig. 2.2, strangeness occurs already in the baryonic phase. Therefore, in this case the sequence of phases is nuclear matter \rightarrow hyperonic matter \rightarrow chirally restored matter with strangeness. Finally, the lower right panel shows yet another qualitatively different behavior, namely a chiral crossover. In this case, strangeness occurs deeply in the baryonic regime (judging from the effective nucleon mass, which is about 800 MeV at that point). Then, there is a continuous transition to the phase with light degrees of freedom. It is striking that, first, this transition is still relatively "sharp". It is difficult to distinguish it by naked eye from a weak first-order transition. And, second, this sharp transition occurs at extremely large chemical potentials, much larger than in the interior of neutron stars. We have not found any parameter set with reasonable low-density properties that shows a significantly smoother crossover or a significantly smaller transition density. (Judging from the results of the non-strange, isospin-symmetric version of our model [97], a much larger incompressibility, far beyond the physical range, is needed for such a scenario.) Nevertheless, it is interesting that our model allows for the possibility of a crossover, which is conceivable within QCD and corresponding model equations of state have been constructed [141, 142], although this question becomes more subtle in the presence of Cooper pairing [26, 143–145].

While the onset of strangeness marked in Fig. 2.2 refers to the first strange degree of freedom, Fig. 2.4 shows all individual particle fractions as functions of density. We have distinguished non-strange baryons from hyperons and leptons by the color of the curves to facilitate the interpretation. Since the horizontal axis represents density, there are disallowed regions due to the first-order phase transitions. There are metastable and unstable branches in these regions which we have omitted since they are not very instructive. Also, the disallowed regions can be populated by inhomogeneous mixed phases, which we are ignoring in this chapter. We see that the lower critical density of the chiral phase transition varies greatly between the different parameter sets, occurring as early as $n_B \simeq 0.4\,n_0$ in the upper left panel. We have also marked the maximal central densities reached in compact stars for each case by an arrow. These densities lie somewhere in the range $n_B \sim (7-10)\,n_0$, a somewhat large number compared to most comparable phenomenological models.

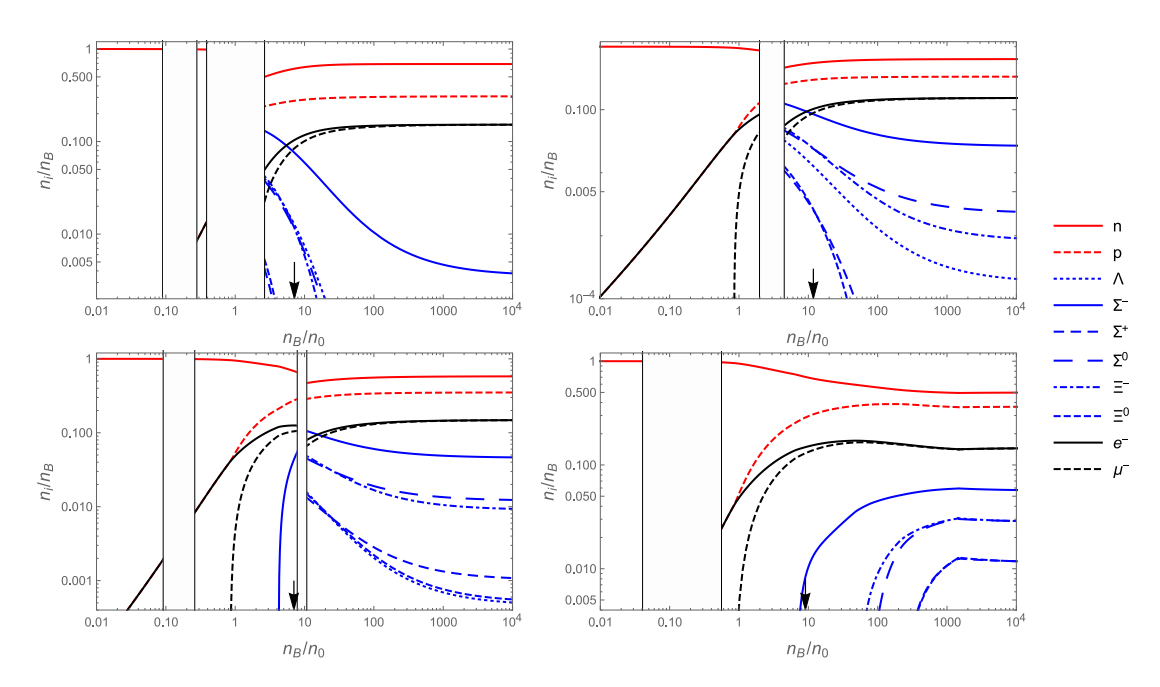


FIGURE 2.4: Density fractions as a function of baryon density (normalized to the saturation density of symmetric nuclear matter n_0) for the four cases of Fig. 2.2, showing non-strange baryons (red), strange baryons (blue) and leptons (black). First-order transitions appear in the form of a gap in the horizontal direction since the density is discontinuous. Cusps arise from the onset of baryonic species. The arrow on the horizontal axis marks the central density of the most massive star possible for each parameter set.

The figure also shows that the most prevalent strange degree of freedom in all four cases is the Σ^- , which is the lightest non-leptonic degree of freedom with negative electric charge. We also see that in the cases with a first-order chiral phase transition the density fractions of the strange degrees of freedom decrease as the density is increased. This is perhaps somewhat unexpected, at least having in mind the following simple picture of quark matter: At intermediate densities we expect the constituent mass of the strange quark to be larger than that of the up and down quarks. At ultra-high densities, due to asymptotic freedom, the quark masses approach the current mass limit, whose scale becomes negligible compared to the chemical potential. As a consequence, one might expect the strangeness content to increase as one moves to higher densities, although the strong-coupling nature of the problem at intermediate densities does not allow a firm first-principles prediction for this behavior. What is firmly predicted by QCD, however, is that three-flavor quark matter becomes flavor symmetric at asymptotically large densities. Our results in Fig. 2.4 show two interesting properties of asymptotically dense matter. First, a nonzero amount of strangeness survives asymptotically. The parameter sets are chosen

2.4. *Results* 53

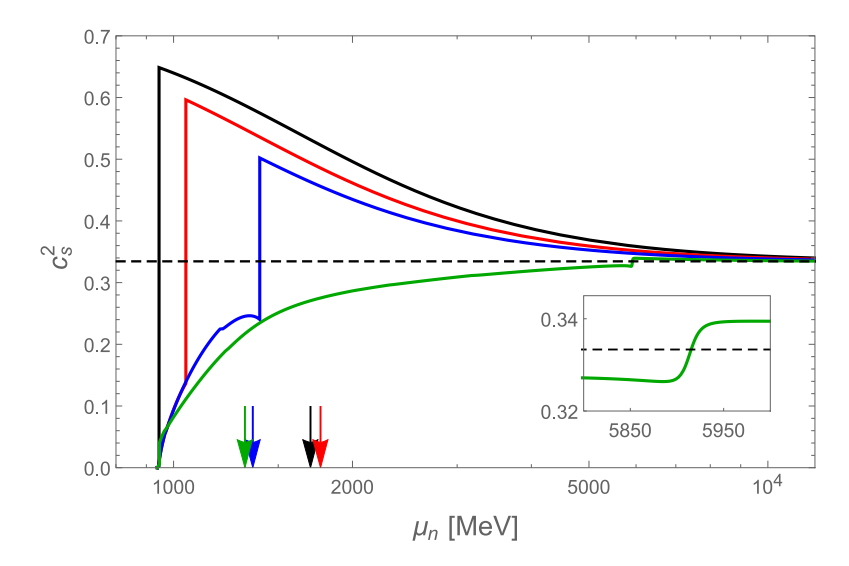


FIGURE 2.5: Speed of sound squared as a function of the neutron chemical potential for the four cases of Fig. 2.2, showing only the stable branches. Colors correspond to the colors of Fig. 2.2, i.e. the Dirac mass at saturation increases from black to red to blue to green. The large discontinuities in the black, red, and blue curves indicate the chiral phase transition, while the green curve has a chiral crossover, as the zoom-in proves. The arrows mark the chemical potentials in the center of the most massive star of each case, and the horizontal dashed line marks the conformal value, $c_{\rm s}^2=1/3$, that is attained asymptotically by all curves.

deliberately to ensure this property, and we shall discuss in the subsequent section that this is not the case for all parameter choices. Second, our asymptotic matter is clearly not flavor symmetric, i.e., the up, down, and strange content of our baryonic degrees of freedom is not equal. We show in Appendix B that there *are* choices of the hyperon-meson coupling constants that lead to asymptotic flavor symmetry (while keeping the saturation properties of symmetric nuclear matter fixed). This would be desirable in our context since this would make our chirally restored matter even more similar to actual QCD quark matter. However, we have not found parameter sets that at the same time produce sufficiently heavy neutron stars, and thus here, in the main part, we do not work with the parameter constraints derived in Appendix B.

2.4.1.2 Speed of sound and mass-radius curves

We show the speed of sound squared c_s^2 for the four parameter sets of the previous subsection in Fig. 2.5. This figure contains various interesting aspects. First, we see that all curves approach the conformal limit $c_s^2 = 1/3$, as already suggested by the analytical calculation in Sec. 2.2.3. While that calculation was performed for

symmetric nuclear matter without strangeness, here we see that the conformal limit is also assumed asymptotically in the electrically neutral, beta-equilibrated case including strange matter. As pointed out in Sec. 2.2.3, the nonzero value of the vector meson self-coupling d is crucial for this behavior. Second, the zoom-in shows that the lower right panels of Figs. 2.2 and 2.4 indeed contain a smooth chiral crossover: the speed of sound – containing a second derivative of the free energy – is continuous and smooth.

Third, and perhaps most importantly, let us comment on the behavior of the speed of sound in the intermediate density regime, relevant for neutron star matter. It is striking that in the cases of a first-order chiral transition the speed of sound increases through the discontinuity as we move towards large densities. Even in the case of the crossover this tendency is retained; through the sharp crossover the speed of sound is increased from just below to just above the conformal limit. (We have checked that there are parameter sets where $c_s^2 > 1/3$ before the sharp crossover, i.e., this is not a generic feature). The large speed of sound in our chirally restored phase is somewhat surprising if we have in mind perturbative QCD, which predicts $c_s^2 < 1/3$ where it is applicable. We should emphasize that our model is not asymptotically free. Even though the conformal limit is approached asymptotically, interactions still play a role in this limit. Therefore, we cannot expect to reproduce this prediction of perturbative QCD. At intermediate densities, QCD is strongly coupled and we have no first-principle results for the speed of sound of quark matter. Therefore, our result is not in any contradiction with QCD. Another reason to expect a smaller speed of sound in the chirally restored phase might be the increase in degrees of freedom as we cross the phase transition. While this tends to soften the equation of state, i.e., to decrease the speed of sound, there are at least two opposing effects that, in our model, turn out to dominate the behavior. Namely, the near-masslessness of the degrees of freedom in the chirally restored phase should indeed contribute to an increase of the speed of sound, and, of course, the form of the interactions plays an important role, which is not easy to disentangle from the other effects. A speed of sound of quark matter above the conformal limit has also been observed in resummed perturbation theory [146] and in the color-flavor locked phase [147]. In fact, it has been shown that no exotic degrees of freedom are necessary in order to generate a speed of sound that surpasses its asymptotic conformal limit. Rather, a peak in the speed of sound of homogeneous

2.4. Results 55

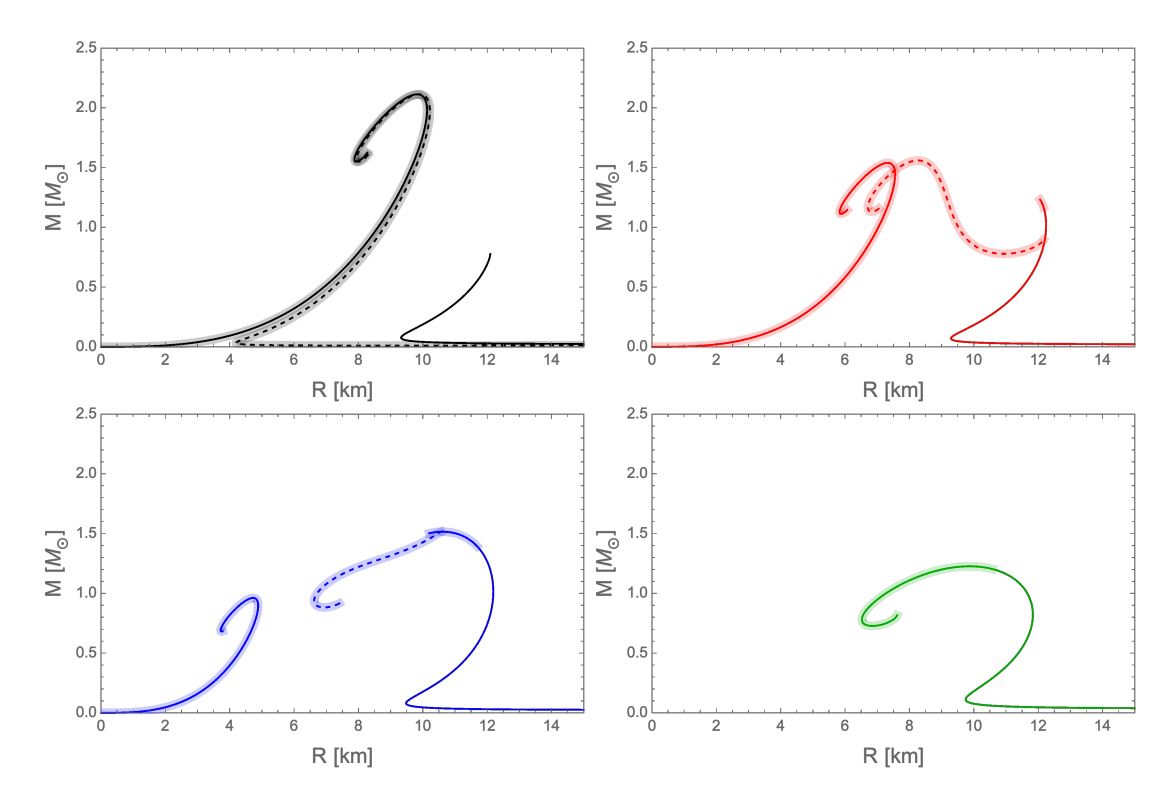


FIGURE 2.6: Mass-radius curves of quark stars (curves reaching back to the origin), hybrid stars (dashed), and neutron stars for the four cases of Fig. 2.2. The shaded bands mark the stars containing strangeness. Only the upper left panel is in accordance with the heaviest known neutron star. (Radius constraints must be ignored here since we have not included a crust, which would change radii, but not the maximal masses, significantly.) The lower right panel corresponds to a parameter set with a chiral crossover and thus only has a single class of stars.

matter naturally emerges in the transition from a phase with broken chiral symmetry to one with a gapped Fermi surface [148].

The speed of sound is a measure for the stiffness of matter, and we expect stiff matter to give rise to large neutron star masses. This connection is borne out in the mass-radius curves shown in Fig. 2.6. They are computed by inserting the equation of state $P(\epsilon)$, with pressure $P=-\Omega$ and energy density ϵ from Eqs. (2.16) and (2.22), into the so-called Tolman-Oppenheimer-Volkoff equations [149–151], which describe a static, spherically symmetric matter configuration in general relativity. By choosing the central pressure as a boundary condition and solving the differential equations numerically one obtains the mass and radius of the star. Varying the central pressure generates a mass-radius curve, representing all possible stars for a given equation of state.

In Fig. 2.6 we show three different classes of stars, which are best explained with

the help of the free energy in Fig. 2.3: "neutron stars", i.e., stars made entirely of baryonic matter, probe the chirally broken branch of our solution. Their maximal central pressure is given by the phase transition point ($\mu_n \simeq 1.4\,\mathrm{GeV}$ in Fig. 2.3) if only stable baryonic matter is considered. In the mass-radius plots we have traced the neutron star branch beyond the transition point into the spinodal region, following the (now metastable) chirally broken solution. Importantly, this spinodal region ends at some point, which corresponds to the end points of the neutron star curves in Fig. 2.6. In an approach using different models for quark and hadronic matter the metastable branch would continue to arbitrarily large densities and no prediction for the endpoint in the mass-radius curve can be made. This metastable neutron star segment can be of astrophysical relevance since it is made of two-flavor nuclear matter (entirely in the upper left panel and for a large part in the upper right panel). Therefore, it is conceivable that it survives for non-microscopic times since the conversion to strange quark matter would require the injection of strangelets.

If we follow the thermodynamically stable branches through the phase transition, we branch off of the neutron star curve by following the chirally restored branch. We obtain hybrid stars, shown by the dashed curves in Fig. 2.6, i.e., stars with a chirally broken mantle and a chirally restored core. This gives rise to the possibility of "twin stars", stable stars with the same mass but different radii [152]. Twins both having thermodynamically stable matter – one neutron star, one hybrid star – are (barely) realized in the upper right panel. However, our results also suggest the existence of twins where one star is made of metastable hadronic matter and its hybrid twin containing a strange quark matter core (upper panels). In all mass-radius plots we have included segments that are expected to be unstable with respect to radial oscillations of the star [127, 153]. Therefore, for instance, the lower left panel does not allow for twin stars because the entire hybrid branch is expected to be unstable.

We also show the mass-radius curves of "quark stars" made entirely out of chirally restored matter in our model. To this end, we follow the chirally restored solution in Fig. 2.3 backwards until the pressure (and thus the free energy density) is zero. In the three cases considered here where this construction is possible, this includes a metastable segment of the solution, towards low densities, similar to the metastable neutron stars just discussed, where the metastable matter sits at high densities. There are parameter regions where the metastable segment does not reach

2.4. Results 57

back to zero pressure, which results in quark matter only appearing in hybrid stars, and not also in a separate branch of quark stars. There are also parameter regions where the chirally restored branch is stable all the way down to zero pressure, which we can interpret as a realization of the strange quark matter hypothesis [154, 155]. We shall come back to this possibility – and identify the region in the parameter space where it is realized – in the subsequent section.

In the calculation of the mass-radius curves we have not included any mixed phase at the chiral phase transition. A mixed phase layer in the star would smoothen the cusp-like transition from the neutron star branch to the hybrid star branch, but otherwise is not expected to change the results significantly. Moreover, we have not included a crust but rather used the homogeneous phases of our model down to the lowest densities. This simplification has a large effect on the radii of the stars. A crust would generate a much larger layer of matter with an average density below saturation density and can be expected to correct the radii to much larger values (see for instance Ref. [156]), with the exception of the quark stars, where only a small crust is expected (see for instance Ref. [157]). Importantly, however, the inclusion of a crust and its precise properties are not expected to change the maximal mass of the given dense matter equation of state [156]. Therefore, the radii in Fig. 2.6 should not be taken too seriously, and we should thus not attempt to compare these results to the latest data for neutron star radii, and neither to constraints for the tidal deformability, which is strongly influenced by the radius of the star. However, the maximal mass of our mass-radius curves can be taken seriously. As a consequence, we see that only the upper left panel corresponds to an equation of state allowed by the existence of a 2.1-solar mass star [106, 107]. In particular, the scenario with the chiral crossover (lower right panel) gives rise to very low masses and thus is in contradiction with astrophysical data. These observations reflect the behavior of the speed of sound in Fig. 2.5: heavy stars are possible for large speeds of sound, and the largest mass is obtained for the case with the earliest chiral phase transition such that the stiff chirally restored phase constitutes a large volume fraction of the heaviest stars. This is in line with recent discussions suggesting the necessity for a non-monotonic behavior of the speed of sound in order to meet astrophysical constraints [77, 158, 159]. While in many approaches, either purely baryonic or in connection with a separate quark matter model, the maximum of the speed of sound is reached in the baryonic phase it

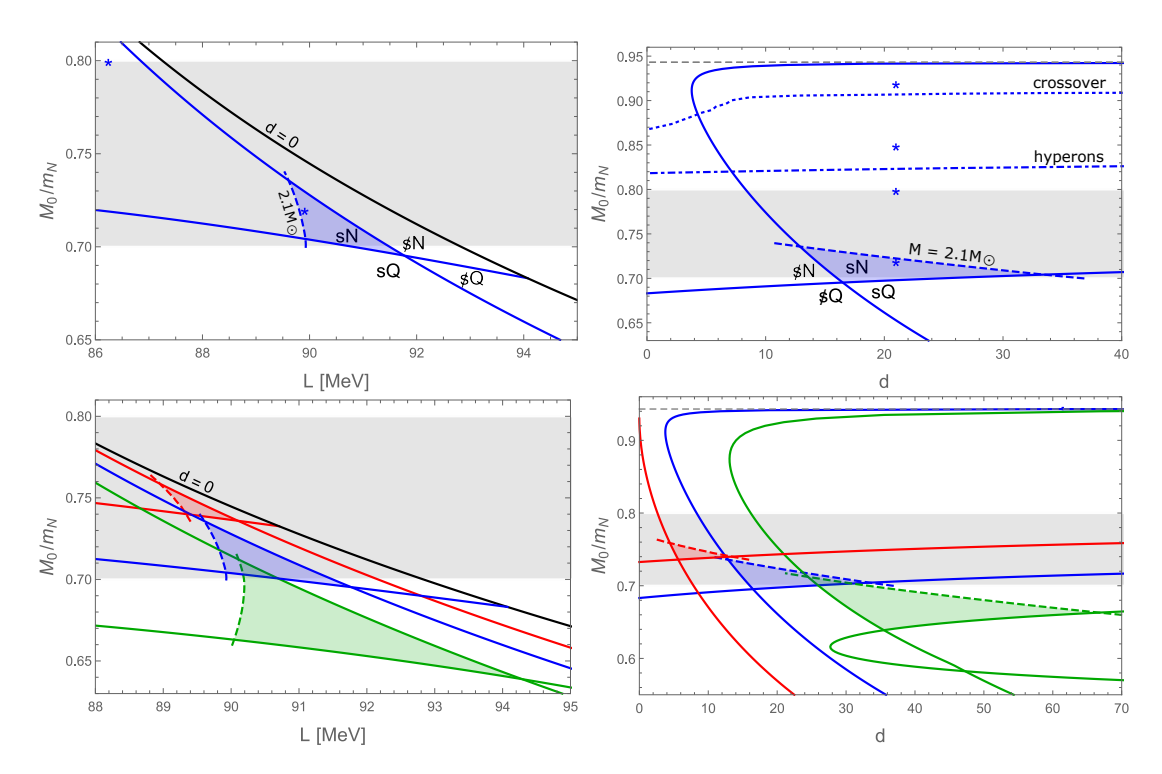


FIGURE 2.7: *Upper panels*: Distinct regions in the M_0 -L and M_0 -d planes for $K=250\,\mathrm{MeV}$ and $\mathcal{U}=-50\,\mathrm{MeV}$. "s" ("\$") labels regions with (without) strangeness at asymptotic densities, "N" ("Q") labels regions where nuclear matter (quark matter) is preferred at zero pressure. In the shaded triangular region maximal masses of (hybrid) stars of more than 2.1 solar masses are reached, in addition to having asymptotic strangeness and nuclear matter being stable at zero pressure. In the right panel, the dashed-dotted (almost horizontal) curve divides the region where hyperons appear before the chiral transition (towards large M_0) from the region where strangeness only appears in the chirally restored phase (towards small M_0). Above the dotted line the chiral transition is a crossover. The grey shaded band in both panels is the empirically preferred regime for M_0 , and the thin horizontal dashed line in the right panel marks the upper limit of M_0 according to Fig. 2.1. The asterisks correspond to the parameter choices in Figs. 2.2 – 2.6 (in the left panel only two of them lie in the shown range). Lower panels: Blue lines as in the upper panels, now with added curves for $\mathcal{U}=-30\,\mathrm{MeV}$ (green) and $\mathcal{U}=-70\,\mathrm{MeV}$ (red).

has also been argued that this behavior may be generated by the so-called quarkyonic phase [160]. In contrast, our results suggest that the peak of the speed of sound may well appear in the quark matter phase, while the baryonic phase exhibits sound speeds below the conformal limit.

2.4.2 Parameter-independent conclusions

We have seen that our model allows for qualitatively different scenarios regarding the chiral phase transition, with different thermodynamic properties and different properties of compact stars. We now intend to determine the region in parameter

2.4. Results 59

space where our model is useful and realistic. For simplicity we keep the incompressibility at saturation fixed to $K = 250 \,\text{MeV}$, and vary the Dirac mass at saturation M_0 , the slope parameter L, and the hyperon potential \mathcal{U} . We present our results in the M_0 -L plane, making the connection to Fig. 2.1. It is useful to consider also the M_0 -d plane for an alternative representation. For a given pair (M_0, d) one can always compute the more physical pair (M_0, L) .

Our results are shown in Fig. 2.7. Let us first focus on the upper panels, which are obtained with the choice $U=-50\,\text{MeV}$, to explain and interpret the various curves.

- *Asymptotic strangeness*. For our main goal to describe strange quark matter with our chirally restored phase we need to check in which cases there is strangeness at asymptotically large densities. (As we have seen in Fig. 2.4, if strangeness survives asymptotically, it tends to be present right after the phase transition as well.) The line in the parameter space that separates the region with asymptotic strangeness from the one without can be calculated with the help of an expansion similar to the asymptotic expansion employed in Appendix B. The ansatz for the solution of the stationarity equations used in this appendix led to conditions for the coupling constants, guaranteeing flavor-symmetric asymptotic strangeness. The weaker condition of the existence of asymptotic strangeness is found by the ansatz $\rho \simeq \rho_{\infty} \mu_n$, $\mu_e \simeq \mu_{e,\infty} \mu_n$ and all other condensates as in Eq. (B.2). This ansatz leads to a set of stationarity equations for the coefficients of the leading-order terms ω_{∞} , ρ_{∞} , ϕ_{∞} , $\mu_{e,\infty}$, which can easily be solved numerically. Then, for instance at a fixed d, we can determine the value of M_0 at which a strange degree of freedom first sets in asymptotically, and repeating the procedure for many values of d gives a curve in the M_0 -d plane and thus also in the M_0 -L plane, shown as a blue solid curve, where regions with and without asymptotic strangeness are labeled by "s" and "\$".
- Stability of nuclear matter at zero pressure. If our chirally restored phase is favored at zero pressure, it prevails for all nonzero densities and the main purpose of the model, to develop a unified approach in the vicinity of the quark-hadron transition, is not realized. Therefore we need to identify the parameter region in which nuclear matter is the favored phase at zero pressure. We can compute the line that bounds this region by computing the points in the M_0 -d plane at which

chirally restored, zero-pressure matter sits exactly at $\mu_n = m_N$, where the second-order onset of charge neutral, beta-equilibrated nuclear matter occurs. If it sits at larger μ_n , as in Fig. 2.3 and all parameter sets of Sec. 2.4.1, there is a chiral transition and we denote this case in Fig. 2.7 by "N"; if it sits at lower μ_n there is no chiral transition and we denote this case by "Q" since it suggests that quark matter is absolutely stable. Together with the criterion for asymptotic strangeness we find four regions: sN, sQ, \sharp N, \sharp Q. (The M_0 -L plane additionally has the region of negative d, which we do not consider.) For our purpose, the sN region – asymptotic strangeness and absolutely stable nuclear matter – is the most relevant.

- Realistic neutron stars. On the blue dashed curve the maximal mass of a hybrid star is exactly $2.1\,M_\odot$, heavier stars are sitting to the right (upper left panel) or below (upper right panel) this curve. We have restricted this curve to the sN region and only indicated that it also extends into the the sQ region (where there are no hybrid stars, i.e. the maximal mass is reached by a quark star) and into the \$N\$ region. The resulting window in the sN region containing stars with maximal masses compatible with astrophysical data is shaded in blue. One of the four parameter sets of Sec. 2.4.1, indicated by asterisks, lies in that region. We see that the shaded region is compatible with the empirical constraints for M_0 , and that it defines a remarkably narrow range in L. As a measure for the largest possible mass of the star inside the triangular region we have also computed the mass at the tip of the triangle opposite of the dashed curve and found $M \simeq 2.28\,M_\odot$, i.e. if a star with a larger mass than that value was measured, our shaded region would disappear. [For the two additional parameter sets in the lower panels, these values are $M \simeq 2.36\,M_\odot$ (green) and $M \simeq 2.23\,M_\odot$ (red).]
- Appearance of hyperons. Parameter choices above the dashed-dotted curve in the upper right panel lead to the appearance of hyperons. More precisely, to plot this curve we have for each d determined the M_0 at which we first see the appearance of (any) strange degrees of freedom just below the chiral phase transition, i.e., at the lower density of the density jump. We find that hyperons only appear for very large values of M_0 . Although the boundaries of the grey band $M_0 \simeq (0.7 0.8) m_N$ should not be taken as sharp constraints, it is unlikely that M_0 assumes such a large value. Perhaps more importantly, hyperons only

2.4. Results 61

appear in a region where the maximal masses of compact stars are well below two solar masses. This observation puts our results into the context of the "hyperon puzzle" [75]: while hyperons are expected to appear at sufficiently large chemical potentials they tend to soften the equation of state and thus render large masses of neutron stars impossible. This is exactly what our model shows, and, importantly, within the same model a solution is suggested, namely the appearance of a stiff chirally restored phase before a potential hyperon onset, allowing for sufficiently heavy hybrid stars.

• *Crossover*. The dotted line at even larger M_0 marks the change from a first-order chiral transition to a crossover. In other words, below that line there is a multivalued solution of the stationarity equations at high densities, and for each d we have determined the M_0 where the solution turns into a single-valued curve. As already suggested by Fig. 2.6, the scenario of a chiral crossover is – within our model – incompatible with realistic maximal masses of compact stars.

In the lower two panels of Fig. 2.7 we have added the curves for two different values of the hyperon potential, $\mathcal{U} = -30\,\mathrm{MeV}$ and $\mathcal{U} = -70\,\mathrm{MeV}$. To avoid too much cluttering we do not show the hyperon onset and crossover lines for these cases, but we have checked that they are also above the grey band, i.e., in an empirically unfavored region. In the lower right panel we see that the line separating absolutely stable nuclear matter from the region where the strange quark matter hypothesis is realized (i.e., "N" from "Q") looks qualitatively different for larger (less negative) hyperon potentials. This gives rise to a second, disconnected sN region, which, however, is disfavored due its incompatibility with the empirical constraints for M_0 . We also observe that for less negative values the shaded area leaves the grey band. Sufficiently heavy stars still exist in the grey band, but not in conjunction with asymptotic strangeness, which tends to disappear if \mathcal{U} is made less negative or even positive. As we mentioned at the end of Sec. 2.3.2, in the realistic parameter regime the hyperon potentials are effectively only relevant for the chirally restored phase, fixing the interactions between light degrees of freedom because actual hyperons do not appear in this parameter regime. If, on the other hand, we go to even more negative \mathcal{U} , the triangular region itself becomes smaller and smaller as it moves to larger values of M_0 and smaller L. As a consequence, the most important conclusion from the lower plots is that the prediction for the value of *L* is not altered much by

allowing the hyperon potential to vary. The lower left panel suggests that independently of the value of the hyperon potential the allowed region of L turns out to be $L \simeq (88-92)$ MeV. This is a remarkably narrow range, which can be expected to become somewhat larger by exhausting the remaining uncertainties in the incompressibility K and the symmetry energy S.

2.5 Summary

We have discussed cold and dense matter undergoing a chiral phase transition within a nucleon-meson model. The main idea has been to include strange baryonic degrees of freedom in the Lagrangian, not necessarily to account for hyperons, which may or may not be favored, but to create a chirally restored phase that resembles strange quark matter. We have pointed out that it is possible to choose the parameters of the model such that flavor-symmetric matter is obtained at ultra-high densities, as expected from asymptotically dense three-flavor quark matter in QCD. However, in this parameter regime the model does not produce compact stars with masses that meet the astrophysical constraints. Therefore, we have mainly explored a parameter region which is not flavor-symmetric asymptotically, but still has nonzero strangeness for large densities and a speed of sound that approaches the conformal limit, as expected from QCD.

Within this parameter region, we have shown that qualitatively different scenarios are possible regarding the chiral phase transition (first order vs. crossover) and the onset of strangeness (within the baryonic phase as hyperons vs. only in the chirally restored phase). Requiring the model to produce compact stars of at least 2.1 solar masses and the correct saturation properties of symmetric nuclear matter disfavors a chiral crossover and the appearance of hyperons. The heaviest stars in the model turn out to be hybrid stars, which can be traced back to a large speed of sound in the chirally restored phase, which peaks just after the chiral phase transition. Furthermore, putting together low-density and astrophysical constraints we have shown that the poorly known slope parameter of the symmetry energy is narrowed down to about $L \simeq (88-92)\,\mathrm{MeV}$. Due to the phenomenological nature of the model and the simplifications we have made, these numbers should of course be taken with some care.

2.5. Summary 63

The main motivation for developing this setup was to provide a unified approach for both quark and hadron phases which enables us to consistently compute properties of matter in the vicinity of the chiral phase transition, such as the surface tension, the free energy of a mixed phase, or the possible existence of an inhomogeneous chiral condensate, for instance in the form of a chiral density wave (which we deal with in Chapter 3). Especially in view of the significance of (global) electric charge neutrality in a neutron star, the inclusion of strangeness has been a step forward because starting with non-strange baryonic degrees of freedom leaves us with no negative charge carriers (except for leptons) in the chirally symmetric phase. These applications of the model are thus natural directions for the future.

Chapter 3

Chiral crossover vs chiral density wave in nuclear matter

3.1 Introduction

The work presented in this chapter has already been published in [2].

In the previous chapter we developed a model with the goal to obtain a qualitatively accurate representation of the chiral phase transition, with the aim to calculate quantities associated with it. In this chapter the goal is to investigate the viability of an anisotropic phase (namely the Chiral Density Wave) as the ground state of the system in this region. Due to the more complicated nature of the problem we drop some of the features that we introduced in the previous iteration of the model, namely the strangeness sector and the neutron star conditions. We restrict ourselves to neutron/proton matter only and impose isospin symmetry. However, we include something that proves to be a significant contribution to the dynamics of the system: the Dirac sea contribution. It is a step forward in the sense that it reinforces the theoretical foundations of our model.

3.1.1 Background and motivation

Thermodynamic phases that break rotational and/or translational invariance are ubiquitous in condensed-matter systems and are expected to play an important role in

the phase diagram of Quantum Chromodynamics (QCD). Cold and dense matter governed by QCD can be found inside neutron stars and thus the properties of anisotropic or crystalline phases are important for the understanding of astrophysical data. Neutron stars rotate and contain strong magnetic fields, effects that tend to stabilize anisotropic structures on a microscopic level. But, even without any external fields, cold and dense matter is prone to developing spatial structures, typically because a condensation mechanism becomes "stressed". A non-uniform state can then be stabilized as a result of competing effects, finding a balance between keeping the kinetic energy cost small while sustaining a gain from condensation energy. In cold and dense quark matter, a mismatch in Fermi momenta due to the nonzero strange quark mass puts a stress on the uniform quark/quark pairing, resulting in anisotropic or crystalline Cooper pair condensates [42, 161, 162]. Here we will be concerned with the possibility of an anisotropic *chiral* condensate. In this case, the baryon chemical potential itself imposes a stress on the condensation mechanism because chiral condensation is based on quark/anti-quark pairing. Throughout this work we will ignore the possibility of Cooper pairing for simplicity and consider systems without magnetic field or rotation.

Since the anisotropic state is an intermediate phase between chirally broken and (approximately) chirally restored phases, we expect a spatially varying chiral condensate in the vicinity of the chiral transition¹. Chiral (and deconfinement) transitions are strong-coupling phenomena and cannot be described with perturbative methods. Moreover, in the region of cold and dense matter, even brute-force methods on the lattice are currently inapplicable. Therefore, for now, this regime of QCD is inaccessible from first principles. The discussion of the chiral transition in cold and dense matter is thus mostly limited to phenomenological models, including the study of inhomogeneous phases in its vicinity. The vast majority of these studies have been performed in models based on quark degrees of freedom, such as the Nambu–Jona-Lasinio (NJL) or quark-meson model [51–63]. These models are, at best, suitable for the high-density side of the chiral transition. However, the relevant degrees of freedom on the low-density side, where chiral symmetry is spontaneously broken, are nucleons. Therefore, these models only yield a toy version of the chirally

¹It is conceivable that an anisotropic or inhomogeneous chiral condensate persists up to asymptotically large densities – then in the form of quark/quark-hole pairing. However, in QCD this requires a large number of colors [163, 164].

3.1. Introduction 67

broken phase of cold and dense QCD. Ideally, a model should account for both quark and nuclear matter. This is a very challenging task, even on the less rigorous level of phenomenological models. Attempts include models where quark and nucleon degrees of freedom are combined in the Lagrangian [165] and models based on the gauge-gravity duality, where both confined and deconfined phases arise naturally but which are different from real-world QCD in other aspects [94–96].

3.1.2 Model and main idea

Here, we employ a nucleon-meson model [104], which offers a complementary perspective to NJL and quark-meson models: In this approach, the low-density side does contain the correct degrees of freedom (and we can choose the model parameters to reproduce properties of nuclear matter at saturation). On the other hand, we have to live with a toy version of quark matter. One of the main ideas is that, if combined, the two complementary approaches can give solid predictions for QCD, at least on a qualitative level. Importantly, our model does have a chiral limit, and thus knows about the concept of a chiral phase transition. The reason is that the nucleon mass is generated fully dynamically, in contrast to widely used models for dense nuclear matter that contain a mass parameter in the Lagrangian, such as the Walecka model and its variants [45, 99, 102, 166]. The model we employ was already used in the context of the chiral transition, for instance to compute the surface tension of the interface between the two phases [97], and strangeness was included to account for a somewhat more realistic description of the chirally symmetric phase [1]. It was also used to construct mixed phases under neutron star conditions [49]. A mixed phase is another example of a spatially inhomogeneous structure, with spatial regions, for instance bubbles, of one phase immersed in the background of another phase. In the context of the quark-hadron transition, the possibility of mixed phases is closely related to a first-order transition in the presence of a local charge neutrality constraint and the relaxation of this constraint to global neutrality. In this chapter, we restrict ourselves to isospin-symmetric nuclear matter without any neutrality condition, where these mixed phases play no role.

Instead, we will allow for an anisotropic chiral condensate, which oscillates between scalar and pseudoscalar components along a certain, spontaneously chosen, direction in position space – this is commonly referred to as a chiral density wave (CDW)². The CDW has been used as an ansatz for the chiral condensate in numerous studies because of its simplicity. In particular, it does not break translational invariance for any observable. More complicated structures have been discussed, for instance spatial variations in the scalar component only [52, 63], variants of the chiral density wave [168], higher-dimensional lattice structures [169, 170], all reviewed in Ref. [171], and the possibility of a quantum spin liquid [172]. It is not the purpose of our study to compare these different inhomogeneous phases, hence we need to keep in mind that our CDW phase may itself be unstable with respect to a phase that does break translational invariance.

3.1.3 Main novelties

The chiral density wave in nuclear matter was already analyzed in Refs. [64–66], employing a model similar to ours, and in Refs. [67, 168], where an extended linear sigma model was used, describing nucleons in a parity doublet and, in Ref. [67], including an additional scalar field. All these works ignore the vacuum contribution of the nucleons (the "Dirac sea"), and we will argue that this contribution makes an important difference. This difference is important not only if a CDW is included. (In Ref. [98] it was argued that the Dirac sea is crucial in the presence of a magnetic field.) Even for the isotropic case, the location and nature of the chiral phase transition is corrected significantly by the vacuum contribution, as already pointed out in the model we use here [173]. In models with quark degrees of freedom, on the other hand, the Dirac sea was included together with the CDW, at least in some of the above mentioned works, see for instance Refs. [55, 59]. Implementing this contribution for the first time into a study of the CDW in nuclear matter gives us a more realistic picture. Moreover, we carefully discuss the renormalization needed for the Dirac sea and point out that a suitable renormalization procedure avoids artifacts at high density seen previously in NJL and quark-meson approaches [54, 55]. Additionally, we will show how the CDW is affected by a quartic self-coupling of the vector meson

²Other names for the CDW exist in the literature, such as "axial wave condensation", "dual chiral density wave", or "chiral spiral". The analogue in quark/quark pairing (as opposed to quark/anti-quark pairing in the chiral condensate) is referred to as the single plane wave Larkin-Ovchinnikov-Fulde-Ferrell (LOFF) state. The CDW is also conceptually the same as a superfluid with nonzero superflow in a fixed direction, described by a complex scalar field whose phase varies along this direction (which can be visualized as a spiral) [167].

[100], which was not taken into account in Refs. [64–67, 168], but which has recently been explored to account for realistic neutron stars [48, 174]. We also ask whether a CDW is favored in a system which – in the absence of anisotropic phases – shows a smooth chiral crossover. As we shall see, the crossover is an unavoidable consequence of our model if the Dirac sea is included, and thus we are "forced" to work in this scenario, which is a viable possibility in QCD [141]. And we shall see that an anisotropic chiral condensate can indeed introduce phase transitions in an otherwise smooth crossover. This is not unlike the Bose-Einstein condensation/Bardeen-Cooper-Schrieffer crossover [167], which can also be disrupted by phase transitions if there is a mismatch in Fermi momenta for the two fermion species that form pairs [175, 176].

3.1.4 Structure of the chapter

This chapter is organized as follows. In Sec. 3.2 we introduce our model of isospin-symmetric nuclear matter and incorporate the CDW, see Secs. 3.2.1 and 3.2.2. Then, in Secs. 3.2.3 and 3.2.4 we derive the free energy and set up the stationarity equations, including the Dirac sea contribution, which requires renormalization, explained in detail in Appendix C. We explain our procedure for fitting the model parameters in Sec. 3.2.5. Our main results are presented in Sec. 3.3, starting from the effect of the vacuum terms on the isotropic scenario in Sec. 3.3.1. The CDW is studied in Sec. 3.3.2 for a specific parameter set, before we present a more global view of the parameter space in Sec. 3.3.3. We compare our results to previous approaches in the literature regarding the treatment of the Dirac sea in Sec. 3.3.4, before we give a summary and an outlook in Sec. 3.4.

3.2 Model and ansatz

3.2.1 Lagrangian

Our model is based on a Lagrangian containing baryonic, mesonic, and interaction terms [1, 49, 97, 104, 173],

$$\mathcal{L} = \mathcal{L}_{\text{bar}} + \mathcal{L}_{\text{mes}} + \mathcal{L}_{\text{int}}. \tag{3.1}$$

The baryonic part is

$$\mathcal{L}_{\text{bar}} = \bar{\psi}(i\gamma^{\mu}\partial_{\mu} + \gamma^{0}\mu)\psi, \qquad (3.2)$$

where the nucleon spinor contains neutrons and protons, $\psi = (\psi_n, \psi_p)$, and μ is the baryon chemical potential. Throughout this chapter, we will restrict ourselves to isospin-symmetric nuclear matter, where neutrons and protons are degenerate and in particular have the same chemical potential, $\mu_n = \mu_p \equiv \mu$. The Lagrangian does not include a nucleonic mass parameter, the nucleon mass will be generated dynamically by spontaneous chiral symmetry breaking. The mesonic part is

$$\mathcal{L}_{\text{mes}} = \frac{1}{2} \partial_{\mu} \sigma \partial^{\mu} \sigma + \frac{1}{4} \text{Tr} [\partial_{\mu} \pi \partial^{\mu} \pi] - \frac{1}{4} \omega_{\mu\nu} \omega^{\mu\nu} + \frac{m_{\omega}^{2}}{2} \omega_{\mu} \omega^{\mu} + \frac{d}{4} (\omega_{\mu} \omega^{\mu})^{2} - \mathcal{U}(\sigma, \pi),$$
(3.3)

where $\pi = \pi_a \tau_a$ with the Pauli matrices τ_a is the pion field, where $\omega_{\mu\nu} \equiv \partial_{\mu}\omega_{\nu} - \partial_{\nu}\omega_{\mu}$, where $m_{\omega} = 782\,\text{MeV}$ is the vector meson mass, and where d>0 is the (dimensionless) self-coupling constant of the vector meson. The potential for the sigma and pion fields takes the form

$$\mathcal{U}(\sigma, \pi) = \sum_{n=1}^{4} \frac{a_n}{n!} \frac{(\sigma^2 + \pi_a \pi_a - f_{\pi}^2)^n}{2^n} - \epsilon(\sigma - f_{\pi}), \qquad (3.4)$$

with parameters $a_1, a_2, a_3, a_4, \epsilon$, and the pion decay constant $f_\pi = 93$ MeV. The potential incorporates a (small) explicit chiral symmetry breaking through the parameter ϵ , which is proportional to the pion mass. For $\epsilon = 0$ the Lagrangian is invariant under chiral transformations. Finally, baryons and mesons are assumed to interact via the Yukawa interaction

$$\mathcal{L}_{\text{int}} = -\bar{\psi} \left[g_{\sigma}(\sigma + i\gamma^5 \pi) + g_{\omega} \gamma^{\mu} \omega_{\mu} \right] \psi, \qquad (3.5)$$

with coupling constants g_{σ} and g_{ω} .

3.2.2 Ansatz and mean-field approximation

In the simplest situation, only the fields σ and ω^0 develop expectation values. We separate them from the fluctuations, $\sigma \to \phi + \sigma$, $\omega^0 \to \omega + \omega^0$, where $\phi \equiv \langle \sigma \rangle$, $\omega \equiv \langle \omega^0 \rangle$ are density-dependent (and in general also temperature-dependent) condensates. If we assume isotropy, ϕ and ω are constant in space. In our more

general – anisotropic – ansatz we keep the vector meson condensate ω spatially constant and introduce a spatial modulation in the sector of scalar and pseudoscalar condensates in the form of a CDW,

$$\sigma = \phi \cos(2\vec{q} \cdot \vec{x}), \quad \pi_3 = \phi \sin(2\vec{q} \cdot \vec{x}). \tag{3.6}$$

Here, the wave vector \vec{q} breaks rotational invariance spontaneously, and its modulus q as well as the condensate ϕ have to be determined dynamically. We have set any charged pion condensate to zero; its competition and possible coexistence with the CDW is worth exploring in systems with isospin asymmetry [59, 64]. It is useful to work with transformed fermionic fields according to

$$\psi \to e^{-i\gamma^5 \tau_3 \vec{q} \cdot \vec{x}} \psi \,. \tag{3.7}$$

Using this transformation and neglecting the mesonic fluctuations, we can write the "mean-field Lagrangian" as

$$\mathcal{L}_{\rm mf} = \bar{\psi}(i\gamma_{\mu}\partial^{\mu} + \gamma^{0}\mu_{*} - M + \gamma^{5}\vec{q}\cdot\vec{\gamma}\,\tau_{3})\psi + \frac{m_{\omega}^{2}}{2}\omega^{2} + \frac{d}{4}\omega^{4} - U - \Delta U, \qquad (3.8)$$

where we have introduced the effective nucleon mass,

$$M = g_{\sigma} \phi \,, \tag{3.9}$$

and the effective chemical potential,

$$\mu_* = \mu - g_\omega \omega \,. \tag{3.10}$$

The mesonic vacuum potential is written as a sum of isotropic and *q*-dependent contributions,

$$U \equiv U(\phi) \equiv \sum_{n=1}^{4} \frac{a_n}{n!} \frac{(\phi^2 - f_{\pi}^2)^n}{2^n} - \epsilon(\phi - f_{\pi}), \quad \Delta U \equiv \Delta U(\phi, q) \equiv 2\phi^2 q^2 + (1 - \delta_{0q}) \epsilon \phi.$$
(3.11)

The form of the q-dependent part deserves a comment. First of all, the term $2\phi^2q^2$ originates from the kinetic term in Eq. (3.3) and corresponds to a kinetic energy cost of creating an axial current from the mesonic sector. Next, we notice that the explicit symmetry breaking term in the potential (3.4) retains a spatial dependence that cannot

be transformed away by the fermionic transformation (3.7). This spatial dependence is easy to understand: Even without the presence of nucleons the CDW ansatz (3.6) is only a solution to the Euler-Lagrange equations for σ and π_3 in the chiral limit $\epsilon=0$; in that case, the solution traces a circle in the σ - π_3 plane. An explicit symmetry breaking term $\epsilon>0$ "tilts" the vacuum potential and the solution will no longer be circular; the condensate will "wobble" along the spatial direction parallel to \vec{q} rather than smoothly follow a regular spiral³. This effect is ignored by working with the simple CDW ansatz, and we will minimize the *spatially averaged* free energy with respect to ϕ and \vec{q} rather than attempting to work with the spatially nontrivial solution of the Euler-Lagrange equation. (Let alone attempting to find a self-consistent solution in the presence of the nucleons.) For convenience, we already introduce the spatial averaging on the level of the mean-field Lagrangian. After separating the $\vec{q}=0$ contribution, this amounts to replacing

$$\epsilon \phi [1 - \cos(2\vec{q} \cdot \vec{x})] \rightarrow \frac{\epsilon \phi}{V} \int d^3\vec{x} \left[1 - \cos(2\vec{q} \cdot \vec{x})\right] = \epsilon \phi \left[1 - \frac{\sin(qL_q)}{qL_q}\right] \rightarrow \epsilon \phi$$
, (3.12)

where V is the volume of the system and L_q its length in the direction of \vec{q} . In the last step, we have taken $L_q \to \infty$ at fixed nonzero wave number q to obtain the contribution to ΔU given in Eq. (3.11). We see that the result does not depend on q; in particular, taking the limit $q \to 0$ now does not change the contribution. If, on the other hand, we are interested in the isotropic case, we first let $q \to 0$ and then take the thermodynamic limit $L_q \to \infty$, in which case the contribution (3.12) vanishes. This $q \to 0$ discontinuity results in the prefactor $1 - \delta_{0q}$ in Eq. (3.11). It implies that it is energetically more costly by a finite amount to have an infinitesimally small winding per unit length (i.e., wavelength going to infinity) compared to the constant zero-winding solution. Again, this is a consequence of the explicit symmetry breaking and our use of the CDW ansatz; the discontinuity is absent in the chiral limit $\epsilon = 0$.

³We have solved the Euler-Lagrange equations for σ and π_3 numerically in the absence of nucleons – but with "tilt" – and found that for small ϵ the solution resembles the "shifted CDW" of Ref. [168], but assumes more irregular shapes as ϵ is increased.

3.2.3 Free energy

The (yet to be renormalized) free energy from the Lagrangian (3.8) is

$$\Omega = \Omega_{\text{bar}} - \frac{m_{\omega}^2}{2}\omega^2 - \frac{d}{4}\omega^4 + U + \Delta U, \qquad (3.13)$$

with the baryonic contribution Ω_{bar} , which is derived as follows.

We first observe that the nucleonic sector of the mean-field Lagrangian (3.8) is formally equivalent to a Lagrangian of free fermions. The thermodynamics can thus be straightforwardly computed without further approximations. To this end, we need to compute the fermionic spectrum in the presence of the CDW. We first identify the inverse nucleon propagator in momentum space,

$$S^{-1}(K) = -\gamma^{\mu} K_{\mu} + M - \mu_* \gamma^0 + \vec{q} \cdot \vec{\gamma} \gamma^5 \tau_3, \qquad (3.14)$$

where $K=(k_0,\vec{k})$, and $k_0=-i\omega_n$ with the fermionic Matsubara frequencies $\omega_n=(2n+1)\pi T$, where T is the temperature and $n\in\mathbb{Z}$. The poles of the propagator S(K) are given by the zeros of the determinant of $S^{-1}(K)$, which can be factorized as follows,

$$\det S^{-1} = [(k_0 + \mu_*)^2 - (E_k^+)^2]^2 [(k_0 + \mu_*)^2 - (E_k^-)^2]^2, \tag{3.15}$$

with the single-nucleon energies

$$E_k^{\pm} = \sqrt{\left(\sqrt{k_\ell^2 + M^2} \pm q\right)^2 + k_\perp^2}$$
 (3.16)

Here we have introduced longitudinal and transverse components of the single-particle momentum \vec{k} with respect to the direction of the CDW, $\vec{k}_{\ell} = \hat{q} \, \hat{q} \cdot \vec{k}$, $\vec{k}_{\perp} = \vec{k} - \hat{q} \, \hat{q} \cdot \vec{k}$. We see from Eq. (3.16) that the wave vector \vec{q} introduces two different dispersion relations which would otherwise be degenerate. In our model, the dispersions have a very simple analytical form despite the presence of the CDW. This will be particularly useful for the regularization of the vacuum contribution, which can be done analytically. This is in contrast to the extended linear sigma model of Ref. [67], where the dispersions are complicated solutions of a quartic polynomial.

Now, following the standard procedure of thermal field theory, we can compute the free energy density from the logarithm of the partition function. After performing the sum over Matsubara frequencies, we obtain the baryonic contribution

$$\Omega_{\text{bar}} = -2\sum_{e=+}^{\infty} \sum_{s=+}^{\infty} \int \frac{d^3\vec{k}}{(2\pi)^3} \left\{ \frac{E_k^s}{2} + T \ln\left[1 + e^{-(E_k^s - e\mu_*)/T}\right] \right\} , \tag{3.17}$$

where the prefactor 2 indicates the degeneracy of neutrons and protons. The free energy density Ω does not depend on space and thus all thermodynamic quantities will be homogeneous as well. This reflects the fact that translation symmetry is unbroken by the CDW – at least in the chiral limit and within our approximation also in the presence of a nonzero pion mass. Of course, Ω does depend on the vector \vec{q} and thus the anisotropy does show up in physical observables.

In all our results we restrict ourselves to zero temperature. In this case, with $\mu_* > 0$, there is no anti-particle matter, i.e., the logarithm is only nonzero for e = +1. We obtain

$$\Omega_{\text{bar}} = -2(P_{\text{vac}} + P_{\text{mat}}), \qquad (3.18)$$

with the (divergent) vacuum pressure of a single fermionic degree of freedom,

$$P_{\text{vac}} \equiv \frac{1}{2\pi^2} \sum_{c=\pm} \int_0^\infty dk_\ell \int_0^\infty dk_\perp k_\perp E_k^s, \qquad (3.19)$$

and the corresponding (finite) matter part,

$$P_{\text{mat}} \equiv \frac{1}{2\pi^2} \sum_{s=\pm} \int_0^\infty dk_\ell \int_0^\infty dk_\perp k_\perp (\mu_* - E_k^s) \Theta(\mu_* - E_k^s) \,. \tag{3.20}$$

We have written the momentum integral in cylindrical coordinates and employed invariance of the integrand under $k_{\ell} \rightarrow -k_{\ell}$.

The double integral in the matter part can be evaluated analytically. After some tedious algebra due to the step function one can write the result as

$$P_{\text{mat}} = \frac{\Theta(\mu_* - q - M)}{16\pi^2} \left\{ M^2 [M^2 + 4q(q - \mu_*)] \ln \frac{\mu_* - q + k_-}{M} + \frac{k_-}{3} [2(\mu_*^2 - q^2)(\mu_* - q) - M^2(5\mu_* - 13q)] \right\}$$

$$+ \frac{\Theta(\mu_* + q - M)}{16\pi^2} \left\{ M^2 [M^2 + 4q(q + \mu_*)] \ln \frac{\mu_* + q + k_+}{M} + \frac{k_+}{M} [2(\mu_*^2 - q^2)(\mu_* + q) - M^2(5\mu_* + 13q)] \right\}$$

$$+ \frac{\Theta(q - \mu_* - M)}{16\pi^2} \left\{ M^2 [M^2 + 4q(q - \mu_*)] \ln \frac{q - \mu_* + k_-}{M} - \frac{k_-}{3} [2(\mu_*^2 - q^2)(\mu_* - q) - M^2(5\mu_* - 13q)] \right\}$$

$$- \frac{\Theta(q - M)}{8\pi^2} \left[M^2 (M^2 + 4q^2) \ln \frac{q + \sqrt{q^2 - M^2}}{M} - \frac{\sqrt{q^2 - M^2}}{3} q(2q^2 + 13M^2) \right], \qquad (3.21)$$

where we have abbreviated

$$k_{\pm} \equiv \sqrt{(\mu_* \pm q)^2 - M^2}$$
 (3.22)

As a check, one finds for q = 0,

$$P_{\text{mat}} = \frac{\Theta(\mu_* - M)}{8\pi^2} \left[\mu_* k_F \left(\frac{2}{3} k_F^2 - M^2 \right) + M^4 \ln \frac{\mu_* + k_F}{M} \right] , \qquad (3.23)$$

where $k_F = \sqrt{\mu_*^2 - M^2}$ is the Fermi momentum. This is the zero-temperature pressure of a non-interacting fermion gas with chemical potential μ_* and fermion mass M.

Moreover, for M = 0 we find

$$P_{\text{mat}} = \frac{\mu_*^4}{12\pi^2},\tag{3.24}$$

which is the pressure of massless fermions. In particular, the wave number q has dropped out. This is expected since any modulation is irrelevant if the amplitude, here M, is zero.

The Dirac sea contribution P_{vac} has to be treated more carefully. We explain all details in Appendix C and proceed here with a short summary and the final result for the renormalized free energy. We first employ proper time regularization to identify the divergent contributions, which we can express in terms of a proper time cutoff Λ and a renormalization scale ℓ . Then, we renormalize our model by introducing the renormalized field ϕ_r and renormalized parameters $f_{\pi,r}, g_{\sigma,r}, a_{n,r}, \epsilon_r$. They are related to the bare quantities of the original Lagrangian by counterterms δa_n and a field rescaling factor Z for the sigma and pion fields. The divergent parts of δa_n and Z are fixed to cancel the divergences of P_{vac} . The q=0 part of the Dirac sea is uniquely determined by our fit of the model parameters to properties of nuclear matter, and no dependence on the choice of the finite parts of δa_n , Z, and on the scale ℓ is left. The q-dependent part, however, is less straightforward, and we keep the scale ℓ in the following results to discuss our choice for it carefully. Dropping for notational convenience the subscript r from the renormalized quantities, the calculation in Appendix C yields

$$\Omega = -2P_{\text{mat}} - \frac{m_{\omega}^2}{2}\omega^2 - \frac{d}{4}\omega^4 + \tilde{U} + \Delta\tilde{U}. \tag{3.25}$$

The renormalized Dirac sea contribution is absorbed in the modified contributions to the meson potential,

$$\tilde{U} \equiv \tilde{U}(\phi) \equiv U(\phi) + \frac{m_N^4}{96\pi^2} (1 - 8\varphi^2 - 12\varphi^4 \ln \varphi^2 + 8\varphi^6 - \varphi^8),$$
 (3.26a)

$$\Delta \tilde{U} \equiv \Delta \tilde{U}(\phi, q) \equiv \Delta U(\phi, q) - \frac{q^2 M^2}{2\pi^2} \ln \frac{M^2}{\ell^2} - \frac{q^4}{2\pi^2} F(y), \qquad (3.26b)$$

where

$$\varphi \equiv \frac{\phi}{f_{\pi}} = \frac{M}{m_N},\tag{3.27}$$

with the nucleon mass in the vacuum $m_N = 939 \,\mathrm{MeV}$, and

$$F(y) \equiv \frac{1}{3} + \Theta(1-y) \left[-\sqrt{1-y^2} \frac{2+13y^2}{6} + 2y^2 \left(1 + \frac{y^2}{4}\right) \ln \frac{1+\sqrt{1-y^2}}{y} \right], \quad (3.28)$$

with

$$y \equiv \frac{M}{q} \,. \tag{3.29}$$

The terms in \tilde{U} generated by the nucleonic Dirac sea are of order

 $(\phi^2-f_\pi^2)^5\sim (\phi^2-1)^5$ and higher. The reason is that we fit all coefficients in front of $(\phi^2-1)^n$ with $n\leq 4$ to reproduce physical quantities, and thus the corrections by the Dirac sea to the terms up to order $(\phi^2-1)^4$ are absorbed by the fit.

The q-dependent contribution of the Dirac sea in $\Delta \tilde{U}$ contains the renormalization scale ℓ . Let us discuss two limits that will serve us to choose ℓ . Firstly, in the vacuum, where $\omega = P_{\text{mat}} = 0$, $\phi = f_{\pi}$ (i.e., $M = m_N$), we find in the chiral limit, where $\epsilon = 0$,

vacuum:
$$\Omega = 2f_{\pi}^2 q^2 \left(1 - \frac{g_{\sigma}^2}{4\pi^2} \ln \frac{m_N^2}{\ell^2} \right) - \frac{q^4}{6\pi^2}, \tag{3.30}$$

where we have assumed $q < m_N$, such that the step function in Eq. (3.28) vanishes. Secondly, in the limit of large q, with all other quantities kept finite, we have

large
$$q$$
: $\Omega = \frac{q^2 M^2}{2\pi^2} \left(2 + \frac{4\pi^2}{g_{\sigma}^2} - \ln \frac{4q^2}{\ell^2} \right) + \mathcal{O}(q^0)$. (3.31)

[F(y) contributes to the logarithm and the matter part reduces to the limit (3.24) and thus is subleading.] We now require that for small q in the vacuum $\Omega = 2f_{\pi}^2q^2 + \mathcal{O}(q^4)$ [55, 177] and that the free energy be bounded from below as $q \to \infty$. Consequently, a natural, albeit not unique, choice is

$$\ell = \sqrt{m_N^2 + (2q)^2} \,. \tag{3.32}$$

The q-dependence is crucial to avoid the unboundedness of the free energy, which was identified as a problem in previous works in similar models [55, 177]. Since q will be determined dynamically as we vary the chemical potential, the scale ℓ depends on the medium. This is typical for perturbative calculations in renormalizable theories such as QCD, if applied to nonzero temperatures and/or densities [178–180]. At the end of Sec. 3.3.3, we shall further discuss the choice (3.32) by comparing our results to the ones obtained with $\ell = m_N$, where Ω is unbounded from below.

3.2.4 Stationarity equations

The thermodynamically stable phases are determined by minimizing the renormalized free energy with respect to the condensates ϕ , ω , and the wave number q,

$$\frac{\partial\Omega}{\partial\phi} = \frac{\partial\Omega}{\partial\omega} = \frac{\partial\Omega}{\partial q} = 0. \tag{3.33}$$

All derivatives are taken with the two other dynamical quantities, the chemical potential, and the scale ℓ kept fixed. The minimization with respect to q is equivalent to requiring the total axial current to vanish; for a nonzero q this means that there will be counter-propagating currents from the mesonic and the baryonic sectors which cancel each other. More explicitly, the stationarity equations (3.33) read

$$g_{\sigma}n_{s} = -\tilde{U}'(\phi) - 4q^{2}\phi \left[1 - \frac{g_{\sigma}^{2}}{4\pi^{2}}\left(1 + \ln\frac{M^{2}}{\ell^{2}}\right)\right] - (1 - \delta_{0q})\epsilon + \frac{g_{\sigma}q^{3}}{2\pi^{2}}F'(y), \quad (3.34a)$$

$$g_{\omega}n_{B} = m_{\omega}^{2}\omega + d\omega^{3}, \qquad (3.34b)$$

$$j = -4q\phi^2 \left(1 - \frac{g_\sigma^2}{4\pi^2} \ln \frac{M^2}{\ell^2}\right) + \frac{q^3}{2\pi^2} [4F(y) - yF'(y)], \qquad (3.34c)$$

where we have introduced the scalar density n_s , the baryon density n_B , and the contribution to the axial current from the baryons j,

$$n_s = -2\frac{\partial P_{\text{mat}}}{\partial M}, \qquad n_B = 2\frac{\partial P_{\text{mat}}}{\partial \mu}, \qquad j = -2\frac{\partial P_{\text{mat}}}{\partial q}.$$
 (3.35)

These quantities are computed straightforwardly from the expression (3.21). For completeness, and for a brief discussion of their limits, we present their explicit expressions in Appendix C.3.

3.2.5 Fitting parameters

Since we fit our parameters to vacuum properties and the properties of nuclear matter in the absence of the CDW, the matching procedure is very similar to our previous works within the same model [1, 49, 97]. Due to empirical uncertainties and in order to explore all qualitatively different scenarios of the model, we shall not simply work with a single parameter set but explore the parameter space of the model within and

somewhat beyond these uncertainties. It is therefore useful to explain the details of our parameter fitting.

We first fit g_{σ} from the vacuum mass of the nucleon, $m_N = g_{\sigma} f_{\pi}$, where we have used that in the vacuum $\phi = f_{\pi}$. Next, we compute the pion and sigma masses by temporarily reinstating mesonic fluctuations about the q=0 vacuum. This can be done for instance by replacing $\phi^2 \to (f_{\pi} + \sigma)^2 + \pi^2$ in the potential \tilde{U} from Eq. (3.26a) and expanding in the fluctuations σ and π . The coefficients in front of the quadratic terms $\pi^2/2$, $\sigma^2/2$ yield the masses squared,

$$m_{\pi}^2 = \frac{\tilde{U}'(f_{\pi}) + \epsilon}{f_{\pi}} = a_1, \qquad m_{\sigma}^2 = \tilde{U}''(f_{\pi}) = m_{\pi}^2 + f_{\pi}^2 a_2.$$
 (3.36)

The first relation is used to fix a_1 from the pion mass m_{π} . In our results, we shall consider both the chiral limit $m_{\pi}=0$ and the physical case $m_{\pi}=139$ MeV. Requiring that $\phi=f_{\pi}$ satisfy (3.34a) in the vacuum then gives $\epsilon=f_{\pi}m_{\pi}^2$. Due to the very uncertain (and not uniquely defined) physical value of m_{σ} we shall not use the second relation to fix a_2 , but use this relation to compute m_{σ} once a_2 is fixed from other constraints, which is useful for a comparison to other models.

The remaining parameters are g_{ω} , a_2 , a_3 , a_4 , and d. We relate them to the following properties of isospin-symmetric nuclear matter at saturation: the binding energy $E_B = -16.3$ MeV, leading to a chemical potential for the baryon onset $\mu_0 \equiv m_N + E_B = 922.7$ MeV, the baryon density $n_0 = 0.153$ fm⁻³, the effective Dirac mass $M_0 \simeq (0.7 - 0.8) m_N$, and the incompressibility $K \simeq (200 - 300)$ MeV. Following Ref. [1], we denote the solution of Eq. (3.34b) at $n_B = n_0$ by

$$\omega_0 = \frac{g_\omega n_0}{m_\omega^2} f(x_0) \,, \tag{3.37}$$

with

$$f(x) \equiv \frac{3}{2x} \frac{1 - (\sqrt{1 + x^2} - x)^{2/3}}{(\sqrt{1 + x^2} - x)^{1/3}}, \qquad x_0 \equiv \frac{3\sqrt{3d} g_\omega n_0}{2m_\omega^3}.$$
 (3.38)

The effective chemical potential at saturation is $\mu_0^* = \mu_0 - g_\omega \omega_0$. Inserting this into Eq. (3.34b) gives a quadratic equation for g_ω^2 with the relevant solution

$$g_{\omega}^{2} = \frac{m_{\omega}^{2}}{2n_{0}}(\mu_{0} - \mu_{0}^{*}) \left[1 + \sqrt{1 + \frac{4dn_{0}(\mu_{0} - \mu_{0}^{*})}{m_{\omega}^{4}}} \right].$$
 (3.39)

Since the effective chemical potential can also be written as $\mu_0^* = \sqrt{k_F^2 + M_0^2}$ with the Fermi momentum at saturation $k_F = (3\pi^2 n_0/2)^{1/3}$, Eq. (3.39) is a relation between the model parameters g_ω and d, all other quantities being physical parameters whose values can be inserted later. We see that at $\mu_0 = \mu_0^*$ the coupling g_ω vanishes, which translates into an upper bound for M_0 ,

$$M_0 < \sqrt{\mu_0^2 - k_F^2} \simeq 0.943 \, m_N \,.$$
 (3.40)

For the remaining parameters a_2 , a_3 , a_4 we set up the following three coupled equations: the definition of the incompressibility K (see for instance Ref. [49] for bringing the definition into the form used here), the free energy of saturated nuclear matter being equal to that of the vacuum (here 0), and the stationarity equation for ϕ (3.34a),

$$0 = \tilde{U}''(\phi) + \frac{g_{\sigma}^{2}}{\pi^{2}} \left(\frac{k_{F}^{3} + 3k_{F}M_{0}^{2}}{\mu_{0}^{*}} - 3M_{0}^{2} \ln \frac{\mu_{0}^{*} + k_{F}}{M_{0}} \right)$$

$$+ \frac{\frac{6g_{\sigma}^{2}k_{F}^{3}}{\pi^{2}} \left(\frac{M_{0}}{\mu_{0}^{*}} \right)^{2}}{K - \frac{6k_{F}^{3}}{\pi^{2}} \frac{g_{\omega}^{2}}{m_{\omega}^{2}} [f(x_{0}) + x_{0}f'(x_{0})] - \frac{3k_{F}^{2}}{\mu_{0}^{*}} '$$

$$(3.41a)$$

$$0 = \frac{m_{\omega}^2}{2}\omega_0^2 + \frac{d}{4}\omega_0^4 - \tilde{U}(\phi) + \frac{1}{4\pi^2} \left[\left(\frac{2}{3}k_F^3 - M_0^2 k_F \right) \mu_0^* + M_0^4 \ln \frac{k_F + \mu_0^*}{M_0} \right], \quad (3.41b)$$

$$0 = \tilde{U}'(\phi) + \frac{g_{\sigma}M_0}{\pi^2} \left(k_F \mu_0^* - M_0^2 \ln \frac{k_F + \mu_0^*}{M_0} \right) , \qquad (3.41c)$$

where the potential \tilde{U} and its derivatives are evaluated at saturation, $\phi = M_0/g_\sigma$. The parameters a_2 , a_3 , a_4 only appear in \tilde{U} and its derivatives. Hence, despite their tedious look, Eqs. (3.41) form a simple system of linear equations for these parameters. As a consequence, we can derive elementary (but very lengthy) analytical expressions for a_2 , a_3 , a_4 purely in terms of physical quantities and the model parameter d.

In our results we shall consider different values of the quartic vector meson coupling d while keeping the aforementioned properties of symmetric nuclear matter at saturation fixed. In order to translate this coupling constant into a more physical quantity, we temporarily consider isospin-asymmetric matter with a Yukawa coupling g_{ρ} between the nucleons and the rho meson. This allows us to relate our parameters to

3.3. Results 81

the symmetry energy $S \simeq (30-34)$ MeV and the "slope parameter" L, which characterizes the change of the symmetry energy under variation of the baryon number. For the exact definitions of S and L see for instance Ref. [1], from which we also quote the relevant relations

$$g_{\rho}^{2} = \frac{3\pi^{2}m_{\omega}^{2}}{k_{F}^{3}} \left(S - \frac{k_{F}^{2}}{6\mu_{0}^{*}} \right) \left(1 + \frac{d\omega_{0}^{2}}{m_{\omega}^{2}} \right),$$

$$L = \frac{3g_{\rho}^{2}n_{0}}{2(m_{\rho}^{2} + d\omega_{0}^{2})} \left[1 - \frac{2d n_{0}g_{\omega}\omega_{0}}{(m_{\rho}^{2} + d\omega_{0}^{2})(m_{\omega}^{2} + 3d\omega_{0}^{2})} \right] + \frac{k_{F}^{2}}{3\mu_{0}^{*}} \left(1 - \frac{K}{6\mu_{0}^{*}} \right)$$

$$+ \frac{g_{\omega}^{2}n_{0}k_{F}^{2}}{2m_{\omega}^{2}\mu_{0}^{*2}} [f(x_{0}) + x_{0}f'(x_{0})],$$

$$(3.42a)$$

with the rho meson mass $m_{\rho} \simeq 776\,\mathrm{MeV}$. We shall work with $S=32\,\mathrm{MeV}$, such that these equations give us a map between d and L if all other model parameters are fixed. The value of L is poorly known, with experimental data indicating a range $L\simeq (40-140)\,\mathrm{MeV}$ [33, 123, 130–133], which is not violated for any d considered in this work.

We summarize our fitting procedure as follows: m_{ω} and g_{σ} are fixed in all cases we consider, and the value of m_{π} fixes a_1 and ϵ ; then, the parameters g_{ω} , a_2 , a_3 , a_4 , d are determined from μ_0 , n_0 , M_0 , K, L, where μ_0 , n_0 are always taken to assume their well-known values, while we will explore the dependence on the less well known M_0 , K, L.

3.3 Results

3.3.1 Isotropic matter: absence of first-order transition due to Dirac sea

To lay the ground for the discussion of the CDW we first focus on the isotropic case q=0. For given M_0 , K, and d we can solve the stationarity equations (3.34a), (3.34b) for ϕ , ω as functions of μ and insert the result back into Eq. (3.25) to compute the corresponding free energy. [The stationarity equation (3.34c) is trivially solved by q=0.] Here, in the isotropic case, the results do not depend on the renormalization scale ℓ . The result for the effective baryon mass M is shown in the left panel of Fig. 3.1, where we have included four cases: with/without Dirac sea and zero/physical pion

mass. The specific values for the model parameters needed to compute these results are given in Table D.1 in Appendix D. We see that in the no-sea approximation the chiral transition is of first order, for either value of the pion mass. The critical chemical potential of the first-order chiral transition is determined by finding the point where the free energies of chirally broken and chirally restored matter are equal. Including the Dirac sea renders the transition second order (chiral limit) or turns it into a crossover (physical pion mass), and moves it to significantly larger values of μ , in accordance with Ref. [173].

Does this observation depend on the specific parameter choice? This question is addressed in the right panel of Fig. 3.1, where we explore the behavior of the chiral phase transition as a function of the parameter M_0 . In this plot we restrict ourselves to the chiral limit to avoid any crossovers, which are difficult to display due to the absence of a well-defined critical chemical potential. For any M_0 we adjust the model parameters such that $K = 250 \,\mathrm{MeV}$ is held fixed (as well as all other properties of symmetric nuclear matter discussed in Sec. 3.2.5). We see that in the no-sea approximation there is a region of small M_0 – in fact covering a large part of the physically most likely values of M_0 – where there is a direct transition from the vacuum to chirally symmetric matter. This means chirally symmetric matter is stable at zero pressure, which is reminiscent of the strange quark matter hypothesis [154, 155]. This interpretation is somewhat far fetched in the current approach but becomes more sensible if strangeness is included, where indeed this behavior persists [1]. In an intermediate range of M_0 we observe a baryon onset from the vacuum to nuclear matter, followed by a first-order chiral transition. This is the scenario of the left panel. Then, for even larger values of M_0 the chiral transition becomes second order (and moves to extremely large μ) even in the no-sea approximation. In the presence of the Dirac sea, the behavior is qualitatively the same for all values of M_0 : The first-order baryon onset at $\mu = \mu_0$ is followed by a second-order chiral transition, shown by the black dashed curves. Even a large mesonic self-coupling $d = 10^4$ does not change this conclusion. We have also varied the incompressibility K within the empirically preferred regime (not shown in the plot) and never found a first-order transition when the Dirac sea is included.

What does this imply for the case of a physical pion mass? The left panel of Fig. 3.1 shows how the second-order transition becomes a crossover if the pion mass is

3.3. Results 83

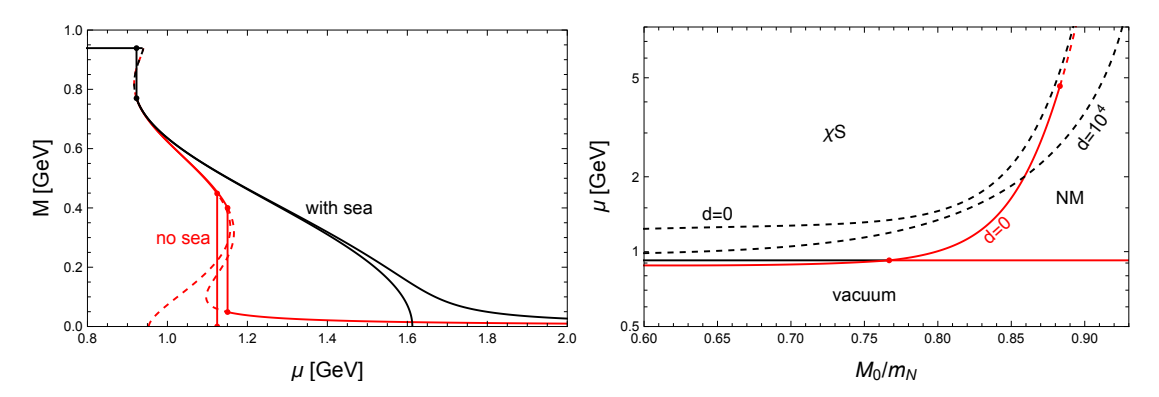


FIGURE 3.1: Effect of the nucleonic vacuum contribution ("Dirac sea") on the chiral phase transition. *Left panel*: Effective nucleon mass M as a function of the baryon chemical potential μ with (black) and without (red) Dirac sea. Solid lines represent stable phases, while dashed lines indicate metastable or unstable solutions. For each color we display the chiral limit (curve connects to the M=0 solution) and the physical case (curve asymptotes to M=0). First-order transitions are marked by solid vertical lines. The baryon onset (small vertical lines at $\mu=\mu_0$) is the same in all cases by construction. The parameters for this panel are $M_0=0.82\,m_N$, $K=250\,\text{MeV}$, d=0. *Right panel*: Phase transitions in the chiral limit upon variation of M_0 , keeping $K=250\,\text{MeV}$, for d=0 (with and without Dirac sea) and $d=10^4$ (for the case with Dirac sea). Colors as in the left panel; solid (dashed) lines are first- (second-) order transitions between vacuum, nuclear matter (NM) and the chirally restored phase (χ S). In the case with Dirac sea, the baryon onset occurs at $\mu=\mu_0$ for all M_0 and d (solid black line, partly covered by the red line).

switched on. Therefore, the result of the right panel indicates that in the presence of a physical pion mass the chiral transition is always a crossover (assuming isotropy). This is the basis on which we now investigate the CDW.

3.3.2 CDW solution

We will now stick to the full calculation that takes into account the Dirac sea and only comment on the differences to the no-sea approximation in Sec. 3.3.4. To find q>0 solutions to the stationarity equations (3.34) it is useful to start with the chiral limit. In this case, the CDW branch can connect continuously to the isotropic solution. The first possibility to connect is with the q=0 nuclear matter branch. The chemical potential where the CDW attaches to this branch can be computed from the $q\to 0$ limit of Eq. (3.34c),

$$\ell \exp\left(\frac{2\pi^2}{g_{\sigma}^2}\right) = M + \Theta(\mu_* - M)(\mu_* - M + \sqrt{\mu_*^2 - M^2}), \tag{3.43}$$

where M and ω (hidden in μ_*) are computed from Eqs. (3.34a) and (3.34b) with q=0. This equation describes the appearance of the CDW via the infinite-wavelength limit

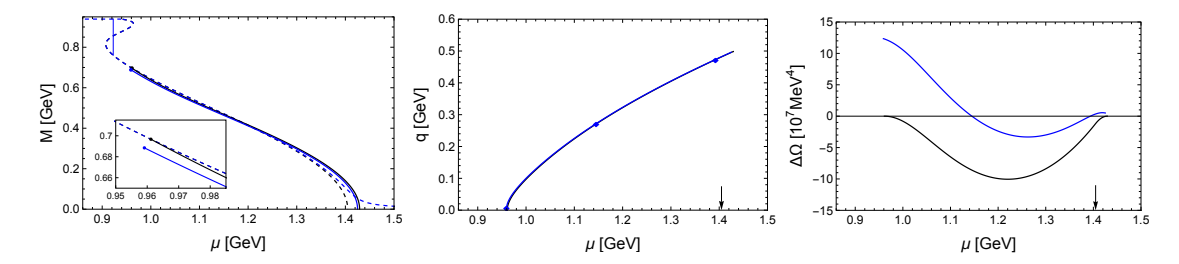


FIGURE 3.2: Effective nucleon mass M (left), wave number q (middle), and free energy of the CDW phase minus that of the thermodynamically stable isotropic phase $\Delta\Omega$ (right), for the chiral limit (black) and the physical pion mass (blue), as functions of the baryon chemical potential μ . The parameters used are $M_0=0.81m_N$, $K=250\,\mathrm{MeV}$, $d=10^4$. The arrow indicates the chiral phase transition in the chiral limit (in the chiral limit, $\Delta\Omega$ is measured relative to the chirally broken phase to the left of the arrow and relative to the chirally restored phase to the right of the arrow). The dashed lines in the left panel are the q=0 curves, including the baryon onset shown as a vertical solid line, while the three markers in the middle panel indicate the points for which we show the nucleonic Fermi surfaces in Fig. 3.3.

at finite amplitude of the chiral condensate. Secondly, the CDW can connect continuously to the chiral solution M=0. The corresponding q and μ can be computed from the $M\to 0$ limit of Eqs. (3.34a) and (3.34c), see also Appendix C.3,

$$\frac{\pi^2}{g_{\sigma}^2} \tilde{U}''(0) + \mu_*^2 - \mu_* q \ln \left| \frac{\mu_* + q}{\mu_* - q} \right| = q^2 \left(\ln \frac{4|\mu_*^2 - q^2|}{\ell^2} - 2 - \frac{4\pi^2}{g_{\sigma}^2} \right), \quad (3.44a)$$

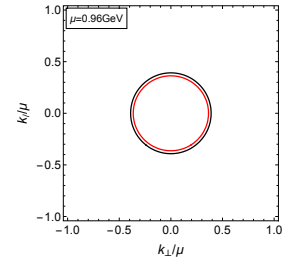
$$- \frac{\mu_* q}{2} \ln \left| \frac{\mu_* + q}{\mu_* - q} \right| = q^2 \left(\ln \frac{4|\mu_*^2 - q^2|}{\ell^2} - 1 - \frac{4\pi^2}{g_{\sigma}^2} \right), \quad (3.44b)$$

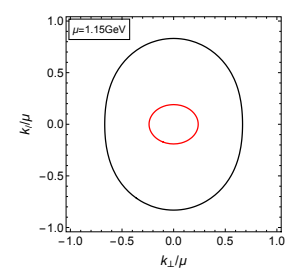
where ω (hidden in μ_*) is computed from Eq. (3.34b) at M=0. These equations describe the appearance of the chiral condensate from the zero-amplitude limit with a finite CDW wavelength. Both Eqs. (3.43) and (3.44) connect the CDW to phases of nonzero baryon density. There is a third option for the CDW branch to end, namely in a $q\neq 0$ vacuum. These exotic vacua, in which the chiral condensate is anisotropic and the nucleons only contribute through the Dirac sea, but not via a nonzero density, play no role for the actual phase structure, as they are thermodynamically disfavored.

We start by discussing the CDW for a specific parameter set with fixed values of M_0 , K, d, and the scale ℓ given by Eq. (3.32). Again, for the precise model parameters used here, see Table D.1 in Appendix D. The numerical solutions are shown in Figs. 3.2 and 3.3. The main observations are as follows.

• Chiral limit. The black curves in Fig. 3.2 show that the second-order isotropic

3.3. Results 85





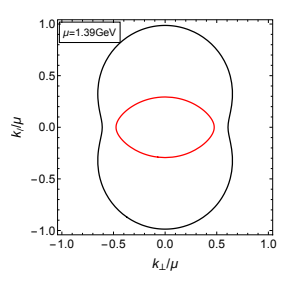


FIGURE 3.3: Fermi surfaces $\mu_* = E_k^+$ (red) and $\mu_* = E_k^-$ (black) in the plane of longitudinal and transverse momentum components with respect to \vec{q} , such that the actual 2-dimensional Fermi surfaces are obtained by rotation around the $k_\perp = 0$ axis. The three plots correspond to three different chemical potentials, as indicated in the middle panel of Fig. 3.2, and are calculated with the physical pion mass (and M_0 , K, d as in Fig. 3.2).

chiral phase transition is replaced by two transitions at $\mu \simeq 0.96\,\mathrm{GeV}$ and $\mu \simeq 1.43\,\mathrm{GeV}$ between which the CDW is energetically favored. The lower end of this region is a nonzero-amplitude, infinite-wavelength transition as described by Eq. (3.43), while the upper end of this region is a zero-amplitude, finite-wavelength transition as described by Eqs. (3.44). The values of the effective mass M (left panel of Fig. 3.2) show that a CDW develops in nuclear matter, and as we move towards larger μ the effective mass decreases such that we observe a CDW in almost chirally symmetric matter.

- Effect of explicit chiral symmetry breaking. The left panel (see zoom-in) and the right panel of Fig. 3.2 show that in the case of a physical pion mass the CDW solution does not connect continuously to the isotropic branch. This is due to the term $\epsilon \phi$ in ΔU (3.11), whose origin is explained below that equation. In particular, the CDW solution admits $M \to 0$ even if m_{π} is nonzero, although it becomes energetically disfavored at a nonzero M. As a consequence, the CDW region is now bounded by two first-order transitions and has shrunk, but not disappeared completely. The CDW exists although, in the absence of anisotropic phases, the chiral transition is a crossover, i.e., the crossover is disrupted by two phase transitions that break (entrance to the CDW) and restore (exit from the CDW) rotational symmetry.
- Fermi surfaces. In Fig. 3.3 we show the Fermi surfaces of the two fermion states $s=\pm$ given by the dispersion relations (3.16). For each dispersion, all states in momentum space (k_ℓ, \vec{k}_\perp) are filled up to the Fermi surface defined by $\mu_*=E_k^s$, as indicated by the step function in Eq. (3.20). For given q, M these Fermi

surfaces can easily be computed, and Fig. 3.3 shows them for 3 different chemical potentials, using the physical pion mass. The chemical potentials in the middle and right panels correspond to the two ends of the CDW region. More exotic topologies are possible – disappearance of one of the Fermi surfaces (red) and split of the (black) Fermi surface into two disconnected regions – but not realized here. Even though the Fermi surfaces are symmetric under $k_{\ell} \rightarrow -k_{\ell}$, there is a nonzero axial current in the vertical direction, to counterbalance that of the mesonic sector. The reason is that the two $s=\pm$ states contribute with opposite sign to that current, at least for q < M, as the integral in the first line of Eq. (C.29) shows. Therefore, for q = 0, where red and black lines would be exactly on top of each other, no net fermionic current exists, while a net current starts to form for q > 0 when the two Fermi surfaces no longer coincide. The case q > M (realized in the right panel) is more complicated, because in this case the s = - state has different regions in momentum space which contribute to the axial current with different sign, which again can be seen from the integrand in Eq. (C.29).

3.3.3 Locating the CDW in the parameter space

Having discussed the details of a specific parameter choice, we now turn to a more systematic exploration of the parameter space of the model. This is necessary due to the large empirical uncertainties in particular of the quantities M_0 , K, and L. Moreover, we have to keep in mind that our model is of phenomenological nature and we can, at best, make qualitative predictions and suggestions for QCD. Therefore, even regions at the edges or beyond the empirically allowed regions, which appear unlikely to be realized from the point of view of our model, may contain interesting features that are possibly relevant for QCD.

The zero-temperature phase structure in the plane spanned by μ and the model parameter M_0 is shown in Fig. 3.4. Let us first discuss the chiral limit (left panel) and focus on the parameters $K=250\,\text{MeV}$, d=50 (black curves). There are 3 qualitatively different scenarios.

3.3. Results 87

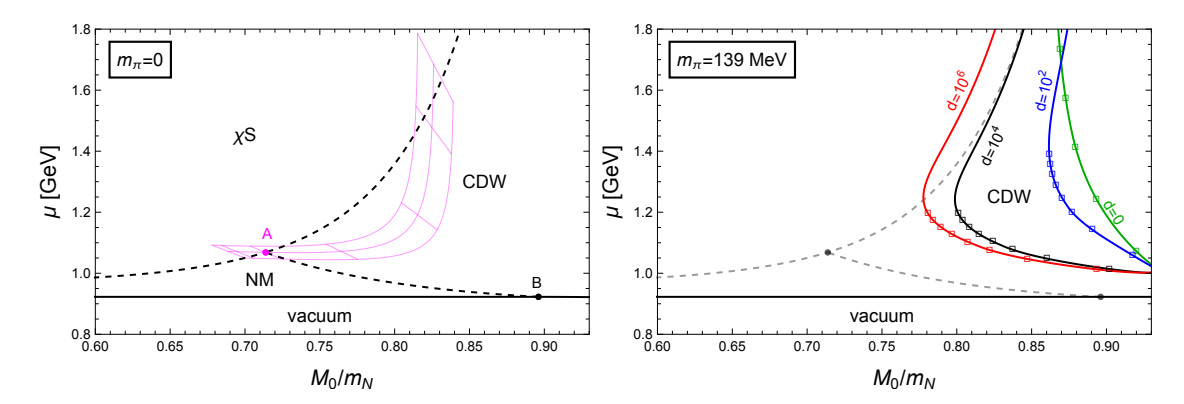


FIGURE 3.4: Left panel: Zero-temperature phases in the chiral limit as the model parameter M_0 is varied, with fixed $K=250\,\mathrm{MeV}$, $d=10^4\,\mathrm{(NM-isotropic nuclear matter}$, $\chi\mathrm{S}$ – isotropic chirally restored phase, CDW – chiral density wave). Black solid (dashed) lines are first (second) order phase transitions. The magenta grid indicates the variation of the triple point A for $K=200,250,300\,\mathrm{MeV}$ (right to left) and $d=0,10^{1,2,3,4,5,6}$ (top to bottom). The triple point B is always at the same μ and varies in M_0 by less than 0.5% as K and d are varied within the range given by the magenta grid. Right panel: Same as left panel, but now for the physical pion mass. The pale black lines are copied from the left panel for reference. Three additional curves (red, blue, green) are shown for three different values of d. The markers on the curves indicate the baryon densities $n_B=(6,8,\ldots,20)n_0$ (from low to high μ) on the isotropic side of the first-order phase transition.

- (*i*) For sufficiently small effective masses at saturation, $M_0 \lesssim 0.71 m_N$, the chiral transition is unaffected by the CDW, there is a second-order transition between isotropic nuclear matter and the isotropic chirally restored phase.
- (ii) For $0.71 \lesssim M_0/m_N \lesssim 0.90$ we find the scenario from Fig. 3.2: There is a finite CDW region covering the would-be isotropic chiral transition.
- (iii) As we approach the point B in the figure, the transition from isotropic nuclear matter to the CDW approaches the nuclear matter onset at μ_0 . For M_0 beyond that point, $M_0 \gtrsim 0.90 m_N$, the model predicts a direct transition from the vacuum to the CDW. This transition occurs at an M_0 -dependent critical chemical potential $\mu < \mu_0$, although on the scale of the plot the corresponding curve is indistinguishable from a horizontal line. Since we know that symmetric nuclear matter at saturation is isotropic, this appears to be an unphysical regime of our model. However, we need to keep in mind that the chiral limit of the left panel is unphysical anyway; and indeed, the right panel shows that this unphysical behavior is gone for the case of a physical pion mass.

How does the CDW region change as we vary the incompressibility *K* and the meson coupling d? As a measure for the importance of the CDW we consider the range in M_0 between the points A and B, read off of the magenta grid (the point B is essentially constant under the variations considered here). We vary K within its empirically most likely range $K \simeq (200 - 300)$ MeV and the quartic meson coupling $d = 0 - 10^6$. For a connection to real-world quantities it is useful to translate the value of *d* into the resulting slope parameter of the symmetry energy *L* and also consider the corresponding sigma mass m_{σ} . This translation is shown in Fig. D.1 in Appendix D. We read off for instance that for $K = 250 \,\text{MeV}$ and tracking the location of point A as $d=0-10^6$, we obtain a range of $L\simeq (87-52)\,\mathrm{MeV}$ and $m_\sigma\simeq (720-830)\,\mathrm{MeV}$. The magenta grid thus illustrates for instance that the CDW becomes more important for increasing *K* or increasing *d* (decreasing *L*). Fig. D.1 also relates the model parameters to the leading-order behavior of the potential $\tilde{U}(\phi)$ for large ϕ . This is interesting because it checks the boundedness of the potential. Although there is no obvious artifact in our results if the potential is unbounded it is useful to point out that this does occur for small values of d and not too large values of M_0 , see left panel of Fig. D.1. Unboundedness of the scalar potential after including the Dirac sea was also observed in quark-meson models [55, 181]; there, however, affecting the entire parameter space due to the different form of the tree-level potential.

The right panel of Fig. 3.4 shows the case of a physical pion mass. Let us first compare the pale black curves (chiral limit, taken from the left panel) with the bold black curve (physical pion mass). First of all, we see that the second-order chiral phase transition line between the isotropic NM and χ S phases disappears as the pion mass is switched on. This indicates that there is no strict distinction between nuclear matter and the chirally restored phase and a crossover is realized, as already discussed in Sec. 3.3.1. The CDW region is bounded by a first-order transition and it has retreated significantly compared to the second-order lines. This is in accordance with the observation of Fig. 3.2, where we have seen that the explicit chiral symmetry breaking tends to disfavor the CDW. With the most likely empirical range $M_0 = (0.7 - 0.8)m_N$ in mind, we see from the black curve that the CDW may just about be realized, if M_0 is on the upper end of this range. Again, it is useful to consult Fig. D.1 to get an idea of the corresponding values of L and m_σ . For instance, for $M_0 = 0.81m_N$ (the case used in Sec. 3.3.2) we have $L \simeq 54\,\text{MeV}$ and $m_\sigma \simeq 1.1\,\text{GeV}$, which is in tension with the

3.3. Results 89

empirically expected value of the sigma mass if the sigma is identified with the $f_0(500)$. The curves for different vector meson couplings (red, green blue) show that the CDW becomes more relevant for larger d, as already anticipated from the chiral limit in the left panel. Larger values of d correspond to smaller L, well within experimental boundaries (perhaps even closer to the real-world value, judging from the distribution of experimental results), but also to larger values of the sigma mass.

Additionally, the plot indicates that the CDW can only appear at large baryon densities (markers on the CDW transition curves). The lowest possible densities are about $n_B \sim 6n_0$, and these are only realized for large, perhaps unrealistically large, M_0 . (Recall that M_0 has an upper bound (3.40), slightly above the scale shown here; as this bound is approached, g_ω goes to zero, which decreases the sensitivity of the results on ω and thus on d.) More realistic values of M_0 require increased values of d, leading to even higher baryon densities for the CDW onset. We have checked that large d generally induce high densities at moderate values of the chemical potential. These large number susceptibilities suggest that the parameter regions where our model predicts a CDW produce soft equations of state. Therefore, it is possible that in these parameter regions the model predicts maximum masses of neutron stars incompatible with astrophysical observations. This remains to be verified by computing the mass-radius curve under neutron star conditions, going beyond the isospin-symmetric scenario considered here.

3.3.4 Comparison with different approaches to the Dirac sea

Finally, let us compare our findings with two different treatments of the Dirac sea: firstly, in the left panel of Fig. 3.5, the use of a different renormalization scale and, secondly, in the right panel, neglecting the Dirac sea partially or altogether. Both comparisons are useful to relate our work to previous studies and are relevant to future improvements in different models.

In Refs. [54, 55] it was pointed out that in the NJL model and in particular the renormalizable quark-meson model, there is a curious behavior at large chemical potentials if the Dirac sea is taken into account: Depending on the parameters of the model, a re-entrance to the CDW phase can occur and this CDW "island" ends at an unphysical boundary. Here, "unphysical" means that the CDW solution turns around

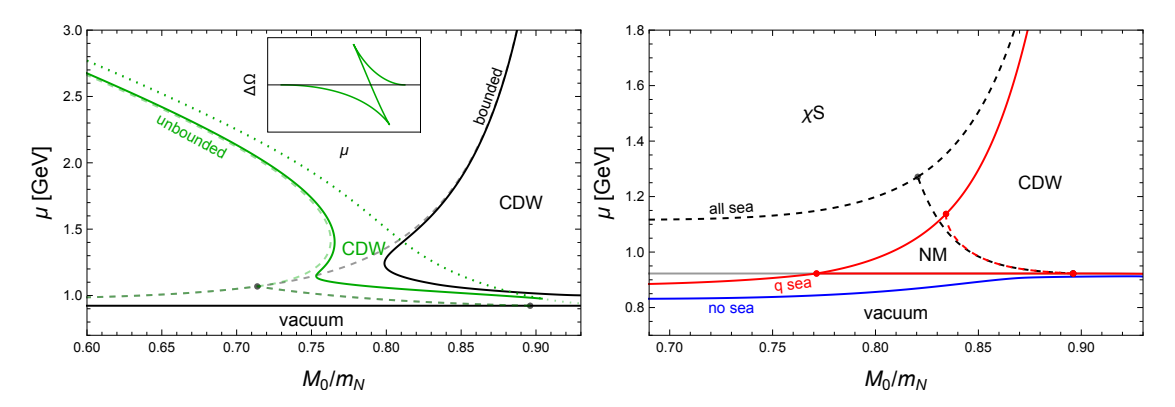


FIGURE 3.5: Comparison of our results to other approaches regarding the nucleonic vacuum contribution, in the plane of the model parameter M_0 and the chemical potential μ . In both panels $K = 250 \,\text{MeV}$, while $d = 10^4 \,\text{(left)} \,d = 50 \,\text{(right)}$. Left *panel*: Results for the choice of the scale $\ell = m_N$, leading to an unbounded free energy (green), compared to our choice in Eq. (3.32) (black, copied from the right panel of Fig. 3.4). Pale lines in both colors correspond to the chiral limit, bold lines to the physical pion mass. The inset shows the unphysical behavior in the free energy difference to the isotropic phase $\Delta\Omega$ for the unbounded case. The dotted lines (pale and bold lines essentially on top of each other) correspond to the point where $\Delta\Omega$ is minimal. *Right* panel: Effect of the Dirac sea in the chiral limit. The full calculation ("all sea") is shown in black. The red curves are obtained by dropping the q = 0 contributions to the Dirac sea ("q sea"). If the entire Dirac sea contribution is dropped ("no sea") the only transition is from the vacuum directly to the CDW phase (blue line), and the CDW persists for arbitrarily large μ . In this panel, the two cases that include the Dirac sea are computed with the renormalization scale from Eq. (3.32) (this choice is only relevant for the CDW- χ S transitions, where q > 0). In both panels, solid (dashed) lines are first (second) order phase transitions.

and continues back to smaller chemical potentials at a point where it is the favored phase. This predicts an unphysical jump in the free energy from the CDW to the chirally restored phase, see inset in the left panel of Fig. 3.5. This panel demonstrates that we find exactly the same behavior if the renormalization scale is chosen to be $\ell = m_N$ rather than choosing the q-dependent scale (3.32): For $\ell = m_N$ (green curves) there are various different scenarios, depending on the value of the model parameter M_0 , but in each case the CDW phase has an upper unphysical boundary (dotted line) as just described. (At very large M_0 there is no CDW region at all for a physical pion mass and $\ell = m_N$.)

It is not surprising that the renormalization scale plays a crucial role here: Our choice, as argued at the end of Sec. 3.2.3, was motivated by avoiding unboundedness of the free energy in the q-direction. This unboundedness, in turn, was identified as a problem in Refs. [55, 177] (but not fixed by a suitable renormalization scheme), and it was realized in Ref. [55] that the unboundedness contributes to the unphysical

3.3. Results 91

behavior, here shown by the green curves. Due to the close similarity between the quark-meson model and our nucleon-meson model, our results suggest that the same renormalization procedure can remove the artifact in the quark-meson model.

As mentioned already in Sec. 3.2.3, the scale ℓ can be chosen differently while still maintaining a bounded free energy. For instance, we can generalize $\ell = \sqrt{m_N^2 + (2cq)^2}$, with a numerical factor c, which has a lower limit $c = 1/\exp(1+2\pi^2/g_\sigma^2) \simeq 0.30$ if boundedness is required and, as $c \to 0$, connects our results continuously to the case $\ell = m_N$. In this work, we do, for definiteness, not further explore the dependence of our results with respect to such variations. It should therefore be kept in mind that the phase boundaries of the CDW phase acquire some uncertainty in our scheme, which becomes larger for larger values of q (corresponding to large μ), and which may be alleviated by more elaborate approximations beyond the mean-field approach.

Turning to the second aspect of this section, we now compare our results to the no-sea approximation, which was used in all previous works on the CDW in nucleonic models. This comparison is done in the right panel of Fig. 3.5. For convenience, we perform this comparison in the chiral limit because in this case all transitions are clearly visible as phase transition lines, crossovers being excluded. We distinguish two different approximations. The red curves are obtained by dropping only the q=0 sea contribution. This amounts to setting $\tilde{U}=U$, i.e., dropping the difference between \tilde{U} and U in Eq. (3.26a), but keeping all terms in $\Delta \tilde{U}$ (3.26b). This approximation, labeled by "q sea" in Fig. 3.5, is reminiscent of the one used in Ref. [98], where rotational symmetry is broken by an external magnetic field B instead of the CDW and it was argued that the B-dependent vacuum contribution contains all important physics, while the B=0 vacuum contribution can be ignored without changing the results qualitatively. We have already seen that if we are interested in the chiral phase transition (which was not relevant in Ref. [98]), already the isotropic calculation is affected by the Dirac sea, turning the first-order chiral transition into a crossover.

Nevertheless, in Fig. 3.5 we see that the q-sea approximation reproduces many of the features of the full result. In contrast, if the entire sea contribution is omitted, $\tilde{U} = U$ and $\Delta \tilde{U} = \Delta U$, the result changes dramatically (blue curve). In that case, the behavior is qualitatively the same for all values of M_0 : there is a first-order transition

from the vacuum to the CDW, and the CDW persists for all values of the chemical potential, i.e., all isotropic phases with nonzero baryon number are gone. If we repeat the calculation for a physical pion mass (not shown in the plot) we find a parameter region, $0.87 \lesssim M_0/m_N \lesssim 0.93$, where the blue line moves above the baryon onset at $\mu = \mu_0$, opening up a pocket of isotropic nuclear matter. This is the scenario (vacuum \rightarrow nuclear matter \rightarrow CDW) found in Ref. [67] in a similar model within the no-sea approximation, investigating only one specific parameter set. With our more global view of the parameter space we conclude that the no-sea approximation vastly overestimates the importance of the CDW, while the q-sea approximation is much closer to the full result, which takes into account the entire nucleonic vacuum contribution.

3.4 Summary

We have employed a nucleon-meson model to improve earlier studies on the possibility of an anisotropic chiral condensate in dense, isospin-symmetric nuclear matter. The model is based on nucleonic degrees of freedom which interact via meson exchange. Importantly, the fermion masses are generated dynamically such that the model can be used to study the chiral phase transition. In our ansatz for the anisotropic chiral condensate we have restricted ourselves to the CDW, which does not break translational invariance. We have worked at zero temperature and in the mean-field approximation.

An important part of our study has been the nucleonic vacuum contribution. We have argued that this contribution is already crucial in the isotropic scenario: it turns the first-order chiral transition into a crossover. As a consequence, our main results concern the question whether the CDW disrupts the smooth transition from nuclear matter to approximately chirally restored matter. We have found that this is indeed possible and have discussed the dependence of the CDW region on the model parameters. By studying the chiral limit as well as the case of a physical pion mass, we have shown that the CDW tends to be disfavored by explicit chiral symmetry breaking. Independent of the choice of the parameters, we have found that within our model the CDW can only appear at large baryon densities, $n_B \gtrsim 6n_0$. It is realized

3.4. Summary 93

somewhere at the edges of and beyond the parameter regime empirically allowed by nuclear saturation properties.

On a more theoretical note, we have discussed a renormalization scheme, and in particular a certain choice of the renormalization scale, which fixes a problem pointed out in similar models based on quark degrees of freedom. Within our scheme, there is no re-entrance and/or unphysical behavior of the CDW at ultra-high densities and it would be interesting to apply our scheme – possibly in modified or further improved form – also to different phenomenological or effective models that describe the CDW or related non-uniform phases.

Chapter 4

Conclusion and Outlook

In our work, we have set up two variations of a nucleon meson model. The aim of the first was to explore whether the properties of the chirally restored phase of the model could be tuned to recreate quark matter properties, while at the same time to be able to accommodate neutron stars consistent with current observational constraints. We achieved to set up such a scenario, and used our model to draw conclusions about the chiral phase transition. First, the model predicts that the chiral phase transition is of first order at vanishing temperature. Moreover, the location of the transition is preferred to be at relatively small μ_B , so that neutron stars can have a large and stiff chirally restored inner core. Such a configuration might be crucial to explain the heavier compact objects that we can see today (that are not black holes). Second, we pointed out that the hyperon onset is delayed up until after the chiral phase transition. In the context of the "hyperon puzzle", one could avoid the softening of the equation of state by an early transition to a stiff, chirally restored phase, without ever introducing baryons beyond the nucleons in the system. Could this also be happening in QCD? Finally, in view of the small region that our model restricts the slope parameter *L*, one may wonder whether an extensive survey of different phenomenological models could provide some indication about the value of this or of other poorly constrained properties of dense matter.

In our second work we restricted ourselves to isospin symmetric matter and removed the hyperons from the model. However, we included the Dirac sea contribution of the nucleons, which had a significant impact on the nature of the phase

transition, converting it to a crossover. This sheds a new light on the importance of the Dirac sea, and directly questions the no-sea approximation in similar models. The quark-hadron continuity proposal is also rekindled here, since there is no strict separation between our chirally restored and broken phase. Another takeaway is that maybe inhomogeneous phases should not only be considered in the vicinity of phase transitions, since even the (relatively "fast") smooth crossover is disrupted by the appearance of the CDW. Finally, it is very likely that the CDW will not appear within neutron stars. Even though we have not performed calculations enforcing the beta-equilibrium and charge neutrality conditions, we do not expect them to significantly alter this conclusion. The density that CDW has an onset is very high if we stay within the empirical range of the physical parameters.

The qualitatively significant contribution of the sea term discussed in Chapter 3 has implications for the further development of the ideas presented in Chapter 2. First, it will be useful to explore what is the effect of beta equilibrium, charge neutrality and hyperon onset in the stability of the CDW. Second, due to the disappearance of the first order phase transition, a softening is expected in the equation of state. Consequently, the parameter region where the existence of heavy enough compact stars is predicted will be shifted. These are points to consider if one wants to answer whether a layer of the CDW is possible to form within the neutron star core. In this context one may also study the competition or possible coexistence of the CDW with quark-hadron mixed phases, which become conceivable due to the presence of a second chemical potential associated with electric charge. Combining and extending ideas in the two works, it would be interesting to include the strange component of the chiral condensate $\zeta \propto \langle \bar{s}s \rangle$. Not only would this more accurately represent the chiral condensate in the model, but it would enable us to explore the possibility of a "strangeness" CDW instead of, or along with the ordinary CDW. One could also consider an improved ansatz for the anisotropic chiral condensate, possibly comparing it with different inhomogeneous structures.

So far, we have also restricted ourselves to zero temperature, and extensions to finite temperatures, desirably going beyond the mean-field approximation, would be interesting and relevant for applications to the mergers of compact stars in the presence of a quark-hadron transition [182, 183].

Another direction is trying to perform these calculations in alternative nucleon-meson models. That could be including strange baryonic degrees of freedom (and their chiral partners) into the extended linear sigma model of Refs. [67, 184, 185], along the lines of Ref. [1] or [186]. The CDW has been studied in this model [67], but without the effect of the Dirac sea.

We have also noted that the ground state of QCD at sufficiently low temperatures is expected to have a superfluid component, possibly on both sides of the chiral phase transition. However, in our model we have not included such a construction. It is conceivable to include Cooper pairing, both in the chirally broken and the chirally restored phases, and it would be interesting to see whether a version of the color-flavor locked phase at high densities [38, 42] can be constructed. It would then be possible to compute for instance the surface tension in the presence of Cooper pairing consistently within a single model. Or, considering the case of a crossover, the model might be able to provide a realization of the quark-hadron continuity in the sense suggested by Ref. [26].

Observable signatures of an inhomogeneous phase can come from the modified transport properties, even if equilibrium properties like the equation of state are only weakly affected. Bulk viscosity in particular, can be important for neutron star merger simulations, since it introduces energy dissipation. In the presence of an inhomogeneous phase, bulk viscosity is modified, as the phase space of the particles is getting deformed. If this modification is significant, it can alter the conclusions of analyses like [187]. When simulating a merger, it is necessary to answer whether the bulk viscosity generated in the presence of an inhomogeneous phase, dampens density oscillations in a timescale relevant for the simulation. Such an effect may also have a significant impact on the energy dissipation during the inspiral, via tidal heating.

Another interesting question is "how would a realistic CDW phase look when it forms within a star?" The usual, simplistic picture is that of a uniform phase. However, given how the system evolves to create this phase, this is not a very probable picture. As the neutron star cools down we expect it to go through a phase transition from a homogeneous to the CDW phase. Assuming that there is no preferred direction, each point in space is going to transition to the CDW phase, with

the wave-vector of the modulation aligned along a random direction. As a result, the full volume of the space will be divided into randomly aligned domains, similar to the demagnetized phase of a ferromagnetic material. It would be interesting to calculate the typical size of these domains, as well as the possibility of alignment under the influence of a magnetic field or rotation.

Finally, our setup can be used for studying a possible quarkyonic phase, which has been predicted to occur in QCD at a large number of colors N_c and may survive for $N_c = 3$ [188]. This phase was for instance constructed in a model that includes both quark and hadronic degrees of freedom [189] (besides other approaches [96, 160, 190]). It would be interesting to see whether our more unified approach might be able to show a transition from baryonic through quarkyonic to quark matter.

Appendix A

Chiral setup

In this appendix we review the foundations of our model within the framework of an $SU(3) \times SU(3)$ chiral approach. This discussion makes explicit which mesonic degrees of freedom we have omitted and which assumptions we have made for the structure of the interaction terms, which is useful to keep in mind for potential extensions in the future. It also provides relations between the baryon-meson coupling constants, some of which we employ in the main part, besides guidance from phenomenology to fix them. Our baryonic degrees of freedom are usually parametrized in the baryon octet as

$$B = \begin{pmatrix} \frac{\Sigma^{0}}{\sqrt{2}} + \frac{\Lambda}{\sqrt{6}} & \Sigma^{+} & p \\ \Sigma^{-} & -\frac{\Sigma^{0}}{\sqrt{2}} + \frac{\Lambda}{\sqrt{6}} & n \\ \Xi^{-} & \Xi^{0} & -\sqrt{\frac{2}{3}}\Lambda \end{pmatrix}, \tag{A.1}$$

and the kinetic part of the baryonic Lagrangian can be written as $\text{Tr}[\bar{B}i\gamma^{\mu}\partial_{\mu}B]$. The scalar and pseudoscalar meson nonets are summarized in the field $\Phi = S + iP = T_a(\sigma_a + i\pi_a)$, where $T_a = \lambda_a/2$ for $a = 0, \ldots, 8$, with the Gell-Mann

matrices λ_a for $a=1,\ldots,8$ and $\lambda_0=\sqrt{2/3}\,\mathbf{1}$. This is usually reparametrized as

$$S = T_{a}\sigma_{a} = \frac{1}{\sqrt{2}} \begin{pmatrix} \frac{a_{0}^{0}}{\sqrt{2}} + \frac{\sigma_{8}}{\sqrt{6}} + \frac{\sigma_{0}}{\sqrt{3}} & a_{0}^{+} & \kappa^{+} \\ a_{0}^{-} & -\frac{a_{0}^{0}}{\sqrt{2}} + \frac{\sigma_{8}}{\sqrt{6}} + \frac{\sigma_{0}}{\sqrt{3}} & \kappa^{0} \\ \kappa^{-} & \bar{\kappa}^{0} & -\sqrt{\frac{2}{3}}\sigma_{8} + \frac{\sigma_{0}}{\sqrt{3}} \end{pmatrix}$$
(A.2a)

$$P = T_a \pi_a = \frac{1}{\sqrt{2}} \begin{pmatrix} \frac{\pi^0}{\sqrt{2}} + \frac{\pi_8}{\sqrt{6}} + \frac{\pi_0}{\sqrt{3}} & \pi^+ & K^+ \\ \pi^- & -\frac{\pi^0}{\sqrt{2}} + \frac{\pi_8}{\sqrt{6}} + \frac{\pi_0}{\sqrt{3}} & K^0 \\ K^- & \bar{K}^0 & -\sqrt{\frac{2}{3}} \pi_8 + \frac{\pi_0}{\sqrt{3}} \end{pmatrix}$$
(A.2b)

One may now construct the potential up to a given order in Φ systematically. For instance, up to fourth order [110],

$$U(\Phi) = m^2 \text{Tr}[\Phi^{\dagger}\Phi] + \lambda_1 (\text{Tr}[\Phi^{\dagger}\Phi])^2 + \lambda_2 \text{Tr}[(\Phi^{\dagger}\Phi)^2] -$$

$$c(\det \Phi^{\dagger} + \det \Phi) - \text{Tr}[H(\Phi^{\dagger} + \Phi)], \qquad (A.3)$$

with parameters m^2 , λ_1 , λ_2 for the quadratic and quartic contributions, c for the chiral anomaly term and a matrix H for a small explicit symmetry breaking. In the scalar sector, one can trade σ_0 and σ_8 for non-strange and strange scalar fields by the transformation

$$\begin{pmatrix} \sigma \\ \zeta \end{pmatrix} = \frac{1}{\sqrt{3}} \begin{pmatrix} \sqrt{2} & 1 \\ 1 & -\sqrt{2} \end{pmatrix} \begin{pmatrix} \sigma_0 \\ \sigma_8 \end{pmatrix}. \tag{A.4}$$

Omitting all other scalar fields results in $S = \frac{1}{2} \operatorname{diag}(\sigma, \sigma, \sqrt{2}\zeta)$. As explained in the main text we further simplify this by omitting the scalar field ζ . The pseudoscalar nonet P is not directly relevant because we assume none of these fields to condense, and our mean-field approach ignores the fluctuations. It is only indirectly used by fitting one of the parameters of the meson potential (2.7) to the pion mass. Our potential thus effectively only depends on σ , which is a drastic simplification of the full potential (A.3). However, we have included terms of higher order than 4 in σ , to make the connection with the previous (non-strange) version of our baryon-meson model [49, 97].

The vector meson nonet can be parametrized as

$$V_{\mu} = T_{a}\omega_{\mu}^{a} = \frac{1}{\sqrt{2}} \begin{pmatrix} \frac{\rho_{\mu}^{0}}{\sqrt{2}} + \frac{\omega_{\mu}}{\sqrt{2}} & \rho_{\mu}^{+} & K_{\mu}^{*+} \\ \rho_{\mu}^{-} & -\frac{\rho_{\mu}^{0}}{\sqrt{2}} + \frac{\omega_{\mu}}{\sqrt{2}} & K_{\mu}^{*0} \\ K_{\mu}^{*-} & \bar{K}_{\mu}^{*0} & \phi_{\mu} \end{pmatrix}, \tag{A.5}$$

where ω_{μ} and ϕ_{μ} are defined by the same transformation as used in Eq. (A.4) for the scalar mesons,

$$\begin{pmatrix} \omega_{\mu} \\ \phi_{\mu} \end{pmatrix} = \frac{1}{\sqrt{3}} \begin{pmatrix} \sqrt{2} & 1 \\ 1 & -\sqrt{2} \end{pmatrix} \begin{pmatrix} \omega_{\mu}^{0} \\ \omega_{\mu}^{8} \end{pmatrix}. \tag{A.6}$$

Keeping only the fields ω_{μ} , ϕ_{μ} , ρ_{μ}^{0} , the matrix V_{μ} becomes diagonal, and we can write down the two quartic structures

$$d_{1}(\text{Tr}[V_{\mu}V^{\mu}])^{2} + d_{2}\text{Tr}[(V_{\mu}V^{\mu})^{2}] = \frac{d_{1}}{4}(\omega_{\mu}\omega^{\mu} + \rho_{\mu}^{0}\rho_{0}^{\mu} + \phi_{\mu}\phi^{\mu})^{2} + \frac{d_{2}}{8}\left[(\omega_{\mu}\omega^{\mu})^{2} + (\rho_{\mu}^{0}\rho_{0}^{\mu})^{2} + 6\omega_{\mu}\omega^{\mu}\rho_{\nu}^{0}\rho_{0}^{\nu}\right]. \quad (A.7)$$

In the main text we work for simplicity with $d_2 = 0$ (and denote $d = d_1$). For a more complete study of vector meson self-interactions in a chiral approach, including axial-vector mesons and derivative interactions with three meson fields, see for instance Refs. [191, 192].

Next, let us discuss the baryon-meson interactions. For the scalar sector, and temporarily including the ζ field, the chirally invariant structures are

$$A_{1}\text{Tr}[\bar{B}SB] + A_{2}\text{Tr}[\bar{B}BS] + A_{3}\text{Tr}[\bar{B}B]\text{Tr}[S]$$

$$= g_{N\sigma}(\bar{n}\sigma n + \bar{p}\sigma p) + g_{N\zeta}(\bar{n}\zeta n + \bar{p}\zeta p) + g_{\Sigma\sigma}(\bar{\Sigma}^{0}\sigma\Sigma^{0} + \bar{\Sigma}^{+}\sigma\Sigma^{+} + \bar{\Sigma}^{-}\sigma\Sigma^{-})$$

$$+ g_{\Sigma\zeta}(\bar{\Sigma}^{0}\zeta\Sigma^{0} + \bar{\Sigma}^{+}\zeta\Sigma^{+} + \bar{\Sigma}^{-}\zeta\Sigma^{-})$$

$$+ g_{\Lambda\sigma}\bar{\Lambda}\sigma\Lambda + g_{\Lambda\zeta}\bar{\Lambda}\zeta\Lambda + g_{\Xi\sigma}(\bar{\Xi}^{0}\sigma\Xi^{0} + \bar{\Xi}^{-}\sigma\Xi^{-}) + g_{\Xi\zeta}(\bar{\Xi}^{0}\zeta\Xi^{0} + \bar{\Xi}^{-}\zeta\Xi^{-}). \text{ (A.8)}$$

We have introduced 8 coupling constants, which all are linear combinations the 3 independent parameters A_1 , A_2 , A_3 . Therefore, one can choose 3 independent

couplings, and the chiral structure fixes the other 5. In our approximation, where we omit the ζ , we have 4 coupling constants and thus, if we wanted to respect the structure given by chiral symmetry, we can choose three of them freely, say $g_{N\sigma}$, $g_{\Sigma\sigma}$, $g_{\Lambda\sigma}$. For the remaining coupling constant this yields the constraint

$$g_{\Xi\sigma} = \frac{3g_{\Lambda\sigma} - 2g_{N\sigma} + g_{\Sigma\sigma}}{2}.$$
 (A.9)

In the main part we fix all four coupling constants separately with the help of the vacuum masses, such that this relation is (slightly) violated in our phenomenological approach: with $g_{N\sigma}=10.16$, $g_{\Lambda\sigma}=12.07$, $g_{\Sigma\sigma}=12.88$, the relation (A.9) would yield $g_{\Xi\sigma}=14.38$, while our fit gives $g_{\Xi\sigma}=14.23$.

Finally, for the interactions with the vector mesons, keeping only the fields ω , ρ^0 , and ϕ , we find the structure

$$C_{1}\text{Tr}[\bar{B}\gamma^{\mu}V_{\mu}B] + C_{2}\text{Tr}[\bar{B}\gamma^{\mu}BV_{\mu}] + C_{3}\text{Tr}[\bar{B}\gamma^{\mu}B]\text{Tr}[V_{\mu}]$$

$$= g_{N\omega}(\bar{n}\gamma^{\mu}\omega_{\mu}n + \bar{p}\gamma^{\mu}\omega_{\mu}p) + g_{N\phi}(\bar{n}\gamma^{\mu}\phi_{\mu}n + \bar{p}\gamma^{\mu}\phi_{\mu}p) + g_{N\rho}(\bar{n}\gamma^{\mu}\rho_{\mu}^{0}n - \bar{p}\gamma^{\mu}\rho_{\mu}^{0}p)$$

$$+ g_{\Sigma\omega}(\bar{\Sigma}^{0}\gamma^{\mu}\omega_{\mu}\Sigma^{0} + \bar{\Sigma}^{+}\gamma^{\mu}\omega_{\mu}\Sigma^{+} + \bar{\Sigma}^{-}\gamma^{\mu}\omega_{\mu}\Sigma^{-})$$

$$+ g_{\Sigma\phi}(\bar{\Sigma}^{0}\gamma^{\mu}\phi_{\mu}\Sigma^{0} + \bar{\Sigma}^{+}\gamma^{\mu}\phi_{\mu}\Sigma^{+} + \bar{\Sigma}^{-}\gamma^{\mu}\phi_{\mu}\Sigma^{-})$$

$$+ g_{\Sigma\rho}(\bar{\Sigma}^{+}\gamma^{\mu}\rho_{\mu}^{0}\Sigma^{+} - \bar{\Sigma}^{-}\gamma^{\mu}\rho_{\mu}^{0}\Sigma^{-}) + g_{\Lambda\omega}\bar{\Lambda}\gamma^{\mu}\omega_{\mu}\Lambda + g_{\Lambda\phi}\bar{\Lambda}\gamma^{\mu}\phi_{\mu}\Lambda$$

$$+ g_{\Xi\omega}(\bar{\Xi}^{0}\gamma^{\mu}\omega_{\mu}\Xi^{0} + \bar{\Xi}^{-}\gamma^{\mu}\omega_{\mu}\Xi^{-}) + g_{\Xi\phi}(\bar{\Xi}^{0}\gamma^{\mu}\phi_{\mu}\Xi^{0} + \bar{\Xi}^{-}\gamma^{\mu}\phi_{\mu}\Xi^{-})$$

$$+ g_{\Xi\rho}(\bar{\Xi}^{0}\gamma^{\mu}\rho_{\mu}^{0}\Xi^{0} - \bar{\Xi}^{-}\gamma^{\mu}\rho_{\mu}^{0}\Xi^{-}). \tag{A.10}$$

Here, the 11 couplings are linear combinations of the 3 independent coefficients C_1 , C_2 , C_3 . Equivalently, we may write C_1 , C_2 , C_3 in terms of 3 coupling constants, say the 3 nucleonic couplings $g_{N\omega}$, $g_{N\phi}$, $g_{N\phi}$, and express the remaining 8 hyperonic

couplings as

$$g_{\Sigma\omega} = \frac{g_{N\omega} + \sqrt{2}g_{N\phi} - g_{N\rho}}{2}, \qquad g_{\Lambda\omega} = \frac{5g_{N\omega} + \sqrt{2}g_{N\phi} + 3g_{N\rho}}{6},$$

$$g_{\Xi\omega} = \frac{g_{N\omega} + \sqrt{2}g_{N\phi} + g_{N\rho}}{2},$$

$$g_{\Sigma\rho} = \frac{g_{N\omega} - \sqrt{2}g_{N\phi} - g_{N\rho}}{2}, \qquad g_{\Xi\rho} = \frac{g_{N\omega} - \sqrt{2}g_{N\phi} + g_{N\rho}}{2},$$

$$g_{\Sigma\phi} = \frac{g_{N\omega} + g_{N\rho}}{\sqrt{2}}, \qquad g_{\Lambda\phi} = \frac{\sqrt{2}g_{N\omega} + 4g_{N\phi} - 3\sqrt{2}g_{N\rho}}{6},$$

$$g_{\Xi\phi} = \frac{g_{N\omega} - g_{N\rho}}{\sqrt{2}}.$$
(A.11)

A particular choice for the independent coupling constants is $g_{N\phi}=0$ and $g_{N\rho}=-\frac{g_{N\omega}}{3}$. This yields the following relations,

$$g_{\Sigma\omega} = g_{\Lambda\omega} = 2g_{\Xi\omega} = \frac{2}{3}g_{N\omega}, \qquad g_{\Sigma\rho} = 2g_{\Xi\rho} = -2g_{N\rho},$$

$$g_{\Sigma\phi} = g_{\Lambda\phi} = \frac{g_{\Xi\phi}}{2} = \frac{\sqrt{2}}{3}g_{N\omega}. \tag{A.12}$$

These relations are often employed in the literature, see for instance Ref. [111] and references therein (our sign convention for the ρ and ϕ couplings is different compared to that reference). Also following the literature, we then fit $g_{N\omega}$ and $g_{N\rho}$ to reproduce saturation properties of nuclear matter, as explained in the main text. This violates the relation $g_{N\rho}=-\frac{g_{N\omega}}{3}$. Since this relation was used to derive Eqs. (A.12) this procedure also violates the original chiral relations (A.11). Furthermore, we relate the ω couplings to the hyperon potential depths, ignoring the first relation of Eq. (A.12). For example, for one of the parameter sets used in Sec. 2.4.1 we have $g_{N\omega}=10.23$, $g_{N\rho}=4.14$. With the first line of Eqs. (A.11) this would yield $g_{\Sigma\omega}=3.05$, $g_{\Lambda\omega}=10.6$, $g_{\Xi\omega}=7.1$, while the fit to the hyperon potential $\mathcal{U}=-50\,\mathrm{MeV}$ (used for all parameter sets in Sec. 2.4.1) gives the larger couplings $g_{\Sigma\omega}=14.6$, $g_{\Lambda\omega}=14.5$, $g_{\Xi\omega}=16.4$, see also Table D.1. For the ρ and ϕ couplings we employ the relations in Eqs. (A.12).

Appendix B

Asymptotic flavor symmetry

In asymptotically dense three-flavor QCD, quark matter with equal numbers of up, down, and strange quarks is electrically neutral and beta-equilibrated. In this appendix we ask whether our model can reproduce this symmetric situation, i.e., whether there is a certain choice of parameters such that our chirally restored phase shares this property with actual quark matter. To this end, we first define the up, down, and strange number densities according to the flavor content of the baryons,

$$n_u = n_n + 2n_p + n_{\Sigma^0} + 2n_{\Sigma^+} + n_{\Lambda} + n_{\Xi^0},$$
 (B.1a)

$$n_d = 2n_n + n_v + n_{\Sigma^0} + 2n_{\Sigma^-} + n_{\Lambda} + n_{\Xi^-},$$
 (B.1b)

$$n_s = n_{\Sigma^+} + n_{\Sigma^-} + n_{\Sigma^0} + n_{\Lambda} + 2(n_{\Xi^-} + n_{\Xi^0}).$$
 (B.1c)

The condition $n_u = n_d$ together with the neutrality condition (2.21) yields $n_e + n_\mu = 0$. The solution of the stationarity equations thus has to be consistent with μ_e going to zero asymptotically. As an ansatz let us assume the following asymptotic behaviors for $\mu_n \to \infty$,

$$\mu_e \simeq \frac{\mu_{e,\infty}}{\mu_n}$$
, $\sigma \simeq \frac{\sigma_\infty}{\mu_n^2}$, $\omega \simeq \omega_\infty \mu_n$, $\phi \simeq \phi_\infty \mu_n$, $\rho \simeq \frac{\rho_\infty}{\mu_n}$, (B.2)

with coefficients $\mu_{e,\infty}$, σ_{∞} , ω_{∞} , ϕ_{∞} , ρ_{∞} constant in the neutron chemical potential. We shall see that this ansatz indeed leads to a valid solution of the stationarity equations, which can also be confirmed numerically. In the neutrality equation (2.21), the only

	solution 1	solution 2	solution 3	
8Σφ	$g_{N\phi} + a(g_{N\omega} - g_{\Sigma\omega})$	$g_{N\phi}+a(g_{N\omega}-g_{\Sigma\omega})$	$\frac{a^2+1}{4a}g_{\Lambda\omega} - \frac{a^2-3}{4a}g_{\Sigma\omega}$	
8 Λφ	$g_{N\phi}+a(g_{N\omega}-g_{\Lambda\omega})$	$\frac{g_{\Lambda\omega}}{a}$	$-\frac{3a^2-1}{4a}g_{\Lambda\omega}+\frac{3(a^2+1)}{4a}g_{\Sigma\omega}$	
<i>8</i> Ξφ	$-\frac{3a^2-1}{a^2+1}g_{N\phi}-2a\frac{a^2-1}{a^2+1}g_{N\omega}+a\frac{3g_{\Sigma\omega}+g_{\Lambda\omega}}{2}$	$-\frac{5a^2-2}{2(a^2+1)}g_{N\phi}-a\frac{3a^2-4}{2(a^2+1)}g_{N\omega}+\frac{3a}{2}g_{\Sigma\omega}$	$-\frac{a^2 - 1}{a^2 + 1}g_{N\phi} + \frac{2a}{a^2 + 1}g_{N\omega}$	
8Ξω	$\frac{4a}{a^2 + 1} g_{N\phi} + \frac{3a^2 - 1}{a^2 + 1} g_{N\omega} - \frac{3g_{\Sigma\omega} + g_{\Lambda\omega}}{2}$	$\frac{7a}{2(a^2+1)}g_{N\phi} + \frac{5a^2-2}{2(a^2+1)}g_{N\omega} - \frac{3}{2}g_{\Sigma\omega}$	$\frac{2a}{a^2+1}g_{N\phi} + \frac{a^2-1}{a^2+1}g_{N\omega}$	

TABLE B.1: Three sets of conditions for the baryon-meson coupling constants, each leading to equal number densities of the three flavors at asymptotic densities for any value of the constant *a*, reproducing the behavior of asymptotically dense three-flavor QCD. Since none of the solutions seems to allow for sufficiently heavy stars they are not employed in the main part of the thesis.

leading-order contributions proportional to μ_n^3 come from n_p and n_{Ξ^-} . Since the mass terms are of higher order due to σ behaving like $1/\mu_n^2$, this yields the asymptotic condition $\mu_p^* = \mu_{\Xi^-}^*$. Since the ρ condensate also vanishes asymptotically on account of the ansatz (B.2), this immediately gives the relation

$$\omega_{\infty} = \frac{g_{\Xi\phi} - g_{N\phi}}{g_{N\omega} - g_{\Xi\omega}} \phi_{\infty}. \tag{B.3}$$

Now, Eqs. (2.20b) and (2.20d) have leading-order contributions proportional to μ_n^3 which depend only on ω_{∞} and ϕ_{∞} (and none of the other coefficients of the ansatz (B.2)). Together with Eq. (B.3) these are three conditions for the two variables ω_{∞} and ϕ_{∞} . Thus, in order for (B.2) to be a valid solution we require (2.20b) and (2.20d) to give the same condition. This can be translated into conditions for the coupling constants as follows: we insert Eq. (B.3) into the leading-order contribution of Eqs. (2.20b) and (2.20d) to eliminate ω_{∞} . Then, we require the four coefficients of the powers ϕ_{∞}^0 , ϕ_{∞}^1 , ϕ_{∞}^2 , ϕ_{∞}^3 of the two equations to be identical up to a constant, say a, to find four conditions for the coupling constants. In fact, there are three possible solutions, i.e., three sets of four conditions, which we show in Table B.1. As a consistency check, one can ask whether we recover the chiral relations (A.11), which we would expect to reproduce flavor-symmetric matter. Indeed, solution 1 with $a = \sqrt{2}$ is satisfied by the chiral relations (A.11). The inverse is obviously not true: even within solution 1, since it consists of only four conditions, there are choices for the coupling constants that obey solution 1 but not the chiral relations (A.11) (in particular, if we allow for arbitrary values of a). The solutions can be used to compute the corresponding ϕ_{∞} and ω_{∞} . The results are not very instructive, but we have checked that they agree with the

numerical evaluation. Similarly, one can consider the subleading contributions in μ_n to the stationarity equations to compute σ_∞ , $\mu_{\ell,\infty}$, ρ_∞ , but, again, we refrain from showing these results explicitly. The main observation is that there exist choices of the coupling constants, given by the solutions in the table, for which at asymptotically large densities $n_u = n_d = n_s$, with the flavor densities defined in Eq. (B.1). However, we have not found a parameter set within the constraints of Table B.1 which simultaneously fulfills all empirical constraints. Therefore, in the main text we content ourselves with employing parameter sets that do produce asymptotic strangeness, but not in a fraction of 1/3.

Appendix C

Computing the Dirac sea contribution

C.1 Regularization

In order to regularize the divergent part of the baryonic pressure P_{vac} (3.19) we employ proper time regularization. First, we use

$$\frac{1}{x^a} = \frac{1}{\Gamma(a)} \int_0^\infty d\tau \, \tau^{a-1} e^{-\tau x} \tag{C.1}$$

to rewrite E_k^s from Eq. (3.16), setting a=-1/2, $x=(\sqrt{k_\ell^2+M^2}+sq)^2+k_\perp^2$. We can then perform the k_\perp integration to obtain

$$P_{\text{vac}} = -\frac{1}{4\pi^{5/2}} \int_0^\infty \frac{d\tau}{\tau^{5/2}} \int_0^\infty dk_\ell \, e^{-\tau(k_\ell^2 + M^2 + q^2)} \cosh 2q\tau \sqrt{k_\ell^2 + M^2} \,. \tag{C.2}$$

Next, after inserting the series expansion

$$cosh x = \sum_{n=0}^{\infty} \frac{x^{2n}}{(2n)!},$$
(C.3)

we can perform the k_ℓ integral to obtain

$$P_{\text{vac}} = \sum_{n=0}^{\infty} \int_0^{\infty} \frac{\tau^{2n} d\tau}{\tau^{5/2}} \mathcal{P}_n, \qquad (C.4)$$

where

$$\mathcal{P}_n \equiv -\frac{M}{8\pi^2} \frac{(2qM)^{2n}}{(2n)!} e^{-\tau(M^2+q^2)} \Psi\left(\frac{1}{2}, \frac{3}{2} + n, \tau M^2\right), \tag{C.5}$$

with the confluent hypergeometric function of the second kind $\Psi(a,b,z)$.

For small τ we have

$$\frac{\tau^{2n}}{\tau^{5/2}} \Psi\left(\frac{1}{2}, \frac{3}{2} + n, \tau M^2\right) \propto \tau^{n-3}$$
 (C.6)

Therefore, the τ integral is finite for $n \ge 3$. For n = 0, 1, 2 we replace the lower boundary by a cutoff $1/\Lambda^2$ to compute

$$\sum_{n=0}^{2} \int_{1/\Lambda^{2}}^{\infty} \frac{\tau^{2n} d\tau}{\tau^{5/2}} \mathcal{P}_{n} = -\frac{\Lambda^{4}}{16\pi^{2}} + \frac{\Lambda^{2} M^{2}}{8\pi^{2}} + \frac{M^{4}}{16\pi^{2}} \left(\gamma - \frac{3}{2} + \ln \frac{M^{2} + q^{2}}{\Lambda^{2}} \right) + \frac{q^{2} M^{2}}{4\pi^{2}} \left(\gamma + \ln \frac{M^{2} + q^{2}}{\Lambda^{2}} \right) + \frac{q^{4}}{96\pi^{2}} \frac{3 - 8y^{2} - 25y^{4} - 6y^{6}}{(1 + y^{2})^{2}} + \mathcal{O}\left(\frac{1}{\Lambda^{2}}\right), \quad (C.7)$$

where $\gamma \simeq 0.577$ is the Euler-Mascheroni constant and we have used the abbreviation y as defined in Eq. (3.29).

For the terms $n \ge 3$ it is easier to go back to the original expression (C.2), insert the series (C.3), and then first perform the τ integral. With the new integration variables $k'_{\ell} = k_{\ell}/q$, $\tau' = q^2 \tau$, abbreviating

$$\kappa^2 \equiv k_\ell^{\prime 2} + y^2 \,, \tag{C.8}$$

C.2. Renormalization 111

and dropping the primes again for convenience, we compute

$$-\frac{q^4}{4\pi^{5/2}} \int_0^\infty dk_\ell \sum_{n=3}^\infty \frac{(2\kappa)^{2n}}{(2n)!} \int_0^\infty \frac{\tau^{2n} d\tau}{\tau^{5/2}} e^{-\tau(\kappa^2+1)}$$

$$= -\frac{q^4}{4\pi^{5/2}} \int_0^\infty dk_\ell \sum_{n=3}^\infty \frac{\Gamma(2n-3/2)}{(2n)! \sqrt{\pi}} \frac{(2\kappa)^{2n}}{(\kappa^2+1)^{2n-3/2}}$$

$$= -\frac{q^4}{6\pi^2} \int_0^\infty dk_\ell \left[(1+\kappa)^3 + |1-\kappa|^3 - \frac{3\kappa^4 + 12\kappa^2(1+\kappa^2)^2 + 8(1+\kappa^2)^4}{4(1+\kappa^2)^{5/2}} \right]$$

$$= -\left(\frac{M^4}{16\pi^2} + \frac{q^2 M^2}{4\pi^2} \right) \ln \frac{M^2 + q^2}{M^2} + \frac{q^4}{96\pi^2} \frac{5 + 24y^2 + 33y^4 + 6y^6}{(1+y^2)^2}$$

$$+ \frac{q^4 \Theta(1-y)}{4\pi^2} \left[-\sqrt{1-y^2} \frac{2 + 13y^2}{6} + 2y^2 \left(1 + \frac{y^2}{4} \right) \ln \frac{1 + \sqrt{1-y^2}}{y} \right]. \tag{C.9}$$

Adding the results (C.7) and (C.9), we obtain the compact expression

$$P_{\text{vac}} = -\frac{\Lambda^4}{16\pi^2} + \frac{\Lambda^2 M^2}{8\pi^2} + \frac{M^4}{16\pi^2} \left(\gamma - \frac{3}{2} + \ln \frac{M^2}{\Lambda^2} \right) + \frac{q^2 M^2}{4\pi^2} \left(\gamma + \ln \frac{M^2}{\Lambda^2} \right) + \frac{q^4}{4\pi^2} F(y) + \mathcal{O}\left(\frac{1}{\Lambda^2}\right) , \qquad (C.10)$$

with F(y) defined in Eq. (3.28).

C.2 Renormalization

Removing the divergences in Eq. (C.10) requires renormalization. To this end, we first introduce a renormalization scale ℓ and drop the terms of order $1/\Lambda^2$ and higher to rewrite Eq. (C.10) as

$$-2P_{\text{vac}} = \frac{\Lambda^4}{8\pi^2} - \frac{\Lambda^2 M^2}{4\pi^2} - \left(\frac{M^4}{8\pi^2} + \frac{q^2 M^2}{2\pi^2}\right) \left(\gamma - \frac{3}{2} + \ln\frac{\ell^2}{\Lambda^2}\right)$$
$$-\frac{M^4}{8\pi^2} \ln\frac{M^2}{\ell^2} - \frac{q^2 M^2}{2\pi^2} \left(\ln\frac{M^2}{\ell^2} + \frac{3}{2}\right) - \frac{q^4}{2\pi^2} F(y). \tag{C.11}$$

We have also reinstated the isospin degeneracy factor 2 and a minus sign to obtain the total vacuum contribution from neutrons and protons to the free energy, cf. Eq. (3.18).

Next, we interpret the following fields and parameters in the Lagrangian as bare quantities, related to the corresponding renormalized quantities via

$$\phi = Z^{1/2}\phi_r, \quad f_{\pi} = Z^{1/2}f_{\pi,r}, \quad g_{\sigma} = \frac{g_{\sigma,r}}{Z^{1/2}}, \quad a_n = \frac{a_{n,r} + f_{\pi,r}^{4-2n} \delta a_n}{Z^n}, \quad \epsilon = \frac{\epsilon_r}{Z^{1/2}},$$
(C.12)

where we have introduced the dimensionless field rescaling factor Z and the dimensionless counterterms δa_n . The rescaling of ϕ follows from rescaling $\sigma = Z^{1/2}\sigma_r$, $\pi_a = Z^{1/2}\pi_{a,r}$ in the original Lagrangian. The remaining fields and parameters of the Lagrangian are assumed to be already in their renormalized form. Therefore, the only terms in the mean-field Lagrangian (3.8) affected by the renormalization (C.12) are

$$U + \Delta U = \sum_{n=1}^{4} \frac{a_{n,r} + f_{\pi,r}^{4-2n} \delta a_n}{n!} \frac{(\phi_r^2 - f_{\pi,r}^2)^n}{2^n} - \epsilon_r (\phi_r - f_{\pi,r}) + 2Z\phi_r^2 q^2 + (1 - \delta_{0q})\epsilon_r \phi_r$$

$$= (U + \Delta U)_r + f_{\pi,r}^4 \left[\left(-\frac{\delta a_1}{2} + \frac{\delta a_2}{8} - \frac{\delta a_3}{48} + \frac{\delta a_4}{384} \right) + \left(\frac{\delta a_1}{2} - \frac{\delta a_2}{4} + \frac{\delta a_3}{16} - \frac{\delta a_4}{96} \right) \phi^2 + \left(\frac{\delta a_2}{8} - \frac{\delta a_3}{16} + \frac{\delta a_4}{64} \right) \phi^4$$

$$+ \left(\frac{\delta a_3}{48} - \frac{\delta a_4}{96} \right) \phi^6 + \frac{\delta a_4}{348} \phi^8 + 2(Z - 1)\phi_r^2 q^2, \tag{C.13}$$

where $(U + \Delta U)_r$ is given by U and ΔU from Eq. (3.11) with ϕ , f_{π} , a_n , ϵ replaced by their renormalized versions, and where φ is defined in Eq. (3.27).

We observe from Eq. (C.11) that we need to cancel divergent terms in P_{vac} proportional to M^2 , M^4 , and q^2M^2 . Since M and q are dynamical quantities that depend on the medium, this cancelation has to be done order by order with the help of the counterterms in Eq. (C.13). To make the cancelation explicit we divide the counterterms and the field rescaling into divergent and finite parts,

$$\delta a_n = \delta a_n^{\Lambda} + \delta a_n^{\rm f}, \qquad Z = Z^{\Lambda} + Z^{\rm f}.$$
 (C.14)

The divergent terms proportional to M^2 and M^4 are then canceled (and no new divergences introduced) by the choice

$$\delta a_1^{\Lambda} = \frac{g_{\sigma,r}^4}{2\pi^2} \left(\frac{\Lambda^2}{m_N^2} + \ln \frac{\ell^2}{\Lambda^2} + \gamma - \frac{3}{2} \right), \qquad \delta a_2^{\Lambda} = \frac{g_{\sigma,r}^4}{\pi^2} \left(\ln \frac{\ell^2}{\Lambda^2} + \gamma - \frac{3}{2} \right),$$

$$\delta a_3^{\Lambda} = \delta a_4^{\Lambda} = 0, \qquad (C.15)$$

while the divergent term proportional to q^2M^2 is canceled by

$$Z^{\Lambda} = \frac{g_{\sigma,r}^2}{4\pi^2} \left(\ln \frac{\ell^2}{\Lambda^2} + \gamma - \frac{3}{2} \right) . \tag{C.16}$$

Besides the divergent terms, the vacuum contribution (C.11) also contains finite logarithmic terms, with prefactors M^4 and q^2M^2 . Let us start with the logarithmic term with prefactor M^4 . We combine this contribution with the finite part of the counterterms $\delta a_n^{\rm f}$. While for the identification of the divergent parts of the counterterms we applied an expansion in φ (C.13), we now expand about the vacuum, i.e., in φ^2-1 , to write

$$\sum_{n=1}^{4} \frac{a_{n,r} + f_{\pi,r}^{4-2n} \, \delta a_n^f}{n!} \frac{(\phi_r^2 - f_{\pi,r}^2)^n}{2^n} - \frac{M^4}{8\pi^2} \ln \frac{M^2}{\ell^2}$$

$$= -\frac{m_N^4}{8\pi^2} \ln \frac{m_N^2}{\ell^2} + \sum_{n=1}^{4} \frac{A_n}{n!} \frac{(\varphi^2 - 1)^n}{2^n} + \frac{m_N^4}{4\pi^2} \sum_{n=5}^{\infty} \frac{(-1)^n (\varphi^2 - 1)^n}{n(n-1)(n-2)}, \quad (C.17)$$

where

$$A_{1} \equiv f_{\pi,r}^{2} a_{1,r} + f_{\pi,r}^{4} \left[\delta a_{1}^{f} - \frac{g_{\sigma,r}^{4}}{4\pi^{2}} \left(1 + 2 \ln \frac{m_{N}^{2}}{\ell^{2}} \right) \right] ,$$

$$A_{2} \equiv f_{\pi,r}^{4} a_{2,r} + f_{\pi,r}^{4} \left[\delta a_{2}^{f} - \frac{g_{\sigma,r}^{4}}{2\pi^{2}} \left(3 + 2 \ln \frac{m_{N}^{2}}{\ell^{2}} \right) \right] ,$$

$$A_{3} \equiv f_{\pi,r}^{6} a_{3,r} + f_{\pi,r}^{4} \left(\delta a_{3}^{f} - \frac{2g_{\sigma,r}^{4}}{\pi^{2}} \right) , \quad A_{4} \equiv f_{\pi,r}^{8} a_{4,r} + f_{\pi,r}^{4} \left(\delta a_{4}^{f} + \frac{4g_{\sigma,r}^{4}}{\pi^{2}} \right)$$
(C.18)

The new coefficients A_n entirely encode the form of the scalar potential and they will be fixed to physical properties of the vacuum and saturated nuclear matter. As a consequence, the choice of the renormalization scale and the finite counterterms is irrelevant here; for any particular choice of ℓ and δa_n^f the coefficients $a_{n,r}$ can be

readjusted to reproduce the desired values for A_n . This implies that the form of the original mesonic potential, which contains terms $(\varphi^2 - 1)^n$ for n = 1, 2, 3, 4, is not altered by the renormalization scheme, although the coefficients of these terms will assume different values due to the Dirac sea. The reason is the presence of the higher-order terms $(\varphi^2 - 1)^n$ for $n \ge 5$, given by the last term in Eq. (C.17). They do not depend on any free parameters and cannot be eliminated by any choice of the renormalization scale or the counterterms. We can rewrite this infinite sum in the closed form

$$\frac{m_N^4}{4\pi^2} \sum_{n=5}^{\infty} \frac{(-1)^n (\varphi^2 - 1)^n}{n(n-1)(n-2)} = \frac{m_N^4}{96\pi^2} (1 - 8\varphi^2 - 12\varphi^4 \ln \varphi^2 + 8\varphi^6 - \varphi^8).$$
 (C.19)

Next, we consider the logarithmic term with a q-dependent prefactor in Eq. (C.11). Combining this term with the finite part of the field rescaling from Eq. (C.13), we write

$$2(Z^{f}-1)\phi_{r}^{2}q^{2} - \frac{q^{2}M^{2}}{2\pi^{2}}\left(\ln\frac{M^{2}}{\ell^{2}} + \frac{3}{2}\right) = -\frac{q^{2}M^{2}}{2\pi^{2}}\ln\frac{M^{2}}{\ell^{2}}, \quad (C.20)$$

where we have set

$$Z^{\rm f} = 1 + \frac{3g_{\sigma,r}^2}{8\pi^2}.$$
 (C.21)

This choice leaves a renormalization scale dependence, in contrast to the case of the *q*-independent contribution. As we discuss in the main text, this renormalization scale dependence gives us an important freedom to eliminate unphysical properties of our effective potential.

Putting everything together, we can write

$$-2P_{\text{vac}} + U + \Delta U = \frac{\Lambda^4}{8\pi^2} - \frac{\Lambda^2 m_N^2}{4\pi^2} - \frac{m_N^4}{8\pi^2} \left(\ln \frac{m_N^2}{\Lambda^2} - \frac{3}{2} + \gamma \right) + \tilde{U} + \Delta \tilde{U}, \quad (C.22)$$

where we have absorbed the effects from the nucleonic Dirac sea into a new effective potential, given by

$$\tilde{U} = \sum_{n=1}^{4} \frac{A_n}{n!} \frac{(\varphi^2 - 1)^n}{2^n} - \epsilon_r (\phi_r - f_{\pi,r})$$

$$+ \frac{m_N^2}{96\pi^2} (1 - 8\varphi^2 - 12\varphi^4 \ln \varphi^2 + 8\varphi^6 - \varphi^8), \qquad (C.23a)$$

$$\Delta \tilde{U} = 2\phi_r^2 q^2 \left(1 - \frac{g_{\sigma,r}^2}{4\pi^2} \ln \frac{M^2}{\ell^2} \right) - \frac{q^4}{2\pi^2} F(y) + (1 - \delta_{0q}) \epsilon_r \phi_r.$$
 (C.23b)

As for the original potential, we have separated the q-dependent part $\Delta \tilde{U}$ such that the potential reduces to \tilde{U} for q=0. Dropping the irrelevant (divergent, but constant) terms in Eq. (C.22), denoting the renormalized quantities for simplicity without the subscript r and renaming $A_n/f_\pi^{2n} \to a_n$, we arrive at the result (3.25) given in the main text.

C.3 Matter contributions to densities and axial current

In this appendix we present the explicit expressions for the matter contributions to the stationarity equations (3.34). The baryon density from a single nucleonic degree of freedom is

$$\frac{\partial P_{\text{mat}}}{\partial \mu} = \frac{1}{2\pi^2} \sum_{s=\pm} \int_0^\infty dk_\ell \int_0^\infty dk_\perp k_\perp \Theta(\mu_* - E_k^s)
= -\frac{\Theta(\mu_* - q - M)}{4\pi^2} \left\{ M^2 q \ln \frac{\mu_* - q + k_-}{M} + \frac{k_-}{3} [2(M^2 - \mu_*^2) + q(q + \mu_*)] \right\}
+ \frac{\Theta(\mu_* + q - M)}{4\pi^2} \left\{ M^2 q \ln \frac{\mu_* + q + k_+}{M} - \frac{k_+}{3} [2(M^2 - \mu_*^2) + q(q - \mu_*)] \right\}
- \frac{\Theta(q - \mu_* - M)}{4\pi^2} \left\{ M^2 q \ln \frac{q - \mu_* + k_-}{M} - \frac{k_-}{3} [2(M^2 - \mu_*^2) + q(q + \mu_*)] \right\},$$
(C.24)

with k_{\pm} from Eq. (3.22). To obtain the baryon density n_B in the stationarity equation (3.34b) the result has to be multiplied by 2 due to the (degenerate) contributions from

neutrons and protons. One easily checks that one obtains the expected limits

$$\frac{\partial P_{\text{mat}}}{\partial \mu} = \begin{cases}
\frac{\Theta(\mu_* - M)k_F^3}{3\pi^2} & \text{for } q = 0\\ \frac{\mu_*^3}{3\pi^2} & \text{for } M = 0
\end{cases}$$
(C.25)

In particular, the density does not depend on q for zero fermion mass M = 0.

The scalar density is given by

$$-\frac{\partial P_{\text{mat}}}{\partial M} = \frac{1}{2\pi^{2}} \sum_{s=\pm} \int_{0}^{\infty} dk_{\ell} \int_{0}^{\infty} dk_{\perp} k_{\perp} \frac{M}{E_{k}^{s}} \left(1 + \frac{sq}{\sqrt{k_{\ell}^{2} + M^{2}}} \right) \Theta(\mu - E_{k}^{s})$$

$$= -\frac{\Theta(\mu_{*} - q - M)M}{4\pi^{2}} \left\{ [M^{2} + 2q(q - \mu_{*})] \ln \frac{\mu_{*} - q + k_{-}}{M} - (\mu_{*} - 3q)k_{-} \right\}$$

$$-\frac{\Theta(\mu_{*} + q - M)M}{4\pi^{2}} \left\{ [M^{2} + 2q(q + \mu_{*})] \ln \frac{\mu_{*} + q + k_{+}}{M} - (\mu_{*} + 3q)k_{+} \right\}$$

$$-\frac{\Theta(q - \mu_{*} - M)M}{4\pi^{2}} \left\{ [M^{2} + 2q(q - \mu_{*})] \ln \frac{q - \mu_{*} + k_{-}}{M} + (\mu_{*} - 3q)k_{-} \right\}$$

$$+\frac{\Theta(q - M)M}{2\pi^{2}} \left[(M^{2} + 2q^{2}) \ln \frac{q + \sqrt{q^{2} - M^{2}}}{M} - 3q\sqrt{q^{2} - M^{2}} \right]. \quad (C.26)$$

In this case, we recover the well-known expression for q = 0,

$$-\frac{\partial P_{\text{mat}}}{\partial M} = \frac{\Theta(\mu_* - M)M}{2\pi^2} \left(\mu_* k_F - M^2 \ln \frac{\mu_* + k_F}{M}\right), \qquad (C.27)$$

while for small *M* we find the expansion

$$-\frac{\partial P_{\text{mat}}}{\partial M} = \frac{M}{2\pi^2} \left(\mu_*^2 - \mu_* q \ln \left| \frac{\mu_* + q}{\mu_* - q} \right| - q^2 \ln \left| \frac{\mu_*^2}{q^2} - 1 \right| \right) + \mathcal{O}(M^3), \quad (C.28)$$

which confirms that Eq. (3.34a) is solved by M=0 in the chiral limit $\epsilon=0$.

Finally, the axial current from a single nucleonic degree of freedom is

$$-\frac{\partial P_{\text{mat}}}{\partial q} = \frac{1}{2\pi^{2}} \sum_{s=\pm} s \int_{0}^{\infty} dk_{\ell} \int_{0}^{\infty} dk_{\perp} k_{\perp} \frac{\sqrt{k_{\ell}^{2} + M^{2} + sq}}{E_{k}^{s}} \Theta(\mu - E_{k}^{s})$$

$$= \frac{\Theta(\mu_{*} - q - M)}{4\pi^{2}} \left[M^{2}(\mu_{*} - 2q) \ln \frac{\mu_{*} - q + k_{-}}{M} - \frac{k_{-}}{3} (4M^{2} - \mu_{*}^{2} - \mu_{*}q + 2q^{2}) \right]$$

$$-\frac{\Theta(\mu_{*} + q - M)}{4\pi^{2}} \left[M^{2}(\mu_{*} + 2q) \ln \frac{\mu_{*} + q + k_{+}}{M} - \frac{k_{+}}{3} (4M^{2} - \mu_{*}^{2} + \mu_{*}q + 2q^{2}) \right]$$

$$+\frac{\Theta(q - \mu_{*} - M)}{4\pi^{2}} \left[M^{2}(\mu_{*} - 2q) \ln \frac{q - \mu_{*} + k_{-}}{M} + \frac{k_{-}}{3} (4M^{2} - \mu_{*}^{2} - \mu_{*}q + 2q^{2}) \right]$$

$$+\frac{\Theta(q - M)}{\pi^{2}} \left[M^{2}q \ln \frac{q + \sqrt{q^{2} - M^{2}}}{M} - \frac{\sqrt{q^{2} - M^{2}}}{3} (2M^{2} + q^{2}) \right]. \tag{C.29}$$

The current is linear in q for small q,

$$-\frac{\partial P_{\text{mat}}}{\partial q} = -q \frac{\Theta(\mu_* - M)M^2}{\pi^2} \ln \frac{\mu_* + k_F}{M} + \mathcal{O}(q^2), \qquad (C.30)$$

while it is quadratic in M for small M,

$$-\frac{\partial P_{\text{mat}}}{\partial q} = -\frac{M^2}{2\pi^2} \left(\frac{\mu_*}{2} \ln \left| \frac{\mu_* + q}{\mu_* - q} \right| + q \ln \left| \frac{\mu_*^2}{q^2} - 1 \right| \right) + \mathcal{O}(M^4).$$
 (C.31)

Appendix D

Model parameters

In this appendix we, firstly, present – for completeness and replicability – the model parameters used for the specific cases discussed in Secs. 3.3.1 and 3.3.2, see Table D.1.

8ω	a ₂	$a_3[{ m MeV}^{-2}]$	$a_4[{ m MeV^{-4}}]$	d	M_0/m_N	L[MeV]	$m_{\sigma}[\mathrm{MeV}]$	$m_{\pi}[\text{MeV}]$	sea
7.574	59.94	-9.427×10^{-3}	1.188×10^{-4}	0	0.82	87.3	708	0	-
7.574	57.75	-2.247×10^{-2}	8.612×10^{-5}	0	0.82	87.3	708	0	√
7.574	57.66	-8.892×10^{-3}	1.178×10^{-4}	0	0.82	87.3	707	139	- 1
7.574	55.48	-2.193×10^{-2}	8.512×10^{-5}	0	0.82	87.3	707	139	√
12.45	130.8	0.4333	7.850×10^{-4}	10^{4}	0.81	53.8	1063	0	√
12.45	128.5	0.4338	7.840×10^{-4}	10^{4}	0.81	53.8	1063	139	√

TABLE D.1: Parameter sets together with resulting physical quantities used for the left panel of Fig. 3.1 (top four rows) and for Fig. 3.2 (bottom two rows). In all cases, $K = 250 \, \text{MeV}$, and the remaining vacuum and saturation properties not shown here are fixed to their physical values. To compute L we always use a value for the symmetry energy of $S = 32 \, \text{MeV}$. The last column indicates whether the Dirac sea is taken into account or not, which is relevant for the parameter fit.

In our main results in Sec. 3.3.3, the parameters are varied continuously. Therefore, secondly, we present the most relevant physical information about these continuous parameter sets in Fig. D.1. This figure shows the slope parameter of the symmetry energy L and the sigma mass m_{σ} for different values of the vector meson self-coupling and the incompressibility as a function of the effective nucleon mass at saturation, computed from Eqs. (3.42b) and (3.36). Additionally, we show the coefficient of the leading-order term of the effective potential for large chiral condensates.

$$\tilde{U}(\phi) = a_{(8)}\phi^8 + \mathcal{O}(\phi^6), \qquad a_{(8)} \equiv \frac{1}{96} \left(\frac{a_4}{4} - \frac{g_\sigma^4}{\pi^2 f_\pi^4} \right).$$
 (D.1)

The sign of $a_{(8)}$ indicates whether the potential is bounded from below for large ϕ . The Dirac sea contribution is negative and thus tends to render the potential unbounded, which is indeed the case for small vales of d and not too large values of M_0 , as the figure demonstrates.

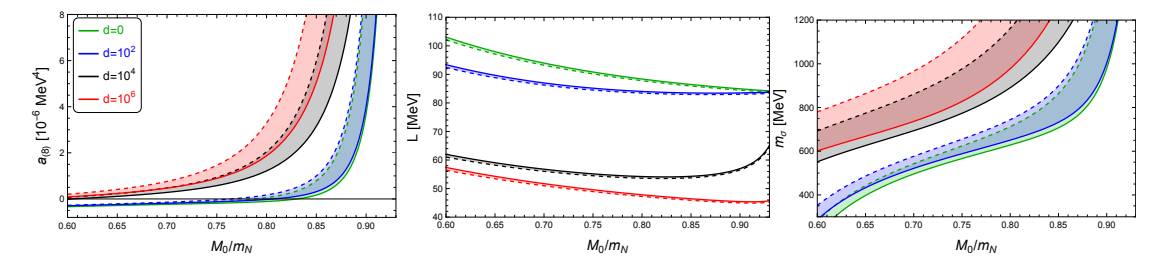


FIGURE D.1: Leading-order coefficient of the effective potential $a_{(8)}$, slope parameter of the symmetry energy L, and sigma mass m_σ , as the effective nucleon mass at saturation M_0 is varied, with all other saturation properties kept fixed. In each panel, the results for 4 different values of the vector meson self-coupling d are shown, corresponding to the 4 values in the right panel of Fig. 3.4. The bands indicate the range between $K=200\,\mathrm{MeV}$ (solid lines) and $K=300\,\mathrm{MeV}$ (dashed lines). All curves are calculated with the physical pion mass. The chiral limit gives slightly different curves but the differences would barely be visible on the scale of these plots.

References

- [1] Eduardo S. Fraga, Rodrigo da Mata, Savvas Pitsinigkos, and Andreas Schmitt. Strange quark matter from a baryonic approach. *Phys. Rev. D*, 106(7):074018, Oct 2022.
- [2] Savvas Pitsinigkos and Andreas Schmitt. Chiral crossover versus chiral density wave in dense nuclear matter. *Phys. Rev. D*, 109:014024, Jan 2024. .
- [3] David J. Gross and Frank Wilczek. Ultraviolet behavior of non-abelian gauge theories. *Phys. Rev. Lett.*, 30:1343–1346, Jun 1973. .
- [4] H. David Politzer. Reliable perturbative results for strong interactions? *Phys. Rev. Lett.*, 30:1346–1349, Jun 1973. .
- [5] Juerg Beringer, JF Arguin, RM Barnett, K Copic, O Dahl, DE Groom, CJ Lin, J Lys, H Murayama, CG Wohl, et al. Review of particle physics. *Physical Review D*, 86(1), 2012.
- [6] Yoichiro Nambu. Quasi-particles and gauge invariance in the theory of superconductivity. *Phys. Rev.*, 117:648–663, Feb 1960.
- [7] Yoichiro Nambu and G. Jona-Lasinio. Dynamical Model of Elementary Particles Based on an Analogy with Superconductivity. 1. *Phys.Rev.*, 122:345–358, 1961.
- [8] Yoichiro Nambu and G. Jona-Lasinio. Dynamical model of elementary particles based on an analogy with superconductivity. II. *Phys.Rev.*, 124:246–254, 1961.
- [9] Jeffrey Goldstone. Field theories with superconductor solutions. *Il Nuovo Cimento* (1955-1965), 19:154–164, 1961.
- [10] Jeffrey Goldstone, Abdus Salam, and Steven Weinberg. Broken symmetries. *Phys. Rev.*, 127:965–970, Aug 1962.

[11] Ruprecht Machleidt and David Rodrignez Entem. Chiral effective field theory and nuclear forces. *Physics Reports*, 503(1):1–75, 2011.

- [12] Y. Aoki, G. Endrődi, Z. Fodor, S.D. Katz, and K.K. Szabó. The Order of the quantum chromodynamics transition predicted by the standard model of particle physics. *Nature*, 443:675–678, 2006.
- [13] Y. Aoki, Z. Fodor, S.D. Katz, and K.K. Szabó. The QCD transition temperature: Results with physical masses in the continuum limit. *Phys.Lett.*, B643:46–54, 2006.
- [14] Yasumichi Aoki, Szabolcs Borsanyi, Stephan Dürr, Zoltan Fodor, Sandor D Katz, Stefan Krieg, and Kalman Szabo. The qcd transition temperature: results with physical masses in the continuum limit ii. *Journal of High Energy Physics*, 2009 (06):088, 2009.
- [15] Keitaro Nagata. Finite-density lattice qcd and sign problem: Current status and open problems. *Progress in Particle and Nuclear Physics*, 127:103991, 2022.
- [16] Peter Hasenfratz and Frithjof Karsch. Chemical potential on the lattice. *Physics Letters B*, 125(4):308–310, 1983.
- [17] Ulrich Heinz and Maurice Jacob. Evidence for a new state of matter: An assessment of the results from the cern lead beam programme. *arXiv* preprint nucl-th/0002042, 2000.
- [18] John Adams, MM Aggarwal, Z Ahammed, J Amonett, BD Anderson, D Arkhipkin, GS Averichev, SK Badyal, Y Bai, J Balewski, et al. Experimental and theoretical challenges in the search for the quark–gluon plasma: The star collaboration's critical assessment of the evidence from rhic collisions. *Nuclear Physics A*, 757(1-2):102–183, 2005.
- [19] Kenneth Aamodt, B Abelev, A Abrahantes Quintana, D Adamova, AM Adare, MM Aggarwal, G Aglieri Rinella, AG Agocs, S Aguilar Salazar, Z Ahammed, et al. Elliptic flow of charged particles in pb-pb collisions at s nn= 2.76 tev. *Physical review letters*, 105(25):252302, 2010.

[20] Atlas Collaboration et al. Observation of a centrality-dependent dijet asymmetry in lead-lead collisions at sqrt (s (nn))= 2.76 tev with the atlas detector at the lhc. *arXiv preprint arXiv:1011.6182*, 2010.

- [21] Qian Yang, STAR Collaboration, et al. The star bes-ii and forward rapidity physics and upgrades. *Nuclear Physics A*, 982:951–954, 2019.
- [22] A Korobitsyn. Star experiment results from bes program. *Physics of Particles and Nuclei*, 55(4):1037–1042, 2024.
- [23] STAR Collaboration et al. Measurements of charged-particle multiplicity dependence of higher-order net-proton cumulants in p+p collisions at \sqrt{s} = 200 gev from star at rhic. *arXiv preprint arXiv:2311.00934*, 2023.
- [24] Shinji Ejiri. Canonical partition function and finite density phase transition in lattice qcd. *Phys. Rev. D*, 78:074507, Oct 2008. .
- [25] E. S. Bowman and J. I. Kapusta. Critical points in the linear σ model with quarks. *Phys. Rev. C*, 79:015202, Jan 2009.
- [26] Thomas Schäfer and Frank Wilczek. Continuity of quark and hadron matter. *Phys. Rev. Lett.*, 82:3956–3959, 1999. .
- [27] G Bertsch and Philip J Siemens. Nuclear fragmentation. *Physics Letters B*, 126 (1-2):9–12, 1983.
- [28] Philip J Siemens. Liquid–gas phase transition in nuclear matter. *Nature*, 305 (5933):410–412, 1983.
- [29] C. J. Horowitz, J. Piekarewicz, and Brendan Reed. Insights into nuclear saturation density from parity-violating electron scattering. *Phys. Rev. C*, 102: 044321, Oct 2020. .
- [30] K Pomorski and Jerzy Dudek. Nuclear liquid-drop model and surface-curvature effects. *Physical Review C*, 67(4):044316, 2003.
- [31] Yongjia Wang, Chenchen Guo, Qingfeng Li, Arnaud Le Fèvre, Yvonne Leifels, and Wolfgang Trautmann. Determination of the nuclear incompressibility from the rapidity-dependent elliptic flow in heavy-ion collisions at beam energies 0.4 a–1.0 a gev. *Physics Letters B*, 778:207–212, 2018.

[32] M Baldo and GF Burgio. The nuclear symmetry energy. *Progress in Particle and Nuclear Physics*, 91:203–258, 2016.

- [33] Brendan T. Reed, F. J. Fattoyev, C. J. Horowitz, and J. Piekarewicz. Implications of PREX-2 on the Equation of State of Neutron-Rich Matter. *Phys. Rev. Lett.*, 126 (17):172503, 2021.
- [34] M Baldo, J Cugnon, André Lejeune, and Umberto Lombardo. Superfluidity in neutron matter and nuclear matter with realistic interactions. *Nuclear Physics A*, 515(3):409–432, 1990.
- [35] Tatsuyuki Takatsuka and Ryozo Tamagaki. Superfluidity in neutron star matter and symmetric nuclear matter. *Progress of Theoretical Physics Supplement*, 112: 27–65, 1993.
- [36] Stefano Gandolfi, Georgios Palkanoglou, Joseph Carlson, Alexandros Gezerlis, and Kevin E Schmidt. The 1s0 pairing gap in neutron matter. *Condensed Matter*, 7(1):19, 2022.
- [37] Georgios Palkanoglou, Michael Stuck, and Alexandros Gezerlis. Spin-triplet pairing in heavy nuclei is stable against deformation. *arXiv preprint arXiv:*2402.13313, 2024.
- [38] Mark G. Alford, Krishna Rajagopal, and Frank Wilczek. Color flavor locking and chiral symmetry breaking in high density QCD. *Nucl.Phys.*, B537:443–458, 1999.
- [39] Mark Alford, Krishna Rajagopal, and Frank Wilczek. Qcd at finite baryon density: Nucleon droplets and color superconductivity. *Physics Letters B*, 422 (1-4):247–256, 1998.
- [40] Peter Fulde and Richard A. Ferrell. Superconductivity in a strong spin-exchange field. *Phys. Rev.*, 135:A550–A563, Aug 1964. .
- [41] Anatoly I Larkin. Inhomogeneous state of superconductors. *Sov. Phys. JETP*, 20: 762, 1965.
- [42] Mark G. Alford, Andreas Schmitt, Krishna Rajagopal, and Thomas Schäfer. Color superconductivity in dense quark matter. *Rev.Mod.Phys.*, 80:1455–1515, 2008.

[43] Robert C. Duncan and Christopher Thompson. Formation of very strongly magnetized neutron stars - implications for gamma-ray bursts. *Astrophys.J.*, 392: L9, 1992.

- [44] Ben Margalit, Adam S Jermyn, Brian D Metzger, Luke F Roberts, and Eliot Quataert. Angular-momentum transport in proto-neutron stars and the fate of neutron star merger remnants. *The Astrophysical Journal*, 939(1):51, 2022.
- [45] J. D. Walecka. A Theory of highly condensed matter. *Annals Phys.*, 83:491–529, 1974.
- [46] C. Sasaki, B. Friman, and K. Redlich. Quark number fluctuations in a chiral model at finite baryon chemical potential. *Phys. Rev. D*, 75:054026, Mar 2007.
- [47] Michał Marczenko, David Blaschke, Krzysztof Redlich, and Chihiro Sasaki. Toward a unified equation of state for multi-messenger astronomy. *Astron. Astrophys.*, 643:A82, 2020.
- [48] V. Dexheimer, R. O. Gomes, T. Klähn, S. Han, and M. Salinas. GW190814 as a massive rapidly rotating neutron star with exotic degrees of freedom. *Phys. Rev.* C, 103(2):025808, 2021.
- [49] Andreas Schmitt. Chiral pasta: Mixed phases at the chiral phase transition. *Phys. Rev. D*, 101(7):074007, 2020.
- [50] D. G. Ravenhall, C. J. Pethick, and J. R. Wilson. Structure of matter below nuclear saturation density. *Phys. Rev. Lett.*, 50:2066–2069, Jun 1983.
- [51] E. Nakano and T. Tatsumi. Chiral symmetry and density wave in quark matter. *Phys.Rev.*, D71:114006, 2005.
- [52] Dominik Nickel. Inhomogeneous phases in the Nambu-Jona-Lasino and quark-meson model. *Phys.Rev.*, D80:074025, 2009.
- [53] I. E. Frolov, V. Ch. Zhukovsky, and K. G. Klimenko. Chiral density waves in quark matter within the Nambu-Jona-Lasinio model in an external magnetic field. *Phys.Rev.*, D82:076002, 2010. .
- [54] Stefano Carignano and Michael Buballa. Inhomogeneous islands and continents in the Nambu–Jona-Lasinio model. *Acta Phys. Polon. Supp.*, 5:641–658, 2012. .

[55] Stefano Carignano, Michael Buballa, and Bernd-Jochen Schaefer. Inhomogeneous phases in the quark-meson model with vacuum fluctuations. *Phys. Rev. D*, 90(1):014033, 2014.

- [56] Michael Buballa and Stefano Carignano. Inhomogeneous chiral symmetry breaking in dense neutron-star matter. *Eur. Phys. J. A*, 52(3):57, 2016.
- [57] Prabal Adhikari, Jens O. Andersen, and Patrick Kneschke. On-shell parameter fixing in the quark-meson model. *Phys. Rev. D*, 95(3):036017, 2017.
- [58] Prabal Adhikari, Jens O. Andersen, and Patrick Kneschke. Inhomogeneous chiral condensate in the quark-meson model. *Phys. Rev. D*, 96(1):016013, 2017. . [Erratum: Phys.Rev.D 98, 099902 (2018)].
- [59] Jens O. Andersen and Patrick Kneschke. Chiral density wave versus pion condensation at finite density and zero temperature. *Phys. Rev. D*, 97(7):076005, 2018.
- [60] Efrain J. Ferrer and Vivian de la Incera. Absence of Landau-Peierls Instability in the Magnetic Dual Chiral Density Wave Phase of Dense QCD. *Phys. Rev. D*, 102 (1):014010, 2020.
- [61] Stefano Carignano and Michael Buballa. Inhomogeneous chiral condensates in three-flavor quark matter. *Phys. Rev. D*, 101(1):014026, 2020.
- [62] Phillip Lakaschus, Michael Buballa, and Dirk H. Rischke. Competition of inhomogeneous chiral phases and two-flavor color superconductivity in the NJL model. *Phys. Rev. D*, 103(3):034030, 2021.
- [63] Michael Buballa, Stefano Carignano, and Lennart Kurth. Inhomogeneous phases in the quark-meson model with explicit chiral-symmetry breaking. *Eur. Phys. J. ST*, 229(22-23):3371–3385, 2020.
- [64] F. Dautry and E. M. Nyman. PION CONDENSATION AND THE SIGMA MODEL IN LIQUID NEUTRON MATTER. Nucl. Phys. A, 319:323–348, 1979.
- [65] Koichi Takahashi and Toshitaka Tatsumi. Sigma pi0 condensation at finite density in the linear sigma model. *Phys. Rev. C*, 63:015205, 2001.

[66] Koichi Takahashi. Neutral pion condensation in the chiral SU(3) x SU(3) model. *Phys. Rev. C*, 66:025202, 2002. .

- [67] Achim Heinz, Francesco Giacosa, and Dirk H. Rischke. Chiral density wave in nuclear matter. *Nucl. Phys. A*, 933:34–42, 2015.
- [68] Oliver Schnetz, Michael Thies, and Konrad Urlichs. Phase diagram of the gross–neveu model: exact results and condensed matter precursors. *Annals of Physics*, 314(2):425–447, 2004.
- [69] Subrahmanyan Chandrasekhar. The maximum mass of ideal white dwarfs. *Astrophysical Journal*, vol. 74, p. 81, 74:81, 1931.
- [70] Dima G Yakovlev and CJ Pethick. Neutron star cooling. *Annu. Rev. Astron. Astrophys.*, 42(1):169–210, 2004.
- [71] Nicolas Chamel and Pawel Haensel. Physics of neutron star crusts. *Living Reviews in relativity*, 11(1):1–182, 2008.
- [72] M Ali Alpar and Altan Baykal. Expectancy of large pulsar glitches: a comparison of models with the observed glitch sample. *Monthly Notices of the Royal Astronomical Society*, 269(4):849–856, 1994.
- [73] Bennett Link and Curt Cutler. Vortex unpinning in precessing neutron stars. *Monthly Notices of the Royal Astronomical Society*, 336(1):211–216, 2002.
- [74] C Drischler, JW Holt, and C Wellenhofer. Chiral effective field theory and the high-density nuclear equation of state. *Annual Review of Nuclear and Particle Science*, 71(1):403–432, 2021.
- [75] Laura Tolos and Laura Fabbietti. Strangeness in Nuclei and Neutron Stars. *Prog. Part. Nucl. Phys.*, 112:103770, 2020. .
- [76] Matteo Breschi, Sebastiano Bernuzzi, Daniel Godzieba, Albino Perego, and David Radice. Constraints on the maximum densities of neutron stars from postmerger gravitational waves with third-generation observations. *Physical review letters*, 128(16):161102, 2022.
- [77] Eemeli Annala, Tyler Gorda, Aleksi Kurkela, Joonas Nättilä, and Aleksi Vuorinen. Evidence for quark-matter cores in massive neutron stars. *Nature Phys.*, 16(9):907–910, 2020.

[78] Roger W Romani, D Kandel, Alexei V Filippenko, Thomas G Brink, and WeiKang Zheng. Psr j0952- 0607: The fastest and heaviest known galactic neutron star. *The Astrophysical Journal Letters*, 934(2):L17, 2022.

- [79] Isaac Legred, Katerina Chatziioannou, Reed Essick, Sophia Han, and Philippe Landry. Impact of the psr j 0740+ 6620 radius constraint on the properties of high-density matter. *Physical Review D*, 104(6):063003, 2021.
- [80] J. S. Langer and L. A. Turski. Hydrodynamic model of the condensation of a vapor near its critical point. *Phys. Rev. A*, 8:3230–3243, Dec 1973. .
- [81] L. A. Turski and J. S. Langer. Dynamics of a diffuse liquid-vapor interface. *Phys. Rev. A*, 22:2189–2195, Nov 1980. .
- [82] Laszlo P. Csernai and Joseph I. Kapusta. Nucleation of relativistic first order phase transitions. *Phys. Rev. D*, 46:1379–1390, 1992. .
- [83] Sidney R. Coleman. The Fate of the False Vacuum. 1. Semiclassical Theory. *Phys. Rev.*, D15:2929–2936, 1977. . [Erratum: D16, 1248 (1977)].
- [84] Curtis G. Callan, Jr. and Sidney R. Coleman. The Fate of the False Vacuum. 2. First Quantum Corrections. *Phys. Rev. D*, 16:1762–1768, 1977. .
- [85] Mark G. Alford, Sophia Han, and Madappa Prakash. Generic conditions for stable hybrid stars. *Phys. Rev. D*, 88(8):083013, 2013. .
- [86] Jan-Erik Christian, Andreas Zacchi, and Jürgen Schaffner-Bielich. Signals in the tidal deformability for phase transitions in compact stars with constraints from GW170817. *Phys. Rev.*, D99(2):023009, 2019.
- [87] Bryen Irving, Thomas Klähn, Prashanth Jaikumar, Marc Salinas, and Wei Wei. Identifying Quark Matter in Hybrid Stars through Relativistic Tidal Deformations. *Universe*, 5(9):193, 2019.
- [88] Jonas P. Pereira, Michał Bejger, Nils Andersson, and Fabian Gittins. Tidal deformations of hybrid stars with sharp phase transitions and elastic crusts. *Astrophys. J.*, 895(1):28, 2020. .
- [89] David Blaschke, Alexander Ayriyan, David Edwin Alvarez-Castillo, and Hovik Grigorian. Was GW170817 a Canonical Neutron Star Merger? Bayesian Analysis with a Third Family of Compact Stars. *Universe*, 6(6):81, 2020.

[90] Niko Jokela, Matti Järvinen, Govert Nijs, and Jere Remes. Unified weak and strong coupling framework for nuclear matter and neutron stars. *Phys. Rev. D*, 103(8):086004, 2021.

- [91] Márcio Ferreira, Renan Câmara Pereira, and Constança Providência. Quark matter in light neutron stars. *Phys. Rev. D*, 102(8):083030, 2020.
- [92] Márcio Ferreira, Renan Câmara Pereira, and Constança Providência. Hybrid stars with large strange quark cores constrained by GW170817. *Phys. Rev. D*, 103 (12):123020, 2021.
- [93] Luiz L. Lopes, Carline Biesdorf, and Débora P. Menezes. Hypermassive quark cores. *Mon. Not. Roy. Astron. Soc.*, 512(4):5110–5121, 2022. .
- [94] Kazem Bitaghsir Fadafan, Farideh Kazemian, and Andreas Schmitt. Towards a holographic quark-hadron continuity. *JHEP*, 03:183, 2019.
- [95] Takaaki Ishii, Matti Järvinen, and Govert Nijs. Cool baryon and quark matter in holographic QCD. *JHEP*, 07:003, 2019.
- [96] Nicolas Kovensky and Andreas Schmitt. Holographic quarkyonic matter. *JHEP*, 09:112, 2020. .
- [97] Eduardo S. Fraga, Maurício Hippert, and Andreas Schmitt. Surface tension of dense matter at the chiral phase transition. *Phys. Rev. D*, 99(1):014046, 2019.
- [98] Alexander Haber, Florian Preis, and Andreas Schmitt. Magnetic catalysis in nuclear matter. *Phys. Rev.*, D90(12):125036, 2014. .
- [99] J. Boguta and A. R. Bodmer. Relativistic Calculation of Nuclear Matter and the Nuclear Surface. *Nucl. Phys. A*, 292:413–428, 1977. .
- [100] Y. Sugahara and H. Toki. Relativistic mean field theory for unstable nuclei with nonlinear sigma and omega terms. *Nucl. Phys. A*, 579:557–572, 1994. .
- [101] Jurgen Schaffner and Igor N. Mishustin. Hyperon rich matter in neutron stars. *Phys. Rev. C*, 53:1416–1429, 1996. .
- [102] Mark G. Alford and Alexander Haber. Strangeness-changing Rates and Hyperonic Bulk Viscosity in Neutron Star Mergers. Phys. Rev. C, 103(4):045810, 2021.

[103] Matthias Drews, Thomas Hell, Bertram Klein, and Wolfram Weise.

Thermodynamic phases and mesonic fluctuations in a chiral nucleon-meson model. *Phys.Rev.*, D88(9):096011, 2013.

- [104] Matthias Drews and Wolfram Weise. From asymmetric nuclear matter to neutron stars: a functional renormalization group study. *Phys. Rev.*, C91(3): 035802, 2015.
- [105] Armen Sedrakian and John W. Clark. Superfluidity in nuclear systems and neutron stars. *Eur. Phys. J. A*, 55(9):167, 2019.
- [106] H. T. Cromartie et al. Relativistic Shapiro delay measurements of an extremely massive millisecond pulsar. *Nature Astron.*, 4(1):72–76, 2020.
- [107] E. Fonseca et al. Refined Mass and Geometric Measurements of the High-mass PSR J0740+6620. *Astrophys. J. Lett.*, 915(1):L12, 2021.
- [108] J. Moreira, B. Hiller, W. Broniowski, A. A. Osipov, and A. H. Blin. Nonuniform phases in a three-flavor Nambu-Jona-Lasinio model. *Phys. Rev. D*, 89(3):036009, 2014.
- [109] V. Dexheimer and S. Schramm. Proto-Neutron and Neutron Stars in a Chiral SU(3) Model. *Astrophys. J.*, 683:943–948, 2008.
- [110] Jonathan T. Lenaghan, Dirk H. Rischke, and Jurgen Schaffner-Bielich. Chiral symmetry restoration at nonzero temperature in the SU(3)(r) x SU(3)(l) linear sigma model. *Phys. Rev. D*, 62:085008, 2000.
- [111] S. Weissenborn, D. Chatterjee, and J. Schaffner-Bielich. Hyperons and massive neutron stars: the role of hyperon potentials. *Nucl. Phys. A*, 881:62–77, 2012.
- [112] A. R. Bodmer. Relativistic mean field theory of nuclei with a vector meson selfinteraction. *Nucl. Phys. A*, 526:703–721, 1991. .
- [113] C. J. Horowitz and J. Piekarewicz. Constraining URCA cooling of neutron stars from the neutron radius of Pb-208. *Phys. Rev. C*, 66:055803, 2002.
- [114] Veronica Dexheimer, Rosana de Oliveira Gomes, Stefan Schramm, and Helena Pais. What do we learn about vector interactions from GW170817? *J. Phys. G*, 46 (3):034002, 2019.

[115] Eduardo S. Fraga and Ana Julia Mizher. Chiral transition in a strong magnetic background. *Phys. Rev. D*, 78:025016, 2008.

- [116] Ana Julia Mizher, M. N. Chernodub, and Eduardo S. Fraga. Phase diagram of hot QCD in an external magnetic field: possible splitting of deconfinement and chiral transitions. *Phys. Rev. D*, 82:105016, 2010.
- [117] G. Endrődi. QCD equation of state at nonzero magnetic fields in the Hadron Resonance Gas model. *JHEP*, 04:023, 2013. .
- [118] Horst Mueller and Brian D. Serot. Relativistic mean field theory and the high density nuclear equation of state. *Nucl. Phys. A*, 606:508–537, 1996. .
- [119] P. Papazoglou, S. Schramm, J. Schaffner-Bielich, Horst Stoecker, and W. Greiner. Chiral Lagrangian for strange hadronic matter. *Phys. Rev. C*, 57:2576–2588, 1998.
- [120] Armen Sedrakian, Jia-Jie Li, and Fridolin Weber. Hyperonization in compact stars. 5 2021.
- [121] Pawel Danielewicz and Jenny Lee. Symmetry Energy II: Isobaric Analog States. *Nucl. Phys.*, A922:1–70, 2014. .
- [122] James M. Lattimer and Andrew W. Steiner. Constraints on the symmetry energy using the mass-radius relation of neutron stars. *Eur. Phys. J.*, A50:40, 2014.
- [123] D. Adhikari et al. Accurate Determination of the Neutron Skin Thickness of ²⁰⁸Pb through Parity-Violation in Electron Scattering. *Phys. Rev. Lett.*, 126(17): 172502, 2021.
- [124] N. K. Glendenning. Vacuum polarization effects on nuclear matter and neutron stars. *Nuclear Physics A*, 493:521–548, March 1989. .
- [125] C. H. Johnson, D. J. Horen, and C. Mahaux. Unified description of the neutron-Pb-208 mean field between -20 and + 165 MeV from the dispersion relation constraint. *Phys.Rev.*, C36:2252–2273, 1987.
- [126] G. Q. Li, R. Machleidt, and R. Brockmann. Properties of dense nuclear and neutron matter with relativistic nucleon-nucleon interactions. *Phys.Rev.*, C45: 2782–2794, 1992. .

- [127] N. K. Glendenning. Compact Stars. Springer, New York, 2000.
- [128] M. Jaminon and C. Mahaux. Effective Masses in Relativistic Approaches to the Nucleon Nucleus Mean Field. *Phys.Rev.*, C40:354–367, 1989.
- [129] R. J. Furnstahl, John J. Rusnak, and Brian D. Serot. The Nuclear spin orbit force in chiral effective field theories. *Nucl. Phys.*, A632:607–623, 1998.
- [130] James M. Lattimer and Yeunhwan Lim. Constraining the Symmetry Parameters of the Nuclear Interaction. *Astrophys. J.*, 771:51, 2013.
- [131] M. Oertel, M. Hempel, T. Klähn, and S. Typel. Equations of state for supernovae and compact stars. *Rev. Mod. Phys.*, 89(1):015007, 2017.
- [132] Ingo Tews, James M. Lattimer, Akira Ohnishi, and Evgeni E. Kolomeitsev. Symmetry Parameter Constraints from a Lower Bound on Neutron-matter Energy. *Astrophys. J.*, 848(2):105, 2017.
- [133] Hajime Sotani, Nobuya Nishimura, and Tomoya Naito. New constraints on the neutron-star mass and radius relation from terrestrial nuclear experiments. *PTEP*, 2022(4):041D01, 2022. .
- [134] M. G. Alford, L. Brodie, A. Haber, and I. Tews. Relativistic mean-field theories for neutron-star physics based on chiral effective field theory. *Phys. Rev. C*, 106: 055804, Nov 2022. .
- [135] D. J. Millener, C. B. Dover, and A. Gal. Λ -nucleus single-particle potentials. *Phys. Rev. C*, 38:2700–2708, Dec 1988.
- [136] A. Gal, E. V. Hungerford, and D. J. Millener. Strangeness in nuclear physics. *Rev. Mod. Phys.*, 88(3):035004, 2016.
- [137] Jürgen Schaffner-Bielich and Avraham Gal. Properties of strange hadronic matter in bulk and in finite systems. *Phys. Rev. C*, 62:034311, Aug 2000.
- [138] Vivek Baruah Thapa, Monika Sinha, Jia Jie Li, and Armen Sedrakian. Equation of State of Strongly Magnetized Matter with Hyperons and Δ -Resonances. *Particles*, 3(4):660–675, 2020.
- [139] J. Haidenbauer and U. G. Meißner. In-medium properties of a ΞN interaction derived from chiral effective field theory. *Eur. Phys. J. A*, 55(2):23, 2019.

[140] J. Haidenbauer, U. G. Meißner, and A. Nogga. Hyperon–nucleon interaction within chiral effective field theory revisited. *Eur. Phys. J. A*, 56(3):91, 2020.

- [141] Gordon Baym, Tetsuo Hatsuda, Toru Kojo, Philip D. Powell, Yifan Song, and Tatsuyuki Takatsuka. From hadrons to quarks in neutron stars: a review. *Rept. Prog. Phys.*, 81(5):056902, 2018.
- [142] Gordon Baym, Shun Furusawa, Tetsuo Hatsuda, Toru Kojo, and Hajime Togashi. New Neutron Star Equation of State with Quark-Hadron Crossover. Astrophys. J., 885:42, 2019.
- [143] Tetsuo Hatsuda, Motoi Tachibana, Naoki Yamamoto, and Gordon Baym. New critical point induced by the axial anomaly in dense QCD. *Phys. Rev. Lett.*, 97: 122001, 2006.
- [144] Andreas Schmitt, Stephan Stetina, and Motoi Tachibana. Ginzburg-Landau phase diagram for dense matter with axial anomaly, strange quark mass, and meson condensation. *Phys. Rev. D*, 83:045008, 2011.
- [145] Aleksey Cherman, Srimoyee Sen, and Laurence G. Yaffe. Anyonic particle-vortex statistics and the nature of dense quark matter. *Phys. Rev. D*, 100 (3):034015, 2019.
- [146] Yuki Fujimoto and Kenji Fukushima. Equation of state of cold and dense QCD matter in resummed perturbation theory. *Phys. Rev. D*, 105(1):014025, 2022.
- [147] Silvia Traversi, Prasanta Char, Giuseppe Pagliara, and Alessandro Drago. Speed of sound in dense matter and two families of compact stars. *Astron. Astrophys.*, 660:A62, 2022. .
- [148] Maurício Hippert, Eduardo S. Fraga, and Jorge Noronha. Insights on the peak in the speed of sound of ultradense matter. *Phys. Rev. D*, 104(3):034011, 2021.
- [149] Richard C. Tolman. Static solutions of einstein's field equations for spheres of fluid. *Phys. Rev.*, 55:364–373, Feb 1939. .
- [150] Richard C. Tolman. *Relativity, Thermodynamics and Cosmology*. Oxford University Press, 1934.

[151] J. R. Oppenheimer and G. M. Volkoff. On massive neutron cores. *Phys. Rev.*, 55: 374–381, Feb 1939. .

- [152] Sanjin Benic, David Blaschke, David E. Alvarez-Castillo, Tobias Fischer, and Stefan Typel. A new quark-hadron hybrid equation of state for astrophysics I. High-mass twin compact stars. *Astron. Astrophys.*, 577:A40, 2015.
- [153] James M. Bardeen, Kip S. Thorne, and David W. Meltzer. A Catalogue of Methods for Studying the Normal Modes of Radial Pulsation of General-Relativistic Stellar Models. ApJ, 145:505, August 1966.
- [154] Edward Witten. Cosmic separation of phases. Phys. Rev., D30:272–285, Jul 1984.
- [155] A. R. Bodmer. Collapsed nuclei. Phys. Rev., D4:1601–1606, Sep 1971.
- [156] Nicolas Kovensky, Aaron Poole, and Andreas Schmitt. Building a realistic neutron star from holography. *Phys. Rev. D*, 105(3):034022, 2022.
- [157] Joas Zapata, Thiago Sales, Prashanth Jaikumar, and Rodrigo Negreiros. Thermal relaxation and cooling of quark stars with a strangelet crust. *Astron. Astrophys.*, 663:A19, 2022.
- [158] Ingo Tews, Joseph Carlson, Stefano Gandolfi, and Sanjay Reddy. Constraining the speed of sound inside neutron stars with chiral effective field theory interactions and observations. *Astrophys. J.*, 860(2):149, 2018.
- [159] Sinan Altiparmak, Christian Ecker, and Luciano Rezzolla. On the sound speed in neutron stars. *The astrophysical journal letters*, 939(2):L34, 2022.
- [160] Larry McLerran and Sanjay Reddy. Quarkyonic Matter and Neutron Stars. *Phys. Rev. Lett.*, 122(12):122701, 2019.
- [161] Krishna Rajagopal and Andreas Schmitt. Stressed pairing in conventional color superconductors is unavoidable. *Phys. Rev. D*, 73:045003, 2006.
- [162] Roberto Anglani, Roberto Casalbuoni, Marco Ciminale, Nicola Ippolito, Raoul Gatto, Massimo Mannarelli, and Marco Ruggieri. Crystalline color superconductors. *Rev. Mod. Phys.*, 86:509–561, 2014. .

[163] D. V. Deryagin, Dmitri Yu. Grigoriev, and V. A. Rubakov. Standing wave ground state in high density, zero temperature QCD at large N(c). *Int. J. Mod. Phys. A*, 7: 659–681, 1992. .

- [164] E. Shuster and D. T. Son. On finite density QCD at large N(c). *Nucl. Phys. B*, 573: 434–446, 2000.
- [165] Rodrigo Negreiros, V. A. Dexheimer, and S. Schramm. Modeling Hybrid Stars with an SU(3) non-linear sigma model. *Phys. Rev. C*, 82:035803, 2010.
- [166] Brian D. Serot and John Dirk Walecka. The Relativistic Nuclear Many Body Problem. Adv.Nucl.Phys., 16:1–327, 1986.
- [167] Andreas Schmitt. *Introduction to Superfluidity: Field-theoretical approach and applications*, volume 888. Heidelberg: Springer, 2015. .
- [168] Yusuke Takeda, Hiroaki Abuki, and Masayasu Harada. Novel dual chiral density wave in nuclear matter based on a parity doublet structure. *Phys. Rev. D*, 97(9):094032, 2018.
- [169] Hiroaki Abuki, Daisuke Ishibashi, and Katsuhiko Suzuki. Crystalline chiral condensates off the tricritical point in a generalized Ginzburg-Landau approach. *Phys. Rev. D*, 85:074002, 2012.
- [170] Stefano Carignano and Michael Buballa. Two-dimensional chiral crystals in the NJL model. *Phys. Rev. D*, 86:074018, 2012. .
- [171] Michael Buballa and Stefano Carignano. Inhomogeneous chiral condensates. *Prog. Part. Nucl. Phys.*, 81:39–96, 2015. .
- [172] Robert D. Pisarski, Alexei M. Tsvelik, and Semeon Valgushev. How transverse thermal fluctuations disorder a condensate of chiral spirals into a quantum spin liquid. *Phys. Rev. D*, 102(1):016015, 2020.
- [173] Len Brandes, Norbert Kaiser, and Wolfram Weise. Fluctuations and phases in baryonic matter. *Eur. Phys. J. A*, 57(7):243, 2021.
- [174] Constança Providência, Tuhin Malik, Milena Bastos Albino, and Márcio Ferreira. Neutron star equation of state: identifying hadronic matter characteristics. 7 2023.

[175] Daniel E. Sheehy and Leo Radzihovsky. BEC–BCS crossover, phase transitions and phase separation in polarized resonantly-paired superfluids. *Annals of Physics*, 322(8):1790–1924, aug 2007.

- [176] Jian Deng, Andreas Schmitt, and Qun Wang. Relativistic BCS-BEC crossover in a boson-fermion model. *Phys. Rev. D*, 76:034013, 2007.
- [177] Wojciech Broniowski and Marek Kutschera. Ambiguities in Effective Chiral Models With Cutoff. *Phys. Lett. B*, 242:133–138, 1990. .
- [178] Joseph Kapusta and Charles Gale. *Finite-temperature field theory: principles and applications*. Cambridge University Press, Cambridge, 2nd edition, 2023.
- [179] Aleksi Kurkela, Paul Romatschke, and Aleksi Vuorinen. Cold Quark Matter. *Phys.Rev.*, D81:105021, 2010. .
- [180] Eduardo S. Fraga, Letícia F. Palhares, and Tulio E. Restrepo. Hot perturbative QCD in a very strong magnetic background. *Phys. Rev. D*, 108(3):034026, 2023.
- [181] V. Skokov, B. Friman, E. Nakano, K. Redlich, and B. J. Schaefer. Vacuum fluctuations and the thermodynamics of chiral models. *Phys. Rev. D*, 82:034029, 2010.
- [182] Elias R. Most, L. Jens Papenfort, Veronica Dexheimer, Matthias Hanauske, Horst Stoecker, and Luciano Rezzolla. On the deconfinement phase transition in neutron-star mergers. *Eur. Phys. J. A*, 56(2):59, 2020.
- [183] Sebastian Blacker, Niels-Uwe F. Bastian, Andreas Bauswein, David B. Blaschke, Tobias Fischer, Micaela Oertel, Theodoros Soultanis, and Stefan Typel. Constraining the onset density of the hadron-quark phase transition with gravitational-wave observations. *Phys. Rev. D*, 102(12):123023, 2020.
- [184] Carleton E. DeTar and Teiji Kunihiro. Linear σ Model With Parity Doubling. *Phys.Rev.*, D39:2805, 1989. .
- [185] D. Zschiesche, L. Tolos, Jurgen Schaffner-Bielich, and Robert D. Pisarski. Cold, dense nuclear matter in a SU(2) parity doublet model. *Phys.Rev.*, C75:055202, 2007.

[186] Eduardo S. Fraga, Rodrigo da Mata, and Jürgen Schaffner-Bielich. Su(3) parity doubling in cold neutron star matter. *Phys. Rev. D*, 108:116003, Dec 2023. .

- [187] Mark Alford, Arus Harutyunyan, and Armen Sedrakian. Bulk viscosity from urca processes: npe μ matter in the neutrino-transparent regime. *Physical Review D*, 108(8):083019, 2023.
- [188] Larry McLerran and Robert D. Pisarski. Phases of cold, dense quarks at large N(c). *Nucl.Phys.*, A796:83–100, 2007.
- [189] Gaoqing Cao and Jinfeng Liao. A field theoretical model for quarkyonic matter. *JHEP*, 10:168, 2020. .
- [190] J. Margueron, H. Hansen, P. Proust, and G. Chanfray. Quarkyonic stars with isospin-flavor asymmetry. *Phys. Rev. C*, 104(5):055803, 2021.
- [191] Denis Parganlija, Francesco Giacosa, and Dirk H. Rischke. Vacuum Properties of Mesons in a Linear Sigma Model with Vector Mesons and Global Chiral Invariance. *Phys. Rev.*, D82:054024, 2010.
- [192] Denis Parganlija, Peter Kovacs, Gyorgy Wolf, Francesco Giacosa, and Dirk H. Rischke. Meson vacuum phenomenology in a three-flavor linear sigma model with (axial-)vector mesons. *Phys. Rev. D*, 87(1):014011, 2013.